UNIVERSITY OF SOUTHAMPTON
UNIVERSITY OF PADOVA

Optics for Short Pulse X-Ray Sources

Magdalena Miszczak
supervised by
Dr. William S. Brocklesby
Prof. Piergiorgio Nicolossi
and Prof. Jeremy Frey

A thesis submitted in partial fulfillment for the
degree of Doctor of Philosophy

in the
Faculty of Physical and Applied Sciences
Optoelectronics Research Center

May 2019

Sede Amministrativa: Università degli Studi di Padova

Dipartimento di Ingegneria dell'Informazione

Faculty of Mathematics, Computer Science and Natural Sciences

SCUOLA DI DOTTORATO DI RICERCA IN: Ingegneria dell'Informazione

INDIRIZZO: Scienza e tecnologia dell'Informazione

CICLO: XXVIII

TESI IN COTUTELA

Optics For Short Pulse X-Ray Sources

Direttore della Scuola: Ch.mo Prof. Matteo Bertocco

Coordinatore d'indirizzo: Ch.mo Prof. Carlo Ferrari

Supervisore: Dr. Bill Brocklesby

Supervisore: Prof. Piergiorgio Nicolosi

Supervisore: Prof. Jeremy Frey

Dottorando: Magdalena Miszczak

Declaration of Authorship

I, Magdalena Miszczak, declare that this thesis titled, 'Optics For Short Pulse X-ray Sources' and the work presented in it are my own. I confirm that:

- This work was done wholly or mainly while in candidature for a research degree at this University.
- Where any part of this thesis has previously been submitted for a degree or any other qualification at this University or any other institution, this has been clearly stated.
- Where I have consulted the published work of others, this is always clearly attributed.
- Where I have quoted from the work of others, the source is always given. With the exception of such quotations, this thesis is entirely my own work.
- I have acknowledged all main sources of help.
- Where the thesis is based on work done by myself jointly with others, I have made clear exactly what was done by others and what I have contributed myself.

Signed: _____

Date: _____

UNIVERSITY OF SOUTHAMPTON
UNIVERSITY OF PADOVA

Abstract

Faculty of Physical and Applied Sciences
Optoelectronics Research Center

Doctor of Philosophy

OPTICS FOR SHORT PULSE X-RAY SOURCES

by Magdalena Miszczak

Extreme Ultraviolet (EUV) radiation defined between ∼30 eV and 284.2 eV [1] gives many opportunities for engineers and scientists. Shorter wavelengths, compared to visible light, allow a better optical resolution to be obtained. However, reflectivity and transparency of most materials in the EUV region is very low and therefore a lot of work needs to be done in order to improve optical systems. In that instance, optics for the EUV able to manipulate and focus the beam is needed. The field is still under rapid development as the water window spectral range is important for the bionanoimaging [2].

Part of the thesis focuses on developing optics for x-rays such as deformable mirror and beam splitter. Piezoelectric, deformable mirror (DM) has been designed to be studied in a vacuum system. We present published data from our experiments where deformable mirror changes shape of its surface, therefore wavefront after reflection from the DM is being manipulated. Some effort has been made on designing a beam splitter for more efficient separation of the high power laser from the EUV short pulses during the high harmonic generation (HHG) process. MoS_2 beam separator can allow for greater separation of the two wavelengths and significantly improve photon flux for imaging.

In this thesis we also present results from imaging biological samples (hippocampal neurons) by using lensless imaging technique - ptychography. High photon flux and stable, focused beam during the scan allowed to achieve satisfied experimental data with fine details resolved on the images. The 54 nm resolution obtained over 100 μm field of view provided phase and amplitude information, which helped in better understanding of neurons cells.

Acknowledgements

I would like to thank to Dr Bill Brocklesby, Prof Piergiorgio Nicolosi and Prof Jeremy Frey for their advices and support through the project. Special thanks to Dr Bill Brocklesby for his guidance, great motivation and patience.

I would like to thank to Michal Odstrcil, Peter Baksh and other colleagues from the group who helped with performing experiments.

Thanks to my family and friends who supported me during the project.

My PhD was supported by the Education, Audiovisual and Culture Executive Agency (*EACEA*) Erasmus Mundus Joint Doctorate Programme Project No. 2012 – 0033. The project was realized at the University of Southampton and University of Padova.

Contents

List of Figures

List of Tables

List of Abbreviations

ADC Analog to digital converterl

AO Adaptive optics

ASM Angular spectrum method

BS Beam splitter

CCD Charge-coupled device

CDI Coherent diffractive imaging

CVD Chemical vapor deposition

DIV Days in vitro

DM Deformable mirror

DPP Discharge-produced plasma

ePIE Extended ptychography iterative engine algorithm

EUV Extreme ultraviolet

FBS Fetal bovine serum

FEL Free electron laser

FIB Focused ion beam

FOV Field of view

HDR High dynamic range

HHG High harmonic generation

HSV Hue saturation value color transformation

IR Infrared (light)

LPP Laser-produced plasma

MEM micro-electro-mechanical

NA Numerical aperture

NGM Neuronal Growth Media

OPRP Orthogonal probe relaxation ptychography

PBS Phosphate-buffered saline

PDL Poly-D-Lysine

PFS Paraformaldehyde solution

PtV Peak-to-valley

PZT Piezoelectric

RMS Root mean square

ROC Radius of curvature

SEM Scanning electron microscope

TEM Transmission electron microscope

VIS Visible (light)

Chapter 1

Introduction

Microscopic techniques helped to extend our knowledge by possibility of studying the tiniest existed structures. First microscope invented by Robert Hook allowed to discover information about small biological organisms [20]. During the next decades due to the increased interest in imaging, focus was concentrated on improving imaging devices and access information not known yet. This leaded to increased magnification of imaging objects by using a lens microscope. In 1873 Ernst Abbe besides developing many optical instruments, he introduced resolution limit of a microscope represented by the formula below [21]

$$\text{Image resolution} = \frac{\lambda}{2\text{NA}} \tag{1.1}$$

Resolution in imaging depends on the illumination wavelength (λ) and numerical aperture (NA), while NA depends on the refractive index of the environment. This allowed for designing new microscopes and new imaging techniques such as commonly used nowadays scanning electron microscopy (SEM) and transmission electron microscopy (TEM).

As one of the factor of high resolution images is wavelength, soft x-rays are able to improve images providing higher contrast in comparison to the standard imaging methods (such as TEM). Higher penetration depth of x-rays allows for higher sensitivity of lighter specimens of a sample, therefore more data can be extracted. Apart from many advantages, there are also some drawbacks, where the most important is the need of vacuum environment due to the high EUV absorption by most of the materials.

The work presented in this thesis is focused on improvement of coherent imaging system generated by HHG laboratory source by introducing new optical elements. It also

presents very important application of the EUV – biological samples imaging. EUV imaging requires high flux and great stability of the source. The flux is strongly linked to the HHG process which requires EUV isolation from high power radiation. It is executed by using beam splitters/filters which separate both wavelengths. Improving mentioned devices can increase separation efficiency, therefore higher flux achieved allows for better penetration of the EUV through the sample, therefore more information resolved.

Another challenge while working with the EUV radiation are optics imperfections or other defects on the way of light (such as temperature changes) which cause wavefront deformations. Those defaults massively decrease quality of the image. Adaptive optics (AO) technology significantly reduces mentioned distortions, where the best examples are images achieved by astronomical telescopes with AO adaptations. During the project, AO technology has been successfully used for the first time to manipulate soft x-rays wavelength.

Chapter 2 of the thesis provides background of the x-rays sources, EUV interaction with matter, beam splitters devices and adaptive optics technology. Lensless imaging technique with details of biological imaging was introduced likewise. Chapter 3 demonstrates imaging in the Ultrafast X-ray Laboratory including laboratory source properties. Chapter 4 presents first application of an adaptive optics technique used in the EUV wavelength range. The last Chapter 5 concentrates on a novel MoS_2 beam splitter development in order to improve EUV/IR separation.

Chapter 2

Theoretical Background

The Extreme Ultraviolet (EUV) spectral region offers exploration of various fields of science. The most significant areas associated with the EUV are next-generation lithography technology [22],[23] and extreme ultraviolet imaging telescopes [24]. Extreme ultraviolet lithography is a meaningful next generation lithography which uses 13.5 nm wavelength of light [25] to manufacture integrated circuits. With the rapid technological improvement, greater performance of x-ray optics and precise beam control are needed.

This chapter starts with introducing basic physics behind the short wavelengths interaction with matter and methods to produce x-rays. Then, some more details about filtering high-power laser from weak x-rays signal during the HHG process have been provided in order to understand the working principle of a beam splitter. Unfortunately, with the best manufactured optics, there is still need of controlling wavefront of the light which can suffer from aberrations present in the optical system or some distortions caused by temperature changes on the path of the light. Adaptive optics (AO) allows for wavefront manipulation and improvement by applying deformable mirror which can minimize or reduce effects of aberrations. Theoretical background has been provided in order to give a better understanding of aberrations in the optical system and wavefront modulation.

A way to deal with challenges associated with wavefront aberrations caused by imperfect optics is lensless imaging. One of the scanning methods used in the project is ptychography, which allows to achieve high resolution images of biological samples. It uses mathematical algorithms in order to compensate and improve imperfections present in the optical system. Theory associated with this lensless imaging technique has been provided.

2.1 X-rays Sources

This section provides information about x-ray sources in a narrow part of the electromagnetic spectrum (0.01 to 10 nm). X-rays generally cannot be emitted from neutral atoms but from charged electrons, therefore ionization must take place first. Several processes have been explained here for better understanding of short pulse generation. These are: high harmonic generation (HHG), emission by synchrotron radiation sources, compact plasma-based EUV sources and free electron lasers.

2.1.1 High Harmonic Generation Process

As mentioned in the previous section, the short wavelength-nature of the x-rays plays an important role in science. The most powerful method, able to generate stable pulses of x-rays is High Harmonic Generation (HHG). HHG is a non-linear conversion process that produces light at harmonic frequencies with much shorter wavelengths than the driving laser field. HHG occurs when highly intense femtosecond laser pulse is focused onto a target, commonly a (noble) gas jet. If the electric field of the laser is of an order of magnitude comparable to the electric field of the atoms in the gas, electrons can be detached from the atoms by tunnel ionization. The electron is accelerated (in the field) and there is a possibility under certain conditions that it will combine with the ion. Interaction between electron and an ion can cause formation of high harmonics (emission of high energy photons, up to 1.3 keV with helium). Figure 2.1 shows the three step scenario of HHG.

In the first step of the HHG process (Figure 2.1 (1)) the Coulomb potential of the atom is modified by the intense electric field of the laser, which allows the electron to tunnel through the potential barrier and ionize. In the second step (2), the electron is accelerated in the laser field and gains momentum. The field reverses and the electron is accelerated back to the ionic parent (3). During the recombination, the electron emits kinetic and binding energy (form of electromagnetic radiation) which is x-ray light [1].

The three step model is a successful and straightforward way to understand basics of the HHG process, generally in gas-phase. Coherence properties of the harmonics depend on the fundamental laser field. They can be inherited from the coherence properties of the fundamental laser beam while ideal phase matching has place. However, presence of second or third harmonic (multiple harmonic orders with various intensity) causes incoherence despite the HHG signal is fully coherent.

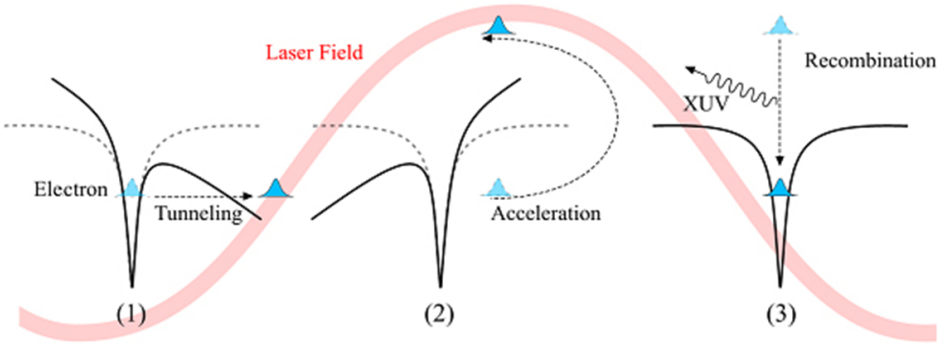

FIGURE 2.1: HHG presenting interactions between atoms and laser field - quasi classical three step model. (a) In the first step, an intense femtosecond electric field of the laser modifies the Coulomb potential of the atom and extracts electron. The electron is able to tunnel through the potential barrier and ionizes. (b) The electron is then accelerated in the laser field. (c) After the optical field reverses, the electron is driving back to the parent ion and it releases a photon with very high energy (taken from [3])

2.1.2 Synchrotron Radiation

Synchrotron radiation is a physical phenomenon which was discovered in 1947, when light was emitted by a charged particle beam moved in a magnetic field in a circular accelerator. Charged particles are accelerated to very high speeds. The observed radiation at the back of the vacuum chamber was a bright luminous path. The radiation has specific unique properties where the most important is its brightness (an attribute of a visual perception, where a source is radiating/reflecting light) - it is one of the brightest artificial source of x-ray radiation. It has also broad electromagnetic spectrum from microwaves up to hard x-rays, high stability and polarisation from linear to circular [26],[27].

2.1.3 Compact Plasma-Based EUV Source

A hot plasma can be a source of high power EUV radiation. Laser-produced plasma (LPP) and discharge-produced plasma (DPP) are two technologies which generate similar properties hot and dense plasma. Electron densities in plasma vary from 10^{17} to 10^{19}, electron temperature is about 20-50 eV. Focusing a high power laser onto such a dense medium is one way to produce EUV. The other method is based on producing plasma by a discharge (high-current) between electrodes of certain materials. By using

emission lines of different gases and different ionization levels, it is possible to tune the photon energy and use different wavelengths for the experiments. Commonly used gases are nitrogen and oxygen which both give strong resonant lines in the range of 15-24 nm. Those photon energies are close to the Co, Ni and Fe electrons binding energies and can be used to investigate magnetic materials. The advantage of plasma-based sources is high monochromacity of the emission lines of elements [28]. Compact plasma-based sources are mainly used as a radiation source for implementation of the next generation lithography (EUV lithography [29]).

2.1.4 Free Electron Lasers

Free-electron lasers (FELs) invented by John Madey [30],[31] are extremely bright sources which provide high power, tunability and coherence. The lasing medium in the free-electron laser consists of free, high speed electrons moving along a sinusoidal magnetic field. An undulator with a periodic arrangement of magnets generates sinusoidal magnetic field forces which move electrons in a sinusoidal trajectory. Spontaneous and stimulated emission occur which allow for optical amplification. The superposition of all fields generated by many electrons produces a wavelength of the size of an atom (x-rays). Free-electron lasers produce much higher coherence and spectral brightness in comparison with synchrotron radiation sources [32]. The main free electron laser project is the ultraviolet and soft x-ray free electron laser (FLASH) facility in Hamburg operating at a wavelength down to ∼6.5 nm. Other important once are SCSS Test Accelerator – Ultraviolet and soft x-ray FEL user facility at Spring 8 (∼30-60 nm) and LCLS (Linac Coherent Light Source) first hard X-ray FEL using 13.6 GeV electrons from SLAC Linac.

2.2 Extreme Ultraviolet Radiation Interaction with Matter

The electromagnetic radiation spectrum on the Figure 2.2 extends from infrared to x-ray light regions. It starts from the red (650 nm), then green (530 nm) and going to the blue (470 nm) wavelength. Shorter wavelengths start from ultraviolet (UV, 400-10 nm) radiation, extreme ultraviolet radiation (EUV/XUV, 125-10 nm) and x-rays (hard and soft x-rays, ranging from 10 to 0.01 nm). Short wavelength nature is very important as it allows for resolving and writing smaller features compared to visible light. Unfortunately, high absorption of most of the materials puts high constraints on the generation of the wavelength and experimental conditions. The main is that the full experiment has to be generally contained in a vacuum system, where x-ray interacts with matter. They can be reflected, transmitted and absorbed, which will be explained in the following section.

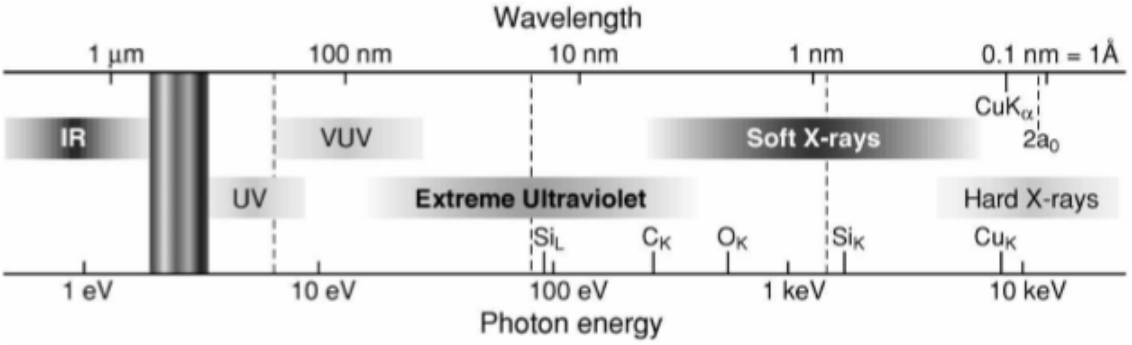

FIGURE 2.2: Spectrum of the electromagnetic radiation which extends from infrared to x-ray light. Short wavelengths can resolve small features of the imaging objects used in x-ray systems; picture taken from [1]

2.2.1 Photoemission Process

The process of photoemission is very important as it helps to identify elements and study chemical states. Emitted photoelectron during the photoemission process will travel through the material and it will lose its energy while interacting with other electrons. The x-ray travel distance gives importance to surface interactions. While radiation is passing through a thin material, the intensity lost can be observed while moving through the material.

$$\frac{I}{I_o} = e^{-\rho\mu x} \tag{2.1}$$

Equation 2.1 presents I/I_o dependence, where I is the intensity transmitted, I_o is the incident intensity, ρ is the density, μ is an absorption mass coefficient which depends on the energy and elemental dependence of a material, x is the thickness of a material.[1]

2.2.2 Scattering, Refraction and Diffraction Processes

Scattering is a physical process where forms of radiation while interacting with a material, change trajectory from straight to by one or more paths. There can be one scattering center (single scattering) or more scattering centers and radiation will scatter many times (multiple scattering). In inelastic scattering some part of an incident particle kinetic energy is lost, therefore it is not conserved (opposite to elastic scattering). Scattering occurs when on the way of incident light are particles (such as double slit). [33]

Refraction process occurs when wave propagation changes the direction of travel due to a change of a material where the light travels in. As the wave enters another medium, phase velocity will change, remaining the same frequency. The change is related to the refractive index of a material (n), which for the EUV/x-rays depends on the optical constants of a material and can be written as 2.2. Refraction basically occurs when on the way of light there is a solid element (but not only).

$$\tilde{n} = 1 - \delta + i\beta = 1 - \frac{r_o \lambda^2}{2\pi} N_{at}(f_1 - if_2) \tag{2.2}$$

where $1 - \delta$ represents the real part of the refractive index, β the imaginary part of the refractive index, f_1, if_2 are scattering coefficients, N_{at} is the number of atoms per volume, r_o is the classical electron radius and λ is the wavelength of light in a vacuum.

Diffraction occurs when a wave meets a slit or an obstacle (regular form, such as grid) on its way and causes interference of the light.

2.2.3 Multiple Interface Reflection and Transmission

In the EUV spectral region, most materials are highly absorptive and simple optics for short wavelengths are inefficient. There is a possibility to increase the reflectivity by a stack of layers, or multilayer structure conventional single layer coatings provide only a negligible reflectance. Figure 2.3 shows the principle, where part of the incoming light is reflected at each interface and part is transmitted and the reflected radiation will add

up in phase [1]. A large contrast in the optical properties is needed between alternating materials (at least two) – the first has high refractive index, whereas the second one low refractive index.

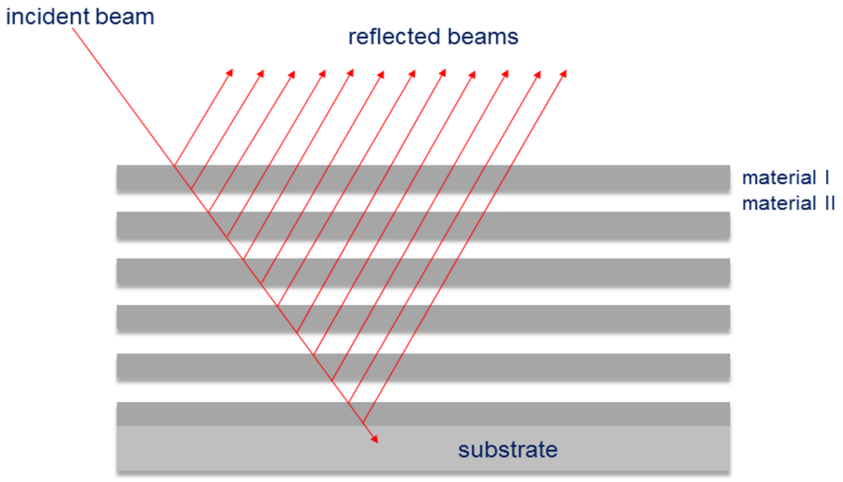

FIGURE 2.3: Principle of a multilayer mirror structure. The structure contains alternating materials - one with a low density and the other with a high density. The incident light illuminating the sample is being reflected by every layer of a multilayer structure. Together, the reflectivity will add in phase and the total reflection will be significantly higher than those provided from a single structure of a mirror. There is a possibility of creating another structures between layers due to interaction between them. As short wavelength requires, in order to achieve high optics efficiency, multilayer structures should have smooth interfaces deposited with an atom thickness precision. They can be fabricated by using many different methods, such as e-beam evaporator, magnetron sputtering, atomic layer deposition

The multilayer is characterized by the number of bilayers - two alternating layers (N), the thickness of one bilayer (Λ) and the ratio between the thickness of the bottom material (bottom of the bilayer) and bilayer (Γ). Figure 2.4 presents one of the fabricated Cr/Al multilayer mirror onto a Si wafer with a thickness of 60 nm. The surface roughness is extremely crucial for EUV applications, therefore all processes during the deposition are important starting from substrate preparation.

The highest reported reflectivity in the EUV spectral range is about 70% for a Mo/Si multilayer mirror near energy 95 eV. In order to obtain the highest optical performance, some methods have been presented to enhance the overall reflectivity of a composition. Aquila reported 10% increased reflectivity by adding a third scandium layer into the multilayer structure consisting of Mg and SiC for a wavelength of 37 nm [34]. The design of the ternary aperiodic multilayer mirror of Mo/B_4C/Si between 120 and 150 eV was presented and allowed for development of spectral filtering mirrors, useful for focusing of attosecond pulses [35]. Capping the top of a structure by another layer may be used to reduce oxidation of the mirror's surface. In order to achieve high total

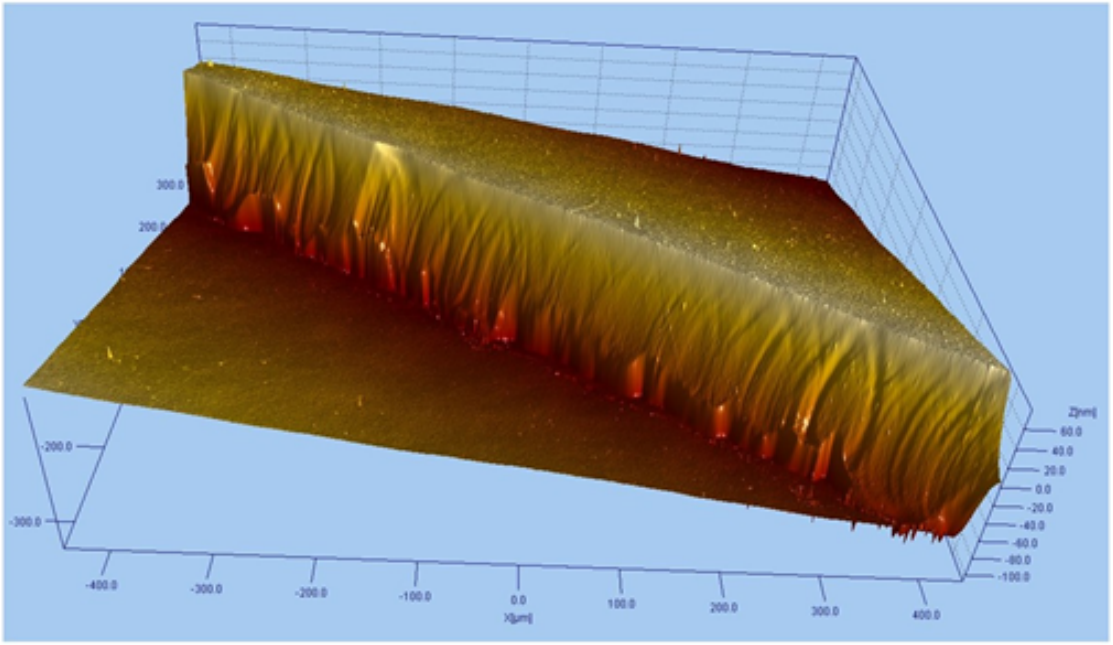

FIGURE 2.4: Surface topography of fabricated Cr/Al multilayer mirror. Mirror consisted of alternating layers of Cr and Al (was fabricated by e-beam evaporation technique, the total thickness was 60 nm. Parameters: Λ=10 nm, Γ=0.5, N=4. Λ is thickness of the bottom material in a bilayer structure, Γ represents ratio between the bottom material thickness in a bilayer to the total thickness of the bilayer

reflection of the multilayer, thicknesses of all layers have to be selected carefully. The relation between the wavelength λ and the angle of incidence θ (between a ray and the line perpendicular to the surface – called normal) is formulated by Bragg's law 2.3:

$$n\lambda = 2d\sin\theta \tag{2.3}$$

where n is an integer (determinated by the order given), d is the thickness of one layer.

According to Bragg's law, there is a need to prepare very thin layers (nm of thickness) for short wavelengths in the EUV region. Fabricating a high number of layers is challenging due to the roughness of a multilayer, intermixing [36] and stress of the overall structure. Materials should have thermal and time stability and ability to create perfectly sharp transitions [37]. The top material should also be oxidation resistant.

The total reflectivity can be calculated from Fresnel equations. Below, there is an approximated equation depending on the real ($\Delta\delta = \delta_1 - \delta_2$) and imaginary parts ($\Delta\beta = \beta_1 - \beta_2$) of the refractive index for two different materials:

$$R_{1,2} = \frac{\Delta\delta^2 + \Delta\delta\beta^2}{4\cos^4(\theta_o)} \tag{2.4}$$

where θ_o is an angle of incidence (degrees).

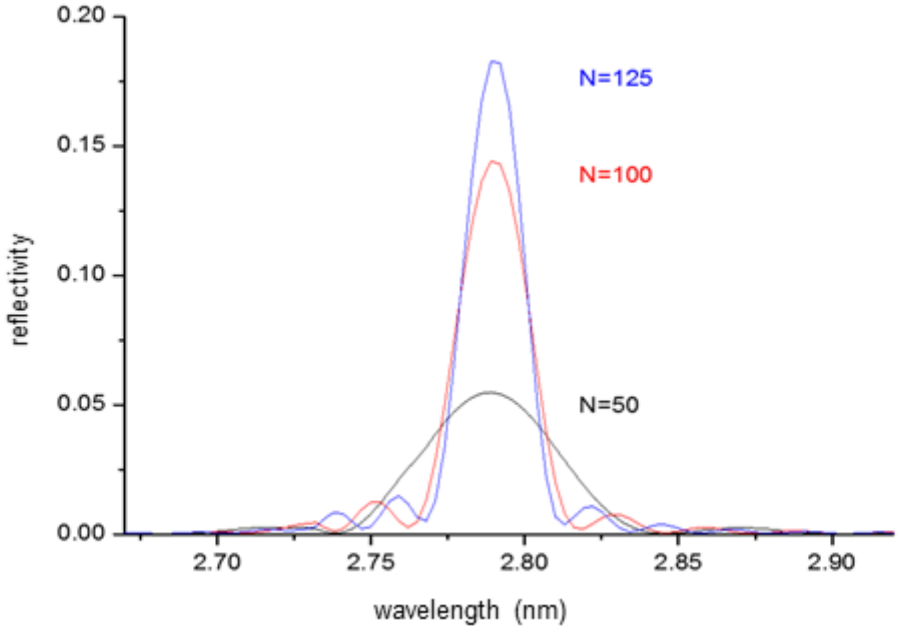

FIGURE 2.5: Reflectivity of the Ni/Ti multilayers depending on the number of bilayers. Parameters: Λ=1.4 nm, Γ=0.4, N=50, 100, 125; angle 90 deg

Figure 2.5 presents simulations for a Ni/Ti multilayer mirror with different number of bilayers deposited. As we can notice, reflectivity significantly increases while using higher number of layers.

In order to select materials for EUV optics, both optical and chemical properties have to be taken into consideration. The first material (spacer) should have a low atomic number (Z) and possibly the lowest absorption for the wavelength of interest. Materials with slightly greater value of δ than the absorption edge and therefore low absorption could be the best choice. The second material (absorber) should have a high atomic number and as a pair with the spacer should provide high reflectivity. By adding more bilayers, the reflectivity of the structure will increase.

2.3 Filtering Optics for Extreme Ultraviolet Radiation

During the HHG process, the produced EUV light is usually collinear with an extremely intense driving laser beam, therefore there is a need for spatial separation of the residual high-powered laser radiation from the weak EUV signal. Beam splitter, also called a semi-transparent mirror is an optical device which splits the incident beam into two - one reflected and one transmitted. The device is placed at the particular angle called Brewster's angle, to split efficiently path of the light. BSs are essential components not only in HHG systems but they are crucial parts of interferometers.

2.3.1 Beam Splitter as a Separator for the HHG Process

Beam splitters are optical components of a great interest in the soft x-ray region. The structure is manufactured by using proper materials that provide high reflectivity for the EUV wavelength and low reflectivity for the laser beam. The task is very challenging as most materials reflect both the fundamental laser beam and the EUV. It is furthermore important that BS is constructed from materials which are capable to withstand high power laser pulses. Figure 2.6 shows the principles of operation of a BS, where the incoming light is separated from harmonic and fundamental laser.

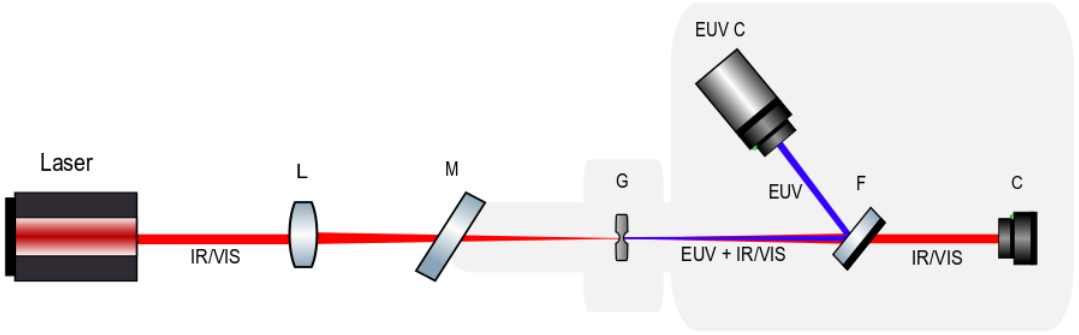

FIGURE 2.6: Configuration of a simple setup measuring beam splitter's efficiency. After EUV has been generated through HHG process, a beam splitter (F - filter) splits an incident light beam into two beams. BS placed at the particular angle reflects part of EUV light and transmits IR/VIS light. Ideal BS reflects full fraction of EUV and transmits full fraction of IR/VIS. Angle at which the BS is set is chosen in order to achieve the highest EUV reflectivity and the lowest IR/VIS reflectivity. In the image, L is lens, M - mirror, G - gas cell, F - beam splitter, C - camera

Efficient BS will have a high splitting ratio (function of wavelength and polarisation) and negligible optical losses so the total output of the power will be equal to the input power (dichroic BS). It is always important to consider the damage threshold of the BS, which is defined as a maximum/critical power of laser radiation causing changes in the structure of a material. Some BS operate at a specific angle while other with a range of wavelength.

The most common types of BSs are dielectric mirrors, cubes and fiber-optic BSs. **Dielectric mirrors** are devices which partially reflect the incidence light. The separation depends on the angle of incident. Reflectivity of dichroic BSs depends generally on the polarisation state of the incoming beam or the wavefront of the light. **BS cubes** with a specific cube form are constructed connecting two prisms together. The separation of the light has place at an interface in the cube, where the angle of interfaces is precisely chosen. Cube filters can be made of crystalline media (birefringent). **Fiber-optic BSs** are made of a quartz substrate (fibers) with, they are required mainly in a fiber-optic network (such as cable-TV).

There are only a few reported BSs able to separate the EUV from the laser light. BS with the most promising properties up to date is NbN [38], for which the measured reflectivity in the range of 13-18 nm exceeded 70%. The same research group developed Si and SiC beam splitters [39] with 56% reflectivity for Si and 45% for SiC at 29.6 nm. Others reported are: TiO_2/sapphire with theoretical reflectivity of 48% at 21.24 nm [40], MgF_2 with 44±10% at 93.3 nm [39] and the wedge-on-mirror output coupler BS, where the reflectivity is a subject to further investigation in the EUV spectral region [41]. Currently, the main challenge in the production process of BS is achieving high optical quality as smooth interface can provide high level of reflectivity in the soft x-ray region.

Brewster's angle

The reflectivity of materials for light polarised in the plane of incidence (p-polarised, parallel polarisation) goes to zero at Brewster's angle [1]. This unique effect is being widely used for separation of the EUV/IR/VIS. By placing our beam splitter at the particular angle for which theoretical reflectivity for the IR/VIS light will be the lowest, the received EUV signal should be free from fundamental laser. Therefore, the efficiency of our beam splitter in separating beam paths will be higher.

If we consider field components for parallel polarisation, where position of the electric field vector is perpendicular to the x, z plane of incidence, the scalar field amplitude at the interface will satisfy the equation 2.5.

$$E_0 + E_0^H = E_0' \tag{2.5}$$

After introducing magnetic field into equation, the boundary conditions will achieve 2.6.

$$H_0 \cos\phi - H_0^H \cos\phi = H_0' \cos\phi' \tag{2.6}$$

After eliminating magnetic field by $H = \sqrt{n\frac{\epsilon_0}{\mu_0}}E$, we get 2.7 and 2.8:

$$(E_0 - E_0^H)\cos\phi = nE_0' \cos\phi' \tag{2.7}$$

$$\frac{E_0^H}{E_0} = \frac{n\cos\phi - \cos\phi'}{n\cos\phi + \cos\phi'} \tag{2.8}$$

Then, applying Snell's law $\cos\phi' = \sqrt{1-\sin^2\phi'} = \sqrt{1-\frac{\sin^2\phi}{n^2}}$ and boundary condition $nE_0' = E_0 + E_0''$, we achieve the ratio of the field amplitude 2.9

$$\frac{E_0'}{E_0} = \frac{2n\cos\phi}{n^2\cos\phi + \sqrt{n^2 - \sin^2\phi}} \tag{2.9}$$

which lead us to achieve expression for reflectivity calculations for parallel polarisation 2.10

$$R_p = |\frac{E_0''}{E_0}|^2 = \frac{|n^2\cos\phi - \sqrt{n^2-\sin^2\phi}|^2}{|n^2\cos\phi - \sqrt{n^2-\sin^2\phi}|^2} \tag{2.10}$$

One of the example of calculated reflectivity for different polarisation states is Si wafer sample. Figure 2.7 presents the difference in polarisation states which leads to different reflectivity of Si wafer sample. Polarisation of light corresponds to the spatial orientation of the electric part of the electromagnetic wave. For light p-polarised we can distinguish discontinuity in reflectivity, where it goes to zero value (Brewster's angle at about 76 deg). That property of materials can be successfully used in filtering wavelengths of light.

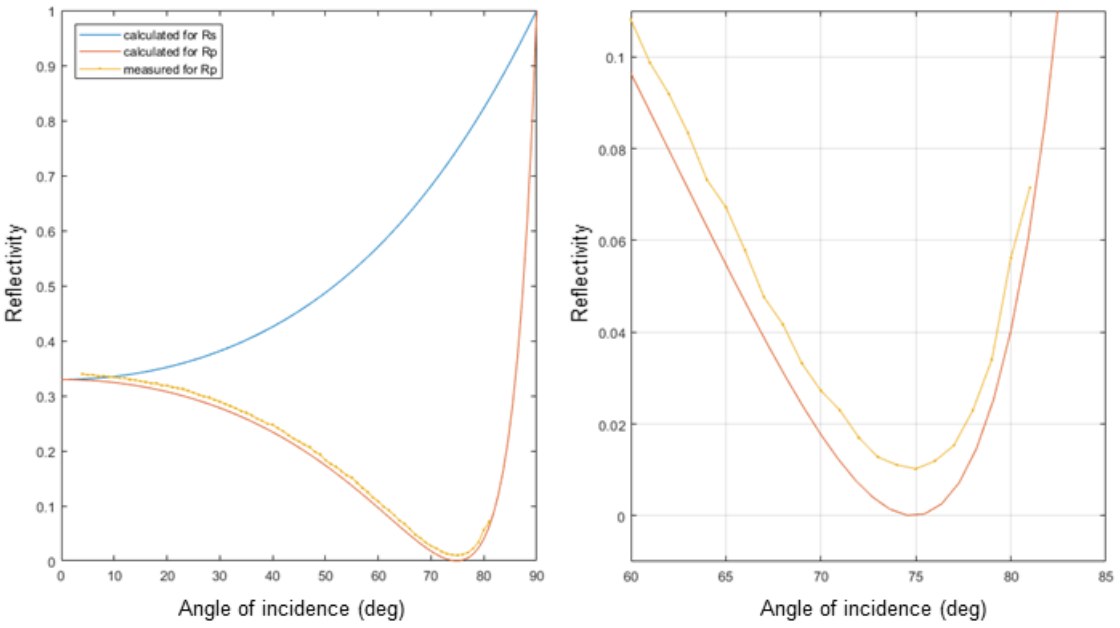

FIGURE 2.7: Reflection from Si wafer of light p- and s-polarised as a function of angle of incident; on the left there is measured (in the Ultrafast X-ray Laboratory in Southampton) and calculated reflectivity for Si; on the right there is magnification of the results. We can notice discontinuity at the Brewster's angle where the reflectivity is close to zero value. Both calculated and measured were performed for 790 nm wavelength of light

2.4 Adaptive Optics Technology

Femtosecond lasers due to their specific properties have been widely used in fields such as attosecond physics [42], femtosecond chemistry [43] and medicine [44]. To achieve very high intensity of the laser focused onto a small spot size, the beam has to be manipulated. While dealing with more compact laser systems, laser focusability can be significantly reduced if large number of optical components are being used. At the same time, imperfect optical EUV elements can cause wavefront distortions. Aberrated light coming from optics onto the camera increases image quality issues. Therefore, it is desirable to focus on the shape of the incoming wavefront and to improve the quality of the image.

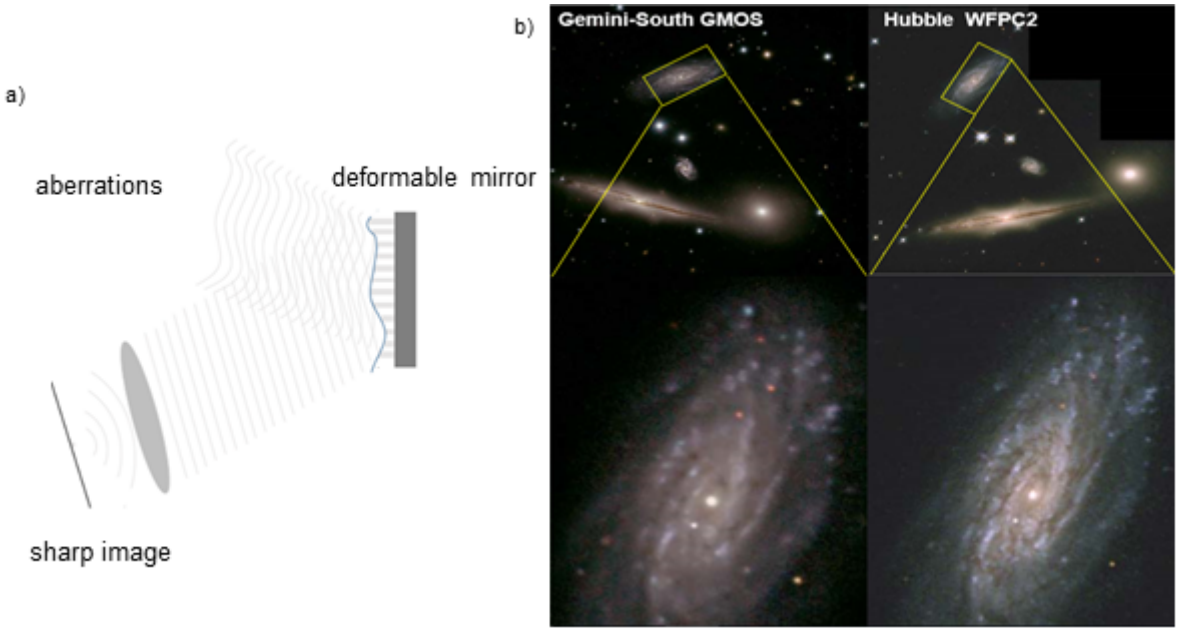

FIGURE 2.8: (a) presents scheme with principal of adaptive optics operation. Aberrated wavefront is corrected by deformable mirror; (b) is of the example showing image improvement by using different technology by NASA. Image of Hickson Compact Group 87 on the left was taken by Gemini-South telescope at Gemini Observatory, image on the right by Hubble. Although image on the left was taken with extraordinary good quality optical seeing, image on the right with AO shows spectacular improvement of the image. Installed the Advanced Camera for Surveys (AO technique) in 2002 on Hubble's telescope improved its significantly optical resolution [4]

Improvement of the optics manufacturing process reduces some aberrations in the system. While dealing with atmospheric distortions or any other distortions in the system such as local changes of the temperature, system improvement requires analyzing and modifying aberrated wavefront. Adaptive optics technology is a solution which improves performance of the system by reducing effect of the wavefront distortions. The most important component in the adaptive optics systems is the deformable mirror, which

deforms in order to fix distortions of the wavefront. The technology is used in many areas such as laser communication systems, microscopy or retinal imaging systems. It has been especially one of the most significant breakthroughs in astronomical telescopes, where adaptive optics helped with atmospheric distortion problem. Figure 2.8 presents one of the improved images by using AO technology.

2.4.1 Aberrations in the Optical Systems

In the following subchapter different types of aberrations which can appear in the optical system has been introduced and described. Aberration is defined as a deviation from the performance of the optical system which predicts paraxial optics. Paraxial optics uses Gaussian approximation and tracing ray of light at only small angles, which can be considered as a perfect system. Light source is located at infinity and it will give an image at a focal plane perpendicular to the optical axis. Any departure from paraxial optics theory will be understood as imperfections of the system - aberrations. Geometrical optics describes propagation of light and it uses rays which are useful abstraction to understand paths of the light and aberrations in the system.

Wavefront distortions are characterized by the peak-to-valley deformation of the wavefront from its intended shape. The main reasons for deviations are often inhomogeneity of the refractive index of a sample or atmospheric distortions. We can distinguish two types of optical aberrations (presented in the Figure 2.9) as: transverse aberrations, longitudinal aberrations and wave aberrations. A distorted wavefront will decrease the quality of our image and provide less information about the picture. Therefore, controlling wavefront aberrations is highly desirable.

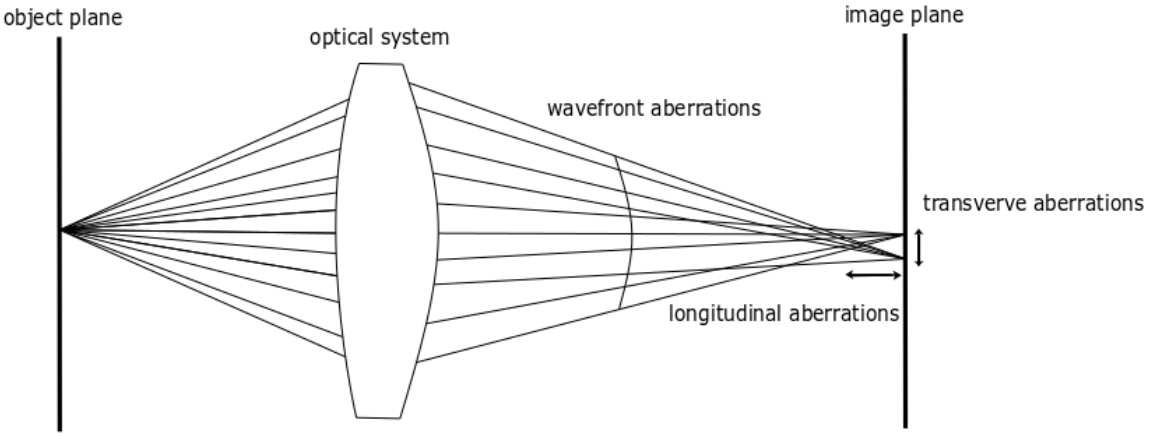

FIGURE 2.9: Aberrations in the real optical system design. Transverse and longitudinal aberrations represent a powerful method of describing the aberrational behavior of an optical system. Ray deviation from the point of focus can cause different forms of aberration. Additionally, system can suffer from wavefront aberrations

Aberrations can appear from imperfections and drawbacks of fabricated optics. Optical devices produced for shorter wavelengths require perfectly smooth, ideal surfaces. Some local changes of the temperature (caused by heat) on the path of the light can also introduce aberrations to the incoming wavefront. To identify and interpret deviations in a system an optical design program (such as ZEMAX) can be used where by building and analyzing a theoretical system, accuracy of the fabricated optics can significantly increase. In such an arrangement by tracing paraxial rays (perfect rays) we are able to evaluate the size and the position of an image and therefore to name specific aberrations and specify their dimensions. With that information it is possible to reduce or minimize the effect of aberrations and optimize distortions of our image. Sometimes by changing parameters like distances, positions of our optics we are able to reduce some distortions. In more complicated systems we are limited with corrections and usually we can reduce some aberrations, while the rest will remain or will increase. Another complex way to correct wavefront distortions are deformable mirrors in the adaptive optics system.

Chromatic aberration can appear in the optical system as axial (longitudinal) or transverse (lateral) form. Figure 2.10 presents the situation where different wavelengths of light are focused at a different position of the focal plane (different distances from the lens along the optical axis). The reason for the described phenomena is dispersion causing failure to focus all colors at the same convergence point [45].

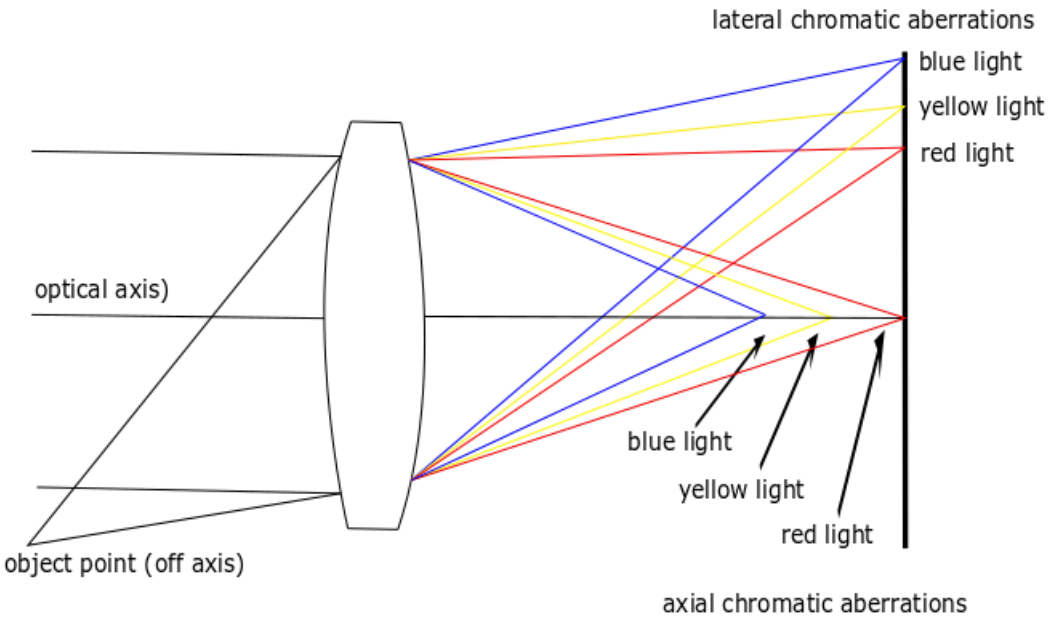

FIGURE 2.10: Chromatic aberrations caused by a single less, introducing different focal length for different wavelengths of light (longitudinal aberrations). The index of refraction and refraction of light vary for different wavelengths; therefore, different focus position has place. Using glasses with different dispersion is one of the way to avoid chromatic aberrations; rewritten from [5]

Lateral aberration cause an error in magnification as different wavelength focus at different distances from the center of the image.

Defocus has place when an image is out of focus, which means focus is shifted along the optical axis from the plane of its best focus position (Figure 2.11). Defocus reduces contrast, sharpness of the image, where some details become blurred. The degree of image blurring depends on the lens f-number, where low f-numbers are very sensitive to defocus, while high f-numbers have high tolerance of defocus.

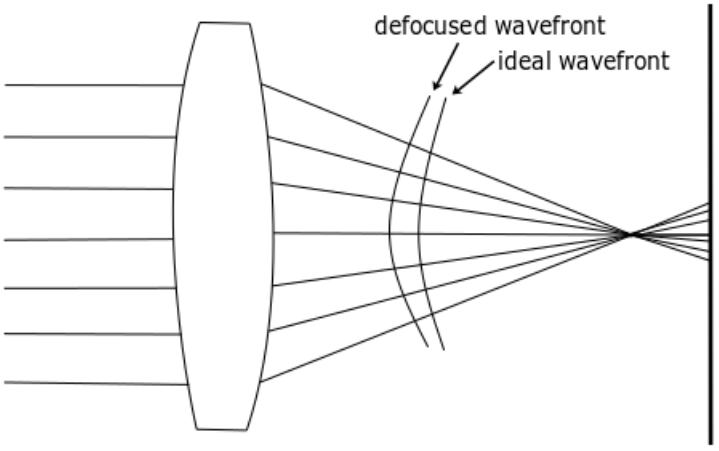

FIGURE 2.11: Defocus aberrations, where focus is shifted from the plane of the best focus position along the optical axis. The aberration is typical while using camera, microscope, telescope or binoculars. Defocus causes sharpness and contrast reduction, the image becomes blurred or even invisible; rewritten from [6]

Figure 2.12 presents **field curvature** optical aberrations (Petzval field curvature) where a flat object appears sharp in some certain parts of the frame rather than uniform across the frame. The described aberration has place due to the curved nature of optical elements causing not perfectly flat projection. Therefore, the entire image cannot be captured in a perfect focus.

Nowadays, produced lenses are designed and manufactured in order to minimize field curvature error, where a focal length increases with the angle of rays.

Coma aberration (Figure 2.13) can appear in the optical system as a result of the tilted or decentered incident wavefront (with respect to the optical surface) which can have origin in lens/other optical components imperfection. The aberration is causing distortion in the image formation process. The above aberration can be reduced by using combination of optical components or specifying the radii of curvature of both sides of a lens.

Astigmatism aberration is similar to the comatic aberration with the difference that astigmatism is less sensitive to the aperture size and they depend on the oblique angle

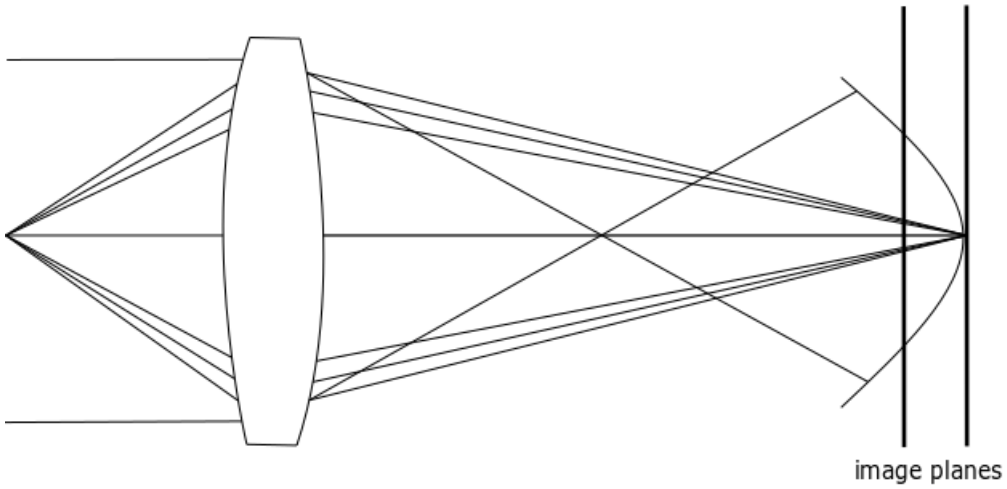

FIGURE 2.12: Petzval field curvature aberration. Rays of the light are perfectly focused at the center of the frame, while moving away from the center, sharpness is dropping which causes lower resolution in the corners of the frame; rewritten from [7]

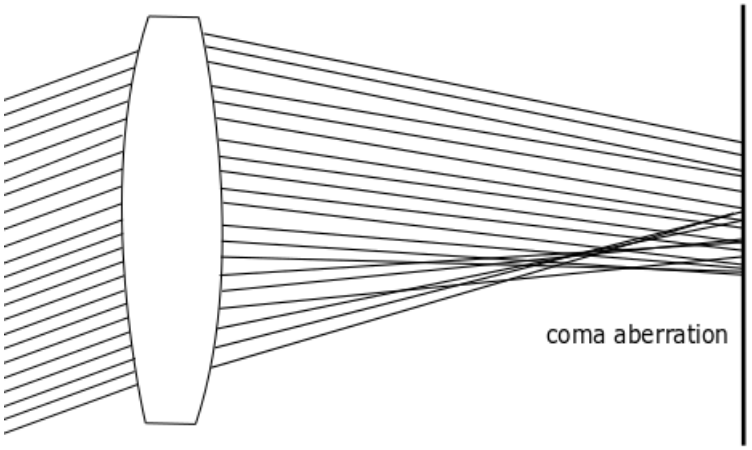

FIGURE 2.13: Coma aberrations presented in the system (tail like a comet). It appears in the system due to the tilted or decentered incident wavefront. The reason of coma presence is lens or other component imperfection. Coma aberration is typical for astronomical telescopes which uses parabolic mirrors; rewritten from [8]

of rays. Figure 2.14 presents astigmatism aberration in the optical system, where an off-axis image point of a specimen appears as an ellipse instead of a point. The aberration can cause unclear image into a diffuse circle.

Astigmatism combines features of focus and magnification error and is intimately associated with both field curvature and distortion.

As the aberration depends on the off-axis light beam angle, the image can be oriented tangentially (the vertical plane in optical system) or sagittally (plane which contains the principle ray in optical system).

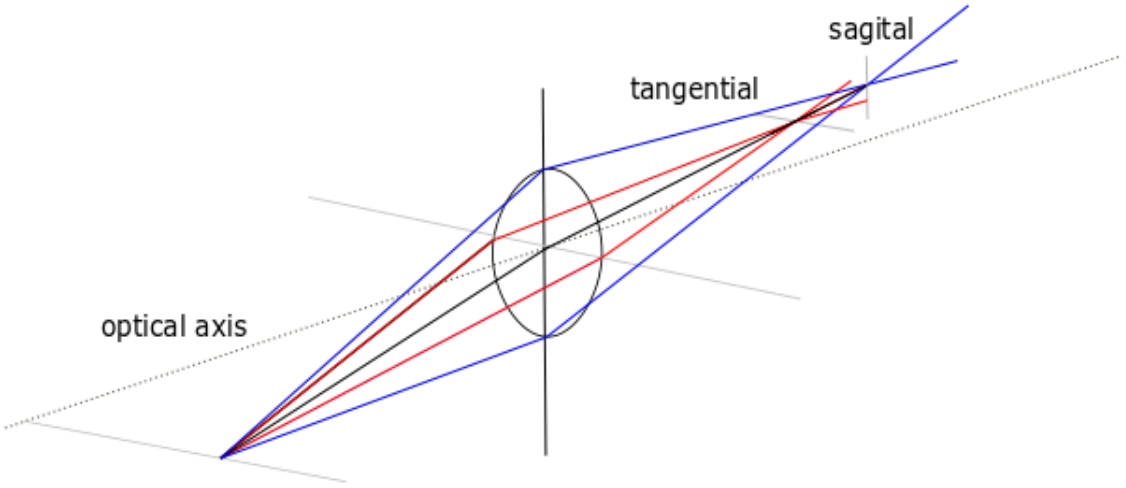

FIGURE 2.14: Astigmatism aberration in the optical system, where an off-axis image point of a specimen appears as an ellipse rather than a point. In other words, two orthogonal light axes are focused at different distances in space. Astigmatism is the most difficult aberration to correct, it combines magnification and focus errors and it is associated with distortion and field curvature aberrations; rewritten from [8]

The idea of **spherical aberrations** has been presented in Figure 2.15. It occurs when a beam of light is passing through a lens and it is refracted less close to the center of the optics while refraction increases close to the edges. As a result, incoming beam of light is focusing. Spherical aberration can appear from the poor quality lenses or incorrect lens design and will affect resolution of the image.

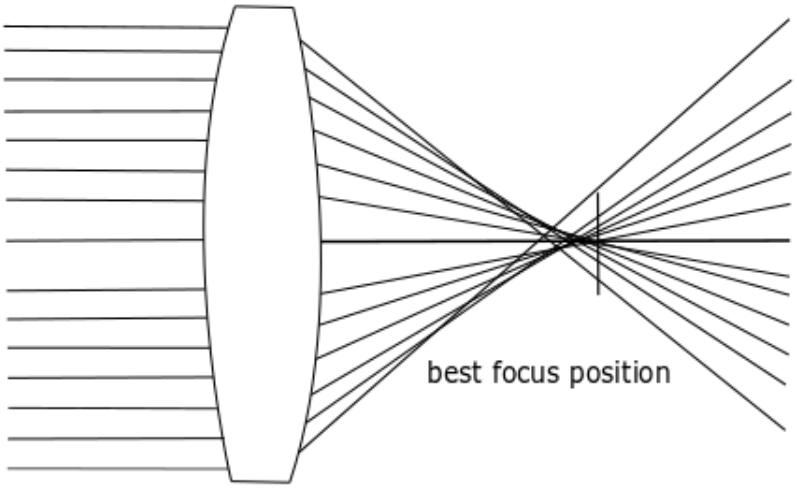

FIGURE 2.15: Spherical aberrations present in the system. Incoming rays closer to the center of the optical axis converge at longer distances along the optical axis, while those which are close to the bottom or top - converge at shorter distances. Position of the best axis is called "circle of least confusion"; rewritten from [9]

Distortion is a deviation which can be explained by introducing rectilinear projection. It is also called gnomic/gnomonic projection, where a portion of the surface of a sphere is mapping to a flat image. In other words, projection with straight lines of a scene will remain straight onto the image. There are few types of distortion which are presented in the Figure 2.16 and those are barrel, pincushion and moustache distortions. In barrel distortion we can clearly observe that magnification decreases when we move away from the optical axis. In the same situation, with the distance from the optical axis magnification of our image increases - we call the aberration pincushion distortion. In that case, as we can observe as presented in the Figure 2.16, the lines are bowed towards the center of the image (like a pincushion). A mixture of both above types of distortion cause mustache/moustache distortion. It starts at the center of the image as a barrel distortion and when we move away from the center it becomes pincushion distortion.

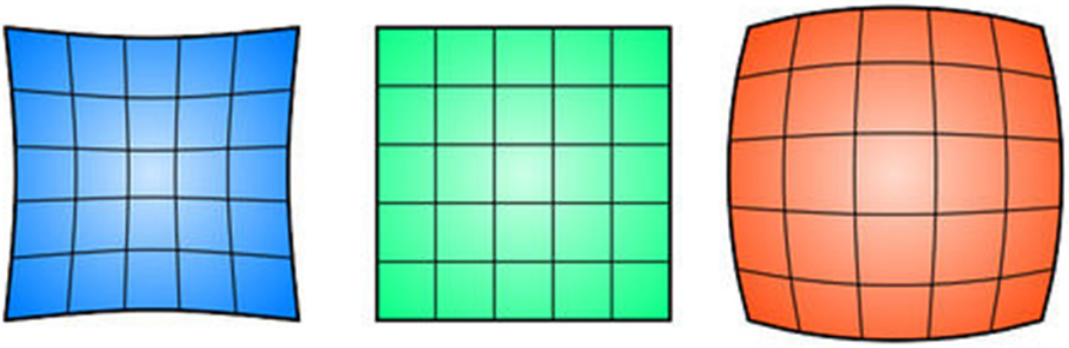

FIGURE 2.16: Three types of distortion can be identified in optical systems: barrel (magnification decreases as we move away from the optical axis, image on the left), pincushion (magnification increases as we move away from the optical axis; image on the right) and mustache/moustache distortion which is a mixture of both previously mentioned distortions (starts as a barrel distortion at the center of the image and as we move away from the center it becomes pincushion distortion). Image in the middle is without distortion aberrations [10]

2.4.2 Introduction to Wavefront Shaping

High reflectivity and long lifetime optics are needed in order to achieve acceptable efficiency of optical devices. It is possible to select materials, optimize structure and build optical components which provide high performance. Unfortunately, even with the most promising simulations, experimental reflectivity is often lower than expected. Reasons in the short wavelength region are aberrations of the system and wavefront distortions.

2.4.3 Wavefront Modulation

In the following subsection, necessary knowledge about wavefront description has been provided. Wavefront can be described as a set of points characterized by propagation of identical phase. It characterizes phase relationship between points across the pupil and aberrations associated with the system. Therefore, it is essential to make an accurate measurement and description of the wavefront. The most common method to perform wavefront sensing is the Shack-Hartmann wavefront sensor which will be described later. Other methods are: curvature sensor, lateral shear interferometer and pyramid wavefront sensor [46],[47].

2.4.3.1 Zernike Polynomials

One of the convenient way to express wavefront data and to help in understanding optical test results of optical systems is polynomial form. Zernike polynomials have been named after Frits Zernike who introduced orthogonal circle polynomials (sequence) in order to describe the imaging defects of aberrations in optical system [48]. Zernike polynomials describe wavefront data by a number of terms which determine the main forms of contributing deviations and the magnitude of deformation. Even (Z_n^m) and odd (Z_n^{-m}) Zernike polynomials are described mathematically by equation 2.11 (even Zernike polynomials) and 2.12 (odd Zernike polynomials). $Z_n^m(\rho, \varphi)$ are radial polynomials derived as Jacobi polynomials (classical orthogonal, hypergeometric polynomials) and tabulated.

$$Z_n^m(\rho, \varphi) = R_n^m(\rho)\cos(m\varphi) \tag{2.11}$$

$$Z_n^{-m}(\rho, \varphi) = R_n^m(\rho)\sin(m\varphi) \tag{2.12}$$

ρ and φ are polar coordinates; ρ is the radial coordinate (range from 0 to 1); φ is the azimuthal component (range from 0 to 2π); n and m represent individual polynomial coefficients (nonnegative integers).

$$R_n^{-m}(\rho) = \sum_{k=0}^{\frac{n-m}{2}} \frac{-1^k(n-k)}{k(\frac{n+m}{2}-k)(\frac{n-m}{2}-k)} \rho^{n-2k} \tag{2.13}$$

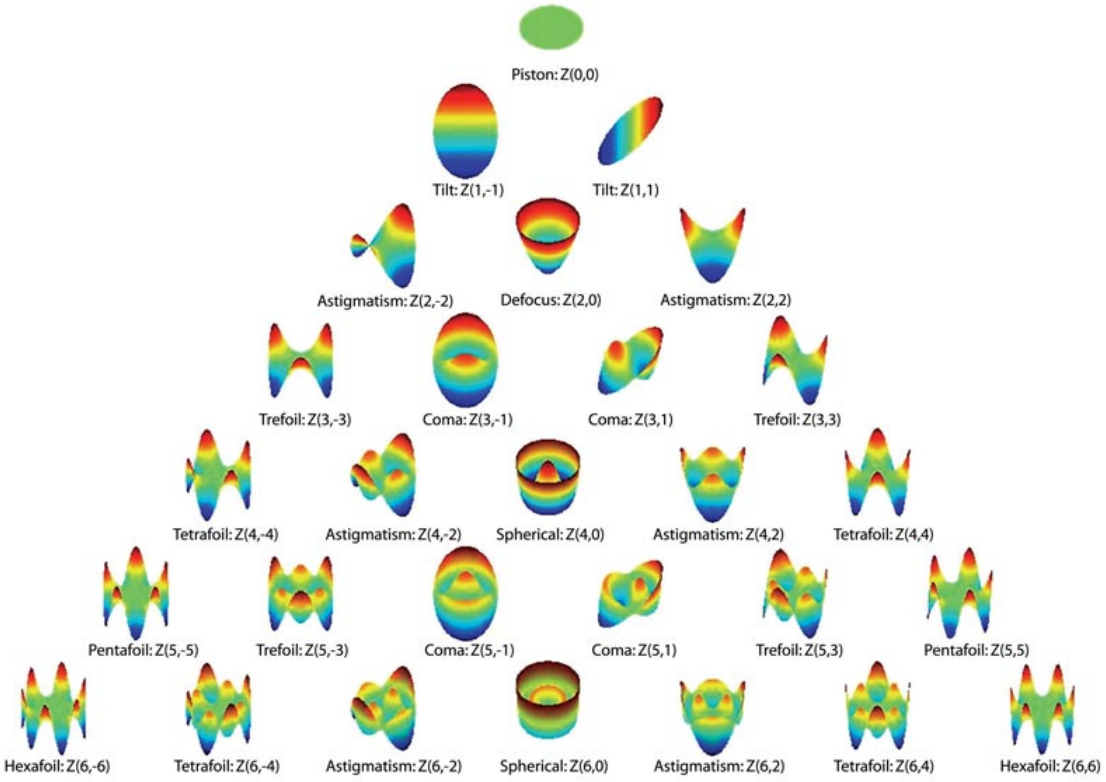

FIGURE 2.17: Zernike polynomials up to 6 orders (n=6, Piston is the 0 order) - radial degree (vertical) and azimuthal degree (horizontal). 3rd and more order aberrations are called high order aberrations. The pyramid has an infinite number of modes - here are presented first 28 as a representation of Zernike pyramid. As more modes are added, the shapes of aberrations are getting more complicated [11]

Figure 2.17 is the Zernike pyramid with representation of 6 orders of Zernike polynomials, where Piston at the top of the pyramid is the *0* order polynomial. Horizontal axis shows changing azimuthal degree and vertical axis presents radial degree. The pyramid has an infinite number of modes with a more complex shape with higher order is presented.

Nowadays, Zernike polynomials are widely used in optical design and image analysis. Nevertheless, they are not always the best representation of the wavefront data. Sometimes they cannot represent all details present in the optical system like air turbulence or fabrication errors. When air turbulence is present in the system, polynomials represent little value of it, therefore they can give poor representation of the wavefront.

2.4.4 Adaptive Optics System

The main components of the adaptive optics system are wavefront sensor which analyzes incoming, distorted wavefront, deformable mirror that corrects aberrations and computer controlling deformable mirror response. In more complicated systems more optical devices can be used in order to optimize the distortions.

2.4.4.1 Shack-Hartmann Sensor

There are several types of wavefront sensors which are needed to analyze the distorted wavefront. One of them, which has been used during the project is Shack-Hartmann wavefront sensor which the design is based on an aperture array developed by Johannes Franz Hartmann in 1900. Shack-Hartman sensor is an optical instrument which is widely used to characterize optical systems. It consists an array of lenses (lenslets) grouped side-by-side as presented in Figure 2.18.

All lenses have the same focal length which is focused onto a CCD camera (or other photon sensor). If the incoming wavefront is perfectly flat with no aberrations present in the optical system, each of the lenslet form an Airy-image at the centers of the detector (Figure 2.18(a)). In case of distorted wavefront, an Airy-image spots will be tilted and the image would be shifted due to phase aberration. (Figure 2.18(b)).

Figure 2.19 presents an example of Shack-Hartmann sensor used in optometry [13],[49],[50], where a virtual light source is created by the laser in the retina. According to the wavefront coming out of the eye, lenslets onto the Shack-Hartmann sensor create appropriate spots which helps to identify vision distortions. The local tilt on the sensor of every lens can be calculated from the position of the focal spot of the lens. By sampling all lenslets, all tilts can be measured and the wavefront can be described. According to the fact the sensor measures only the tilts, it is impossible to measure discontinuous steps of the wavefront.

2.4.4.2 Deformable Mirror Device

Deformable mirror (DM) is often used as part of an adaptive optics system, controlled by a computer. The surface of a mirror is deformed by the presence of actuators in order to control wavefront aberrations. The number of actuators represents the degrees of freedom which the mirror is able to correct. More actuators applied into the system give the possibility of higher accuracy corrections (Figure 2.20).

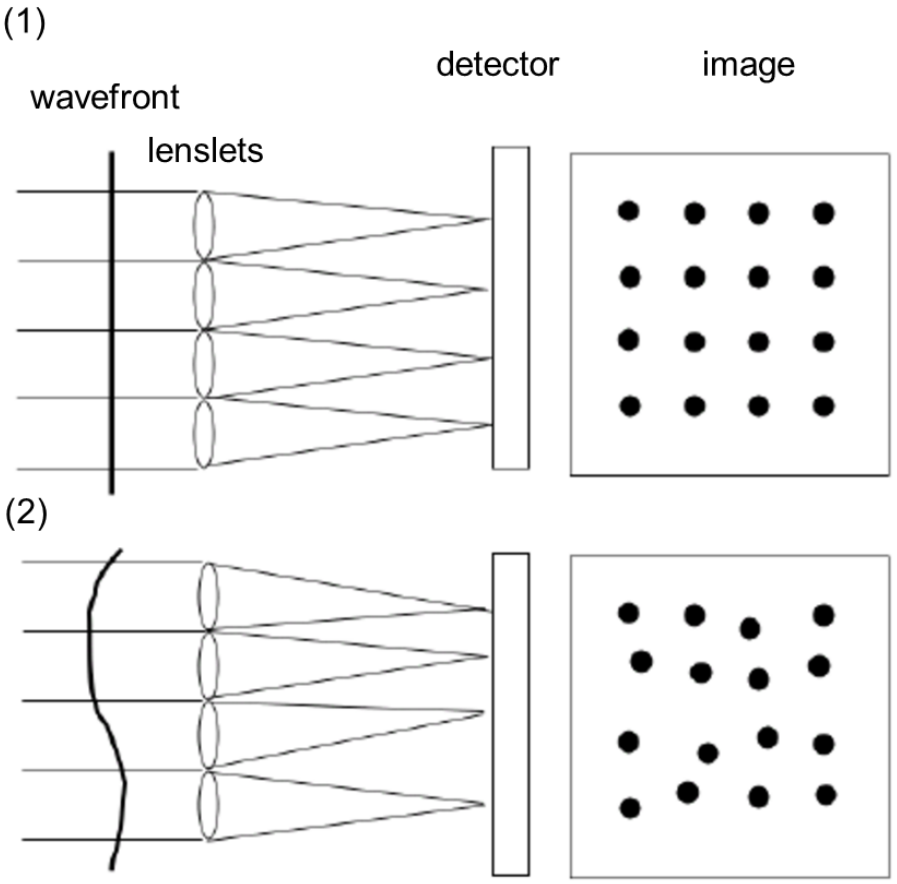

FIGURE 2.18: The Shack-Hartmann wavefront sensor in an optical system. The light is focused onto a CCD. (a) While dealing with a perfect wavefront, the Airy-image spots would stay at the center of their original position. (b) While dealing with distorted wavefront, Airy-image spots are shifted from the center position [12]

We can distinguish two types of deformable mirrors: bimorph and micromachined. Bimorph deformable mirror consists of two thin layers - one is a piezoelectric material, the other one is an optical surface. Between the two layers' conductive film as a common electrode is placed. When voltage is applied to the electrodes, it introduces variation in the area of piezoelectric material. Piezoelectric electrodes are placed usually in a square or a hexagonal arrays (Figure 2.20). With bimorph deformable mirrors with increasing spatial frequency, the maximum correctable amplitude diminishes strongly.

Micromachined deformable mirror -micro-electro-mechanical (MEM) are a new class of mirrors which can be made with a large number of actuators (hundreds). They are characterized by high bandwidths and low hysteresis. The actuation is formed between a thin electrode membrane and control electrodes. [51]

The most common used actuators are piezoelectrics (PZT) [52] which create stress under

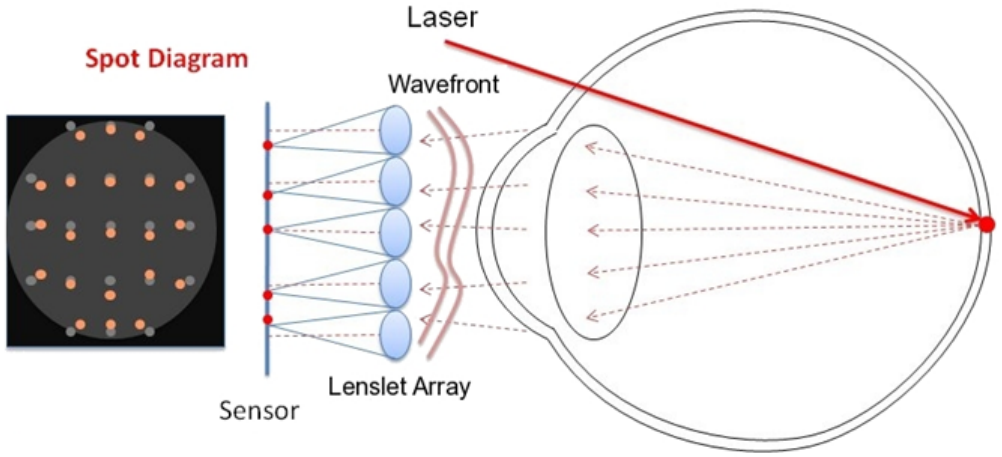

FIGURE 2.19: The Shack-Hartmann wavefront sensor in an optical system of optometry [13]. A virtual light source in the retina is created. The aberrated incoming wavefront coming out of the eye is analyzed by the Shack-Hartmann sensor. The array of lenslets creates appropriate spots and the wavefront can be described. The effect of the distorted wavefront can be then corrected [14]

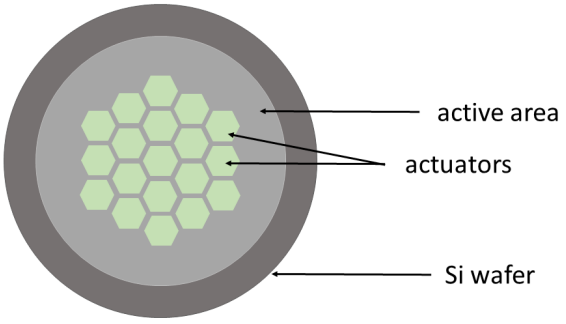

FIGURE 2.20: Piezoelectric surface of the mirror. Electric field applied to the surface of the actuators introduce displacement of the mirror's surface (Si wafer). On the image, piezoelectric actuators are placed in a hexagonal array

an applied electric field. Piezoelectric actuator converts an electrical signal into physical displacement (stroke) which can be precisely controlled. They are characterized by short reaction times and fast acceleration rates but also by the hysteresis caused by remanent polarisation [53]. Another type is magnetostrictive materials which produce a displacement in response to a magnetic field applied.

2.5 Lensless Imaging Technology

X-rays and EUV light can be profitably used for imaging the smallest structures of an object, with a few nanometer resolutions. Traditional imaging methods such as an optical microscopy rely on a lens which creates an image, and a specific detector device recording photons. High-resolution optical microscopy with high-numerical aperture and high magnification objective lenses reaches a resolution of approximately 250 nm. In contrast, lensless techniques such as coherent diffractive imaging (CDI) provide aberration-free images, with a resolution which is dose and diffraction limited. Resolution depends on an aperture size, exposure and wavelength of light. Main advantages of lensless imaging are no lenses in the optical system (aberration–free final image), large field of view and possibility of a 3D reconstruction of the image. These techniques meet lots of applications in diagnostics, bio sensing and cytometry by imaging nanoparticles, viruses and biomolecules. Computational techniques are necessary to reconstruct raw data taken by an image sensor. One of the forms of coherent diffractive imaging are powerful ptychography techniques. Ptychography allows to obtain meaningful images with approximately 10 nm resolution for biological samples. One of the drawbacks of ptychography technique is duration of the scan, typically 3-6 hours.

The following chapter discusses the theory of optical imaging and lensless imaging with focus on ptychography. Image creation in high-resolution microscopy is presented and compared with ptychography technique. Phase retrieval algorithms necessary for lensless imaging are also discussed.

2.5.1 Coherence

One of the fundamental requirement of the light source used for ptychography imaging is high coherence. Coherence describes correlation between phases in the monochromatic electromagnetic radiation which remain stable. When beams interfere, they produce a specific pattern of fringes which can be used as evaluation of the coherence of the source. Coherence can be mathematically represented with a mutual coherence function (Γ) which has been described by the equation 2.14

$$\Gamma_{12}(\tau) \equiv \langle E_1(t+\tau)E_2^*(t)\rangle \tag{2.14}$$

where E_1 and E_2 are electric fields at points *1* and *2*, t is the time and τ is the time delay [54].

There are two types of coherence properties which can be distinguish between interfering beams: longitudinal coherence and spatial coherence (Figure 2.21).

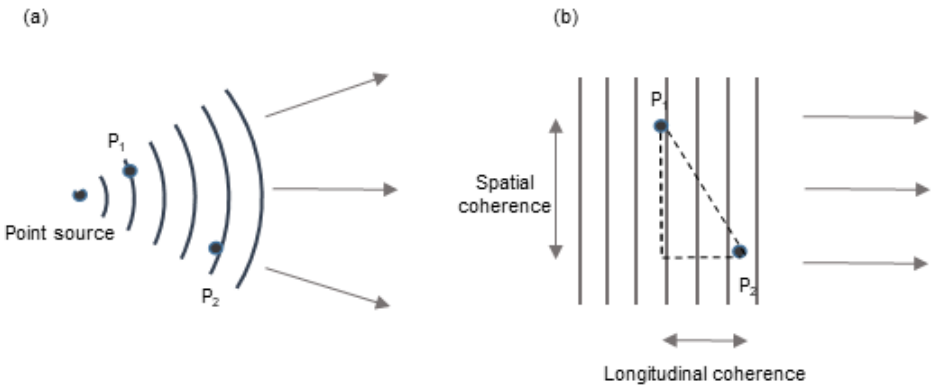

FIGURE 2.21: Scheme of longitudinal (temporal) coherence and transverse (spatial) coherence. Longitudinal coherence concerns the phase correlation between the wave's value and itself delayed (by a certain period of time). Spatial coherence describes the correlation between wave signals from one to another point. On the right a plane wave is characterized by an infinite coherence; rewritten from [1]

Longitudinal coherence is linked with spectral purity of the light source and it can be calculated from the equation 2.15. It presents monochromaticity of our source and shows how a wave at a different time interfere with itself. Coherence properties of a radiation field can be found by knowing spectral bandwidth and wavelength.

$$l_{coh} = \frac{\lambda^2}{2\Delta\lambda} \tag{2.15}$$

where $\Delta\lambda$ is the spectral bandwidth and λ is the wavelength of light [1].

Spatial coherence is linked to the size of the light source and emission angle of radiation. It is a correlation in phase between wave signals from one point to another point which are spatially distinct. Real radiation sources are partially coherent. The equation is:

$$l_{transverse} = \frac{z\lambda}{2\pi d} \tag{2.16}$$

where z is the distance from the light source, λ is the wavelength of light and d is the slit spacing [1]. In x-ray radiation temporal coherence is limited by short pulse duration.

2.5.2 The Problem of Phase Retrieval and Sampling

The intensity of the electromagnetic field can be described by equation 2.17 where E_0 and H_0 are complex scalar amplitudes. The intensity is the magnitude of its time-averaged Poynting vector.

$$I = \langle \mid S \mid \rangle = \frac{1}{2} E_0 H_0^* = \frac{n}{2}\sqrt{\frac{\epsilon_0}{\mu_0}} \mid E_0 \mid^2 \tag{2.17}$$

where n is refractive index of a medium, ϵ_0 is the vacuum permittivity, μ_0 is the vacuum permeability. According to the fact that detector is able to record the diffracted intensity (squared modulus of the amplitude) from the object, it cannot measure the complex amplitude. Therefore, information about the phase of a wave which is reaching the detector can be lost from the intensity measurement. Although it can be only detected directly through interference effects, in some circumstances phase can be retrieved by using different reconstruction algorithms.

A condition to retrieve a phase from the magnitude of the Fourier transform is to have a set of constraints on the image (commonly two: nonnegativity constraint and a support constraint obtained often from the prior knowledge/estimated). Phase can be recovered from the diffracted amplitude of its Fourier transform. Therefore, phase information can be calculated from the diffracted amplitude measurements via inverse Fourier transforms or Fresnel propagations.

The phase problem in ptychography is closely related to the sampling requirement. It was suggested by Bates [55] that the desired phase information from an object can be achieved by sufficient process of sampling the diffraction pattern. Sayre [56] proposed that the phase problem in crystallography can be solved when the diffraction pattern is sufficiently sampled at half of the unit cell. It is a criterion which was proposed and defined by Nyquist [57] that sampling the diffraction pattern at a rate of twice (of the Shannon frequency) will give an answer to the phase problem. While dealing with a crystal, the size of the unit cell will be considered as the Shannon frequency so the sampling would be half of the unit cell. Sayre realized that the phase problem can be solved for crystal by measuring at twice rate of a frequency where the Bragg peaks occur in a diffraction pattern. The theory has been extended for diffraction imaging (Bates) and the oversampling criteria has been defined as twice (the Nyquist) sampling rate in all linear directions, which means the diffraction pattern 2D has to be 4 times oversampled [58]. In 2000 Miao [59] proposed that sampling for a single position of CDI can be calculated from equation 2.18. Miao made a conclusion that sampled Fourier transform by the Nyquist frequency (where the signal is sampled at least twice the rate

of its highest frequency component [57]) has underdetermined magnitude. Both in one-dimensional objects and two- and three-dimensional objects it is underdetermined by a factor of two. To calculate unknown-valued pixel numbers, equation 2.19 has to be solved.

$$\sigma = \frac{D_{pixels}}{S_{pixels}} \tag{2.18}$$

where D_{pixels} is the total number of pixels while S_{pixels} represents the number of pixels inside the support (with unknown value). Object pixel is defined by equation 2.19.

$$P_{object} = \frac{\lambda}{2\sin\left(\arctan(\frac{P_{det}N}{2_z})\right)} \approx \frac{\lambda}{2\mathrm{NA}} \tag{2.19}$$

where P_{object} represents the size of an object pixel, P_{det} is the size of the pixel on the detector, N represents the number of pixels in the detector and z is the distance between the object and the CCD detector.

The expression of the complex-valued object density contains complex atomic scattering factor *f1* and *f2*, where *f1* is the effective number of electrons that diffract the photons in phase, *f2* is the attenuation. Assuming that both values in the complex-valued object density are positive, they can be used as constraints for phase retrieval [55].

2.5.3 Ptychographic Imaging

Phase information is very important in imaging systems, helping to visualize the specimen of interest. Ptychography is a coherent lensless imaging technique combined with scanning microscopy. It was invented in 1969 by Walter Hoppe [60] in the field of electron diffraction. He proposed to use finite coherent illumination to restore information about the phase from the recorded interference pattern between the Bragg peaks of a specimen. Then, the idea was proposed by Rodenburg and Faulkner to develop a reconstruction phase method for electron microscopy [61]. In 2009 the reconstruction algorithm was improved by Rodenburg and Maiden and it allows the reconstruction of the complex illuminating wave field and the complex object function [16],[62]. Figure 2.22 presents configuration of a ptychographic imaging experiment.

During ptychography of a sample, the object is illuminated with a highly coherent beam at different positions, such that illumination at each of the positions partially overlaps with each other. The far field diffraction pattern from each position of the scan is

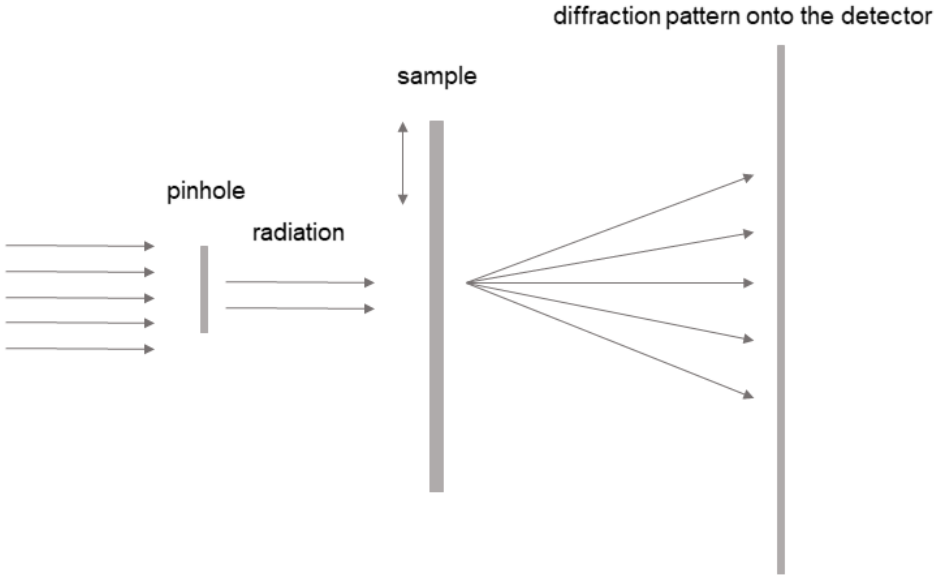

FIGURE 2.22: The configuration of ptychographic imaging. X-ray light is passing through the pinhole and being illuminated onto the object. Diffraction patterns from the scanning specimen has been recorded and processed in order to achieve the image [15]

recorded. The set of diffraction patterns collected from the scan is used to perform reconstruction by applying a phase retrieval algorithm.

2.5.3.1 Difference Map Algorithm

The difference map is the iterative reconstruction algorithm which has been introduced by Elser [63] and then extended and demonstrated by Thibault [62]. It is based on sets of constraints and projections onto the constraints. The algorithm can be applied to a variety of problems.

2.5.3.2 Extended Ptychographic Iterative Engine (ePIE)

Extended Ptychographic Iterative Engine (ePIE) is one of the phase retrieval algorithm that a series of diffraction patterns is recorded and written as a set of overlapping positions of an imaging sample. Below details of the ptychographic algorithms used in ePIE method are presented. Data was obtained from series of far-field diffraction patterns (J) of a sample interacting with probe wavefront. The diffraction pattern of a sample is taken from different regions of a sample such as at the end of the scan about 60-70% overlapping is achieved. Interaction between the sample and the probe can be

modelled by using complex multiplication. The wavefront which is at the exit of the sample (exit-wave) and its far field diffraction pattern can be modelled by a Fourier transform.

The flowchart in Figure 2.23 presents the operation of the extended PIE method.

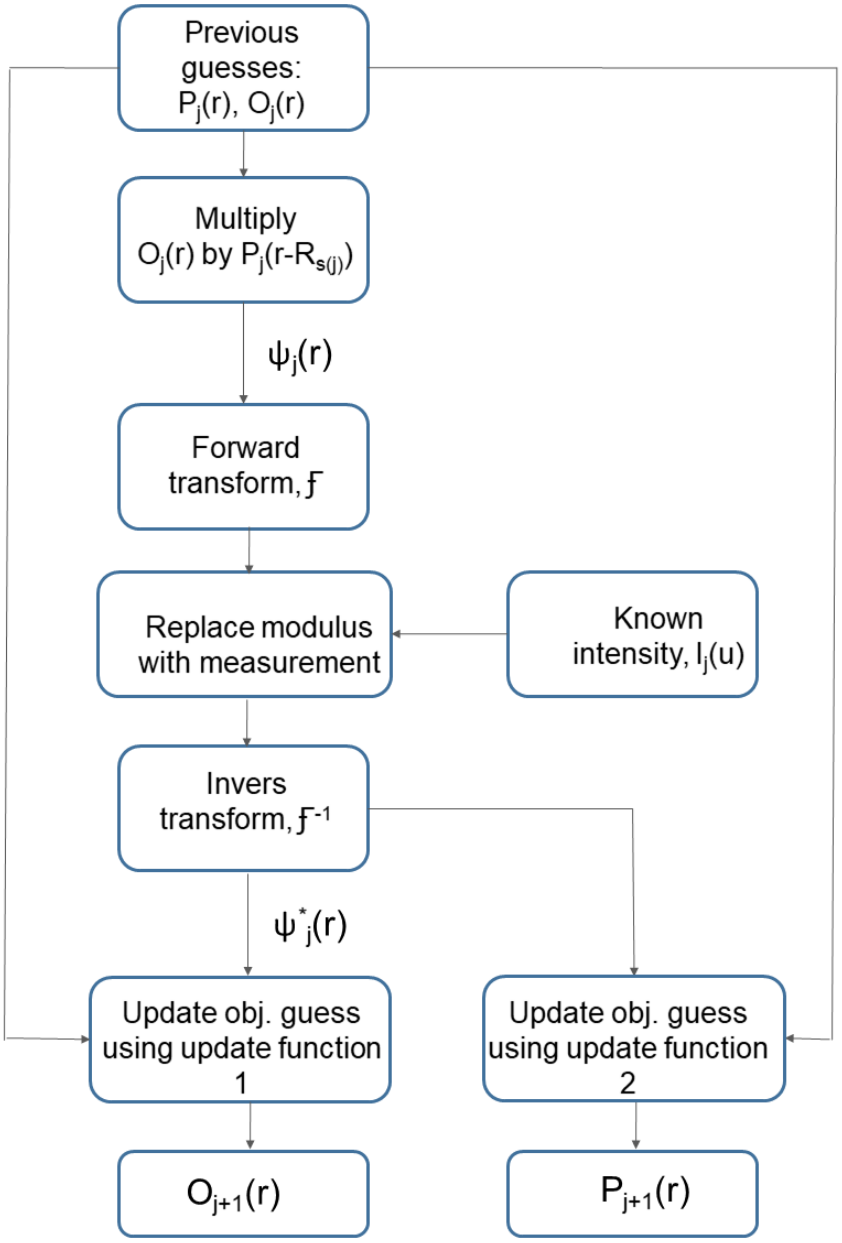

FIGURE 2.23: Flowchart for the ePIE method. $P_j(r)$ and $O_j(r)$ are respectively object and probe wavefront. The script is followed by multiplication by shifted probe, then replacement of Fourier transform is taking place and inverse Fourier transform. Re-written from [16]

The exit wave starts with multiplication of the current object by approximately shifted probe and is presented in 2.21.

$$\psi_j(r) = O_j(r)P_j(r - R_{s(j)}) \tag{2.20}$$

where r is the real-space coordinate vector. Vector R_j presents the relative shift between the object and the probe (before recording of the jth intensity diffraction pattern). After multiplication, the modulus of the Fourier transform (of the exit wave) is replaced with the square-root of the diffraction pattern and the new exit wave is calculated by using an inverse Fourier transform. $P_\mathrm{j}(r)$ and $O_\mathrm{j}(r)$ are respectively object and probe wavefront. The current object is given by 2.21.

$$O_{j+1}(r) = O_j(r) + \alpha \frac{P_j^*(r - R_{s(j)})}{(|P_j(r - R_{s(j)})|^2_{max}} (\psi_j^{'}(r) - \psi_j(r)) \tag{2.21}$$

Respectively, equation 2.22 represents the probe.

$$P_{j+1}(r) = P_j(r) + \alpha \frac{O_j^*(r - R_{s(j)})}{(|O_j(r - R_{s(j)})|^2_{max}} (\psi_j^{'}(r) - \psi_j(r)) \tag{2.22}$$

The above process of calculations continues with the all object diffraction patterns. Then single ePIE iteraction is completed. Main advantages of the ePIE technique is, that it is significantly robust to the detector's noise and it can work faster that other phase retrieval methods.

2.5.4 Biological Imaging

Two- and three-dimensional ptychography imaging allows for high contrast, label- and artefact-free images of the in vivo cells. Due to the penetration depth of x-rays, structural information of a sample on the nanometer scale can be provided. Main requirements for high contrast and resolution of an object is sufficient number of photons scattering the sample. The number should exceed the noise (Rose criterion [64]). A certain dose of the sample for imaging is also important and should be low enough to protect sample from the radiation. The main challenge for biological imaging is ionizing radiation which can damage the sample while ptychography illumination.

2.5.4.1 Contrast and Resolution

Resolution is defined as performance of the imaging system to resolve details of an object so we can distinguish small details on the image. It is the shortest distance between two specimens on the image which are distinguishable by a camera system. The process of

imaging requires a light source which illuminates an object in order to create an image. The light from the object will reflect, absorb and diffract and the scattered light will leave an object at a certain angle. At that point, numerical aperture (NA) of the imaging system plays crucial role as the resolution will depend on it. Numerical aperture specifies range of angles over which the imaging system is able to accept the light. It is defined as $NA = n \sin \theta$, where n is the refractive index of the medium where lens of the imaging system is located, θ is the half angle of the cone of the light which can enter/leave the lens. Resolution can be also defined by using Rayleigh criterion and it defines minimum resolvable detail (2.23):

$$x = 0.61 \frac{\lambda n}{\mathrm{NA}} \tag{2.23}$$

Resolution by using the Rayleigh criterion can be explained by using Airy patterns [65]. The Airy disk is a description of the best focused light spot that a perfect lens can make and it is often used in optics. The brightest spot of the highest intensity at the center of the pattern is the Airy disk, while concentric bright rings around including the spot is the Airy pattern. The Airy patterns representing the resolution of the image are presented in Figure 2.24. In (left) case, the Airy disks are separated, they do not overlap which makes objects clearly resolvable. While Airy disks are overlapping but they are still separated by more than the Airy radius disk (middle), two objects are just resolvable. Disks overlapping (right) with separation smaller than the Airy disk radius makes objects not resolvable. That is the reason for large lenses of the astronomical telescopes - they are manufactured to obtain the finest details.

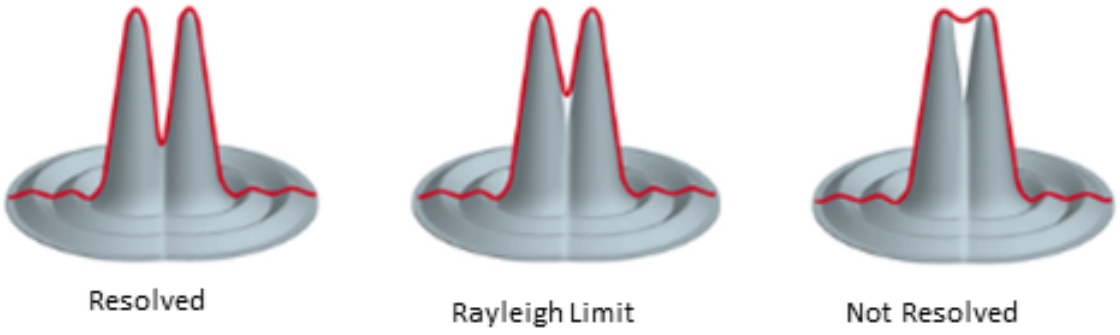

FIGURE 2.24: Explanation for the minimum resolvable details of an object by using Airy patterns a) Two points are separated as the distance between them is greater than Rayleigh criterion, therefore we can distinguish two points; b) the distance is equal to the Rayleigh criterion, the1points are 'just resolved'; c) two points are not resolved as the distance between them is smaller than Rayleigh criterion - the points are not distinguished [17]

The diffraction limit of light for a microscope has been presented by Ernst Abbe, who found out that for a specific wavelength of light which travels in the medium with a given refractive index n, light will make a spot with a radius defined by the equation 2.24.

$$d = \frac{\lambda}{2\mathrm{NA}} \tag{2.24}$$

NA in modern optics can reach value of 1.4-1.6, which means the Abbe limit of the resolution is about 250 nm.

2.5.4.2 Dose and Damage

Resolution of the image is highly related to the radiation dose onto the sample. The radiation can damage the sample, which will cause changes in the intensity of the diffraction spots of the collected data. The diffraction pattern will not correspond to the real image. As samples being imaged are based on huge variation of materials, therefore it is not possible to provide simple, theoretical treatment of a sample. It is quite obvious that high intensity of a light can make changes onto the sample.

Two types of radiation damage can be distinguished: primary and secondary damage. During ionization of a sample, some chemical and physical processes have place as photon interacts with a sample. Photoabsorption, Rayleigh and Compton scattering are main processes where chemical bond in a sample is breaking, what causes primary damage [66]. Secondary damage is connected with the diffusion of the atomic and molecular radicals which can cause further damage of a sample [67].

Nonelastic processes with a high energy photons absorbed can damage molecule. When a photon has higher energy than hydrogen bond, it may excite bonding electrons and break the bond. The free radical released during the process can break another nearby molecule. In Compton scattering, hard x-ray photon can hit molecules on its way and release electrons.

The radiation dose can be described as absorbed energy per mass 3.2.

$$\text{Radiation dose} = \frac{\text{absorbed energy}}{\text{mass}} \tag{2.25}$$

The dose unit is Gray (Gy; 1Gy = 1 joule/kilogram). For a specific material with a density ε, the radiation dose can be calculated from 2.26 [68]

$$D = \frac{N_0 \mu h\nu}{\varepsilon} \tag{2.26}$$

where N_0 is the incident number of transmitted x-rays per unit area (N), $h\nu$ is the energy of x-rays and μ is the coefficient (which depends on the material's density). Howells [69] has been studying radiation damage with X-ray diffraction microscopy for life-science imaging. Calculations of the dose needed to achieve an image of a sample with a given resolution has been based on the 'dose fractionation theorem' created by Hoppe and Hegerl [70]. To estimate the dose and the number of rays which are necessary to scatter the light from a specific unit area of a sample into the detector, equation 2.27 has been delivered. P is the number of photons scattered into the detector, the fraction of the incident light which will be scattered is defined by σ_s/d^2.

$$D = \frac{\mu h\nu P}{\varepsilon \sigma_s} = \frac{\mu P h\nu}{\varepsilon} \frac{1}{r_e^2 \lambda^2 |\rho|^2 d^4} \tag{2.27}$$

where r_e is the classical electron radius, d is a size of a voxel's sample (for which the coherent scattered intensity is calculated) and ρ is the scattering signal from a voxel. As $N_o = P/\sigma_s$, the number of x-rays which are needed to scatter the light is given by the equation 2.28.

$$N_o = \frac{P}{r_e^2 \lambda^2 |\rho|^2 d^4} \tag{2.28}$$

The requirement for an object to be sufficiently imaged is that the feature signal should be five times greater that the rms background noise. The wavelength should be shorter than about a quarter to a half of the resolution, which makes the diffraction angle small enough so the sample is a weak absorber and data can be processed on the Born approximation basis by ignoring multiple interactions (using single-scattering perturbation theory).

2.6 Conclusions

In this chapter, x-ray sources have been presented with the focus on the HHG process used in the project. HHG is a powerful method which uses IR focused in the gas jet to generate stable, coherent pulses of x-rays, which can be used for imaging purposes. Performing experiments in the EUV light require optical devices with specific properties. Optics needed for the short wavelength can be challenging to fabricate. In general, mirrors which are used for the light manipulation have multilayer structures of a very

thin layers of materials. HHG process also requires separation of the fundamental and the EUV laser beam which is performed by beam splitters.

In the EUV systems, aberrations play an important role. Mainly because it is challenging to fabricate optics with a nm precision as well as some local temperature changes can occur while performing the experiment. Wavefront modulation by using deformable mirror devices can improve the optical system and imaging process. DM is a multilayer mirror (for the short wavelength of light) with some number of actuators attached, which can cause displacement of mirror's surface.

A very successful method of imaging biological samples using short wavelengths of light is ptyhography. It requires high flux, high coherence and a high level of stability. During the process diffraction patters are measured in the far-flied and reconstructed to retrieve intensity and phase.

The aim of this chapter was to present some theoretical background needed to understand the further demonstrated experiments and considerations. It was needed to show how important role plays the EUV and the x-rays in science, medicine and other areas. Short wavelengths allow us to see the tiniest existed structures and subtract information. Therefore, improving areas which can increase efficiency of the imaging processes is essential.

Chapter 3

Ptychographic Imaging of Biological Samples

The work in the following section was performed in the Ultrafast X-ray Laboratory at the University of Southampton. This work demonstrates lensless imaging by using x-ray radiation at 29 nm spectral wavelength. High resolution images of biological samples were reconstructed from collected diffraction patterns and then extensively studied.

3.1 Mouse Hippocampal Neurons Ptychographic Imaging

Neurodegenerative diseases affect neurons in the human brain causing Parkinson's, Alzheimer's, and Huntington's disease. After neurons are damaged, human body is unable to reproduce them. As a consequence, it can result in degeneration/death of nerve cells. The number of people affected by neurodegenerative diseases increases every year [71]. In pursuance of using the most effective way of medical treatment, molecular mechanism controlling neurons damage progress process should be greatly understood. In order to achieve that, morphological analysis of neurons is needed. Therefore, improving imaging techniques and providing higher resolution images of biological samples is essential.

In the following section, high resolution images of mouse hippocampal neurons by using ptychographic x-rays imaging have been studied. Samples were illuminated by using monochromatic radiation at a wavelength of 29 nm. Collection of the scatter patterns was reconstructed to create images which provided details of the neurons structure which is critical for scientists. To contrast images, far field transmission ptychography technique has been used. Ptychography is a high contrast imaging method that solves

the diffraction-pattern phase problem. It is followed by the image reconstruction process which uses computational algorithms in order to retrieve the phase of the scatter pattern.

3.2 Neuron Structure

Neurons are brain cells which transmit electrical and chemical signals (information) in the brain. Apart from the transmission messages, they are responsible for many other functions, such as storing information (memories) and muscles control. Human brain contains $\sim$ 100 billion neurons. They are the core of the central nervous system. Information from one neuron to another one passes across synapse (a small gap), where electrical information is translated into chemical signals (neurotransmitters). After the signal is located on the other side of the gap, it becomes electrical in order to meet another synapse and translate the signal to pass it again. Therefore, neurons can send and receive information and one neuron can be connected with many other neurons, with different shapes. Figure 3.1 presents cellular structure of a neuron cell. A typical neuron cell contains axon, dendrites, nucleus and cell body (soma). Electrochemical impulses transmitted from one neuron are being received by dendrites of the other neuron. In order to form an axon, some components of neuronal cytoskeleton are required: mictotubules, neurofilament and actin filaments [72],[73]. Dendrites do not extent great distances from the cell body compare to the axon which can achieve even 1-meter length among large animals.

The information flow along the axis which passes it to other cells. The speed of sending signal by a nerve cell is ranging from 0.5 to 50 meters per second and it depends on the axon's structure [75]. We can distinguish different types of neurons with specialized functions responding to different signals such as sound, touch and other. **Nucleus** is a central part of a cell body and it is a source for most of the RNA produced in neurons so it contains majority of the genetic information of a cell. One neuron has usually one nucleus, however sometimes there is no nucleus or as in a human skeletal muscle cells can have more than one nucleus. **The cell body (soma)** is the main part of neuron which contains nucleus. Soma gives rise to multiple dendrites and/or always one axon. **Dendrites/dendrons** arise from soma, they create a complex structure "dendritic tree" and can be hundreds of micrometers long. **Axon** is a long projection (extension) from a neuron and it can travel 1 meter in a human body or even longer in other species. Usually axon has the same radius along the structure. Some neurons do not contain axons and information passes from dendrites. Axons as dendrites are being used by neuron for communication with other neurons [72].

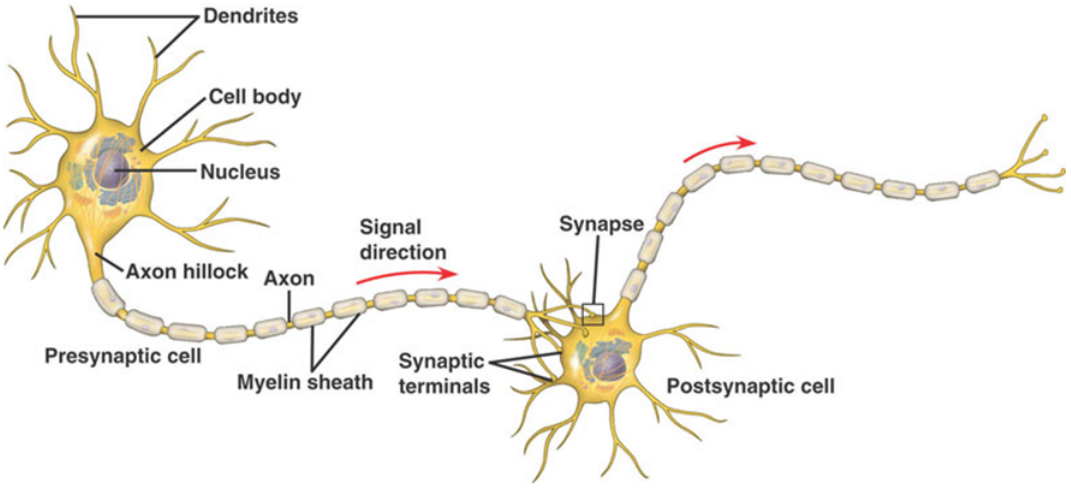

FIGURE 3.1: Cellular structure of a neuron cell which contains: nucleus, cell body (soma), dendrites and axon. Information is transmitted from one neuron to the other one by receiving signals by dendrites, then passing them through the axon which transmits information to another neuron in the body. In synapse electrical information are translated into chemical signals [74]

3.3 Experimental Information

In the following section x-ray imaging experimental setup has been presented. More information were concluded in subsection *Design of the Experimental Chamber* where details of the components of the vacuum experimental chamber have been given.

3.3.1 General Design

High intense ultrashort pulses have to be focused into an intense spot for the generation of high harmonics to take place. The outset part of the laser system consists of Nd:YLF pumped laser (Spectra Physics Millenia) and Ti:Sapphire oscillator (Spectra Physics Tsunami). The oscillator receives the feedback from an acousto-optical modulator (AOM) and initiates modelocking. The short pulses (30 fs centered at 800 nm) are selected and enter the amplifier where chirped pulse amplification process takes place. After the pulse comes into the amplifier, it is stretched in time by a grating system (by a factor of 10^4) and it enters Ti:Sapphire amplifier (Spectra Physics Spitfire Pro). Spectra Spitfire Pro is pumped by Q-switched frequency doubled laser (Positive Light Evolution, Nd:YLF). The final output are 40 fs pulses with 3 mJ energy and 1 kHz repetition rate.

In order to characterize the beam, a M^2 parameter (measuring beam quality factor) and a frequency resolved optical gating device (FROG, measuring spectral phase) have been used. The beam is then split into 3 beamlines, one of them is focused by 50 cm focal length lens to a $\omega o = 25$ μm spot inside the gas cell filled with 80 mbar of Argon (10^{-6} mbar vacuum chamber). Then infrared light is filtered by using Al filters (depending on the process, one or two filters) and enters the experimental vacuum chamber (at a pressure of 10^{-6} mbar).

3.3.2 Design of the Experimental Chamber

Figure 3.2 shows a schematic diagram of the imaging experimental chamber. The main components are multilayer EUV mirror, sample/camera stages and CCD camera. The EUV light entering the chamber is directed by the Si/Mo multilayer mirror (50 cm radius of curvature, ROC) onto the pinhole aperture, where it focuses and at a distance of about 2 cm from the aperture goes onto the CCD camera. At the focus position, a pinhole (usually 7 μm or 10 μm size) is placed and preferably about 50-100 μm further, a sample for imaging is arranged. Both samples (pinhole and imaging sample) and charge coupled device (CCD) located in the experimental chamber are operated by stages (x, y and z axis) with a precision of 1 nm (SmarAct stages) and 1 mm (Newport). The pinhole located in the experimental chamber serves as designating aperture for the coherence.

3.3.3 Sample Information

All investigated in the thesis samples were neurons cell structures extracted from mouse hippocampus one of the major components of the human's and many animals brain), at least 7 days in vitro (DIV). Preparation of all samples was performed by Joanne Bailey from the University of Southampton. All samples were cultured onto a Si_3N_4 membranes 500 μm $\times$ 500 μm window size and 50 nm thickness, which provided uniform and extremely thin support allowing for photon penetration. Before that, Si_3N_4 membranes were sterilized (UV light exposure for 15 minutes). The samples were incubated in Poly-D-Lysine (PDL) solution. Phosphate buffered saline (PBS) was used to wash unbound PDL and then removed. More details about solution/support during neurons samples preparations has been provided in Appendix C.

Hippocampal neuron cells were extracted from a female mouse's brain and treated with a solution of 0.05% of trypsin enzyme (7 minutes, 37 centigrade). 10% fetal bovine solution (FBS) was used to deactivate the trypsin enzyme. After the solution was removed, cortices (tissue's layer) and hippocampi were suspended by using Neuronal

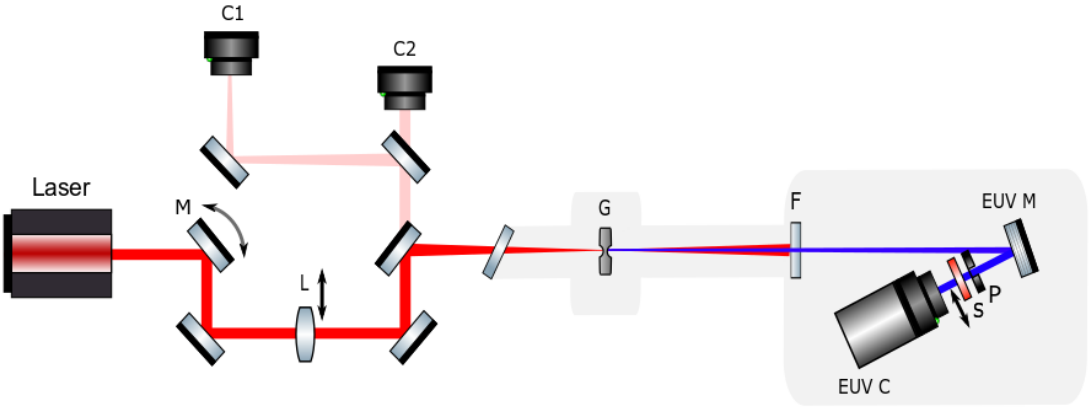

FIGURE 3.2: Experimental setup for the ptychography imaging. High-powered IR laser light is being manipulated by the set of mirrors and focused onto a gas jet in a vacuum system. Partially the same IR light is being slightly reflected by a mirror to the stabilization system which helps improving stability of the beam during the scan. After generation of the HH in the gas cell, the EUV and IR light is passing through the filter which separates IR from EUV. EUV beam in a vacuum experimental chamber is being reflected by the EUV mirror and it is passing through a pinhole, then a sample which is moving during the ptychography scan in order to collect the data. The beam is going onto the EUV camera where the actual collection of the data is taking place. Sample, pinhole and the camera are being manipulated by a set of stages. In the image, L is lens, g is glass, M - mirror, G - gas cell, C1/C2 - cameras, F - filter, EUV M - multilayer spherical mirror, S - sample, P - pinhole, EUV C - EUV camera

Growth Media (NGM) comprised of Neurobasal Glutamax, followed by 2% B27 (serum-free supplement). Cortices, hippocampi and NGM solution was dissociated by titration (process of neutralization, where a slow portion of a solution of known concentration is added to another solution with unknown concentration). The hippocampal neurons were added to each Si_3N_4 given approximately 7000 cells per membrane. Cortical cells have been used as feeder cells. This allowed to provide neurons support for the growth on the Si_3N_4.

After 7, 14 and 21 days (old samples, in vitro) some samples were incubated with ferrous chloride (50 μm, 30 minutes, 37 degrees centigrade) providing Fe^{2+} treatment. PBS was used to wash free Fe^{2+}. Formerly samples were fixed in 4% paraformaldehyde fixing solution (PFS) and 20% sucrose solution. After the PFA solution was removed, cells were dried by dehydration: fixed in 10 mins 70% ethanol, 10 min 80% ethanol, 10 min 100% ethanol and then left to dry on tissue. As DIV increases, some more cell somas can be identifying. At DIV 3 it is likely to identify some synapses neurites. DIV 7 presents young neurons and small spines. Mature spins are visible on DIV 20, where many synaptic connections should be already formed.

3.4 Ptychography Alignment and Image Acquisition

X-ray ptychographic imaging requires highly coherent and a high flux light with a high level of stability during the whole experiment. The configuration of the setup has been presented in Figure 3.2. Diffraction patterns were measured in the far-field, therefore the sample was placed in the circle of indistinctness (spot created by a cone of rays from non-perfect focus of a lens) and the camera about 2.5 cm from it. During all imaging experiments the Andor DX434 CCD camera has been used to detect EUV light. The performance of the x-ray laser system has been demonstrated in details in subchapter 3.3.2.

Andor CCD camera

Charge-coupled device (CCD) was invented in 1969 [76] and it allows data storage and image processing. CCD is an integrated circuit of capacitors which are based onto a silicon surface and form light sensitive elements. Array of capacitors (each capacitor represents a pixel) are made of metal oxide semiconductors. The silicon is doped with a small amount of another material (gallium, phosphorus) which gives specific properties. Pixels are distributed across a focal plane of a camera in a square array in the form of several millions pixels. When light strikes onto a pixel, photons penetrate the silicon layer (an image area of the CCD) and photoelectric effect is achieved. Intensity of light is converted into electrical charge as electrons are being displaced and collected/stored in the pixel. The number of photos striking the CCD image will lead to the number of electrons emission from the layer of silicon (approximately 8 μm thin). The greater number of photons will lead to the greater amount of electrons emission. Therefore, intensity of incident light is proportional to the charge difference and to the voltage. The capacitance of a single pixel depends on the charge and the voltage of the capacitor.

$$C = q/V \tag{3.1}$$

where C represents capacitance, q is the charge and V is the voltage.

Pixel being exposed for a specific amount of time, collects proportional amount of photons. The more photons strike the silicon, the more photons are produced, therefore depending on the exposure time, the amount of light is collected. A pixel has the capacity of storing electrons, which is called saturation capacity - the number of electrons which can be stored in a pixel. Above that value, additional electrons will not be stored. Saturation occurs as the charge that every pixel can store before being read-out (well depth) is limited or due to the ADC (analog to digital converter) which has limited dynamic range.

The electron is being displaced in a capacitor and after exposure is finished, the electrical charge is stored by a pixel. At that time, the charge is transferred pixel by pixel and all signals are shifted by capacitors once at a time. For every single pixel it is possible to find out how much charge has been captured. Then, voltage conversion into a digital value is taking place in order to capture digital images. This provides information about how many photons felt on every single pixel. The digital form of data with series of values is collected and the image can be formed.

The Andor camera used in the ptychographic imaging is an EUV-sensitive Andor DX434 camera, which allows for direct sensitivity detection from soft x-ray. It contains of 1024 $\times$ 1024 array with 13 μm pixels. We can define how many photons can be recorded before saturation takes place from equation 3.2.

$$\text{Photons Number} = \frac{\text{well depth} \times \text{E}_{\text{EH}}}{\text{E}_{\text{photon}}} \tag{3.2}$$

E_{EH} denotes the amount of energy needed to create a pair of electron-hole in the Si layer (doped) and it is 3.65 eV. E_{photon} represents photon energy. For our 1k-chip Andor DX-434 camera and 43 eV we use in the Ultrafast X-ray Laboratory saturation appears at 17000 photons. This relates to the dynamic range of the camera.

While talking about camera's performance, it is important to refer to the signal to noise ratio and dynamic range. Both measures the ratio of noise versus the signal, which are observed by the camera. The number of photos which are needed to collect signal equivalent to the noise observed by the sensor is called absolute sensitivity threshold. The number of photons for a given image of an exposure time t, quantum efficiency QE, pixel counts c and counts per photon cpp can be calculated from the equation 3.3

$$\text{Photon Flux} = \text{c}/(\text{t} \times \text{QE} \times \text{cpp}) \tag{3.3}$$

The QE is the number of signal electrons produced per photon.

CCD camera apart from the desired signal detection records undesired signal which degrades image quality. Noise is often random with the unknown value, therefore most of the time it cannot be simply removed. The main noise contributions are: noise coming from the image (shot noise), readout noise and dark noise (thermal). Shot (photon) noise is coming from the statistical process of detecting photons by the CCD. For several images which are taken over specific time period, every image has different amount of detected photons. The intensity of taken images will vary and follow the

Poisson distribution (+/- the square root of measured intensity). Therefore, the shot noise can be estimated.

Readout noise happens while CCD charge carriers (from each pixel) are being converted into a voltage (in order to achieve quantitative value) and then amplified before digitalization. That CCD architecture results in generating the readout noise and majority quality of the analogue to digital converter process contributes in the readout noise. That type of the noise does not depend on the exposure time; hence short exposure time generates more noise while long exposure time contributes in the readout noise.

Dark noise will appear from physical processes taking place in the CCD camera itself, not from the signal. Temperature of the CCD while operating will change the number of electrons generated.

Sample/camera stages

While performing experiments two types of stages have been used. Vacuum compatible LTAHSPPV6 high speed motorized actuators (Newport) were used to control position of the camera and the probe. They provide 50 mm/25 mm travel range and about 1 μm precision. Ptychography technique requires precise and small movement, therefore for sample operation SLC-1740 linear positioner (SmarAct) has been used. The accuracy of the SmarAct motor is 1 nm (repeatability 2 μm) with a travel range of 26 mm.

3.4.1 Ptychography Sample Alignment

In all ptychography experiments performed during the project, the pinhole was placed before the sample. Aligning both aperture and sample with the focus position can be challenging in a vacuum environment. In order to achieve that, low IR laser power ($\ll$ mW) was used in the atmosphere, locating all positions of the motors for the focus of the beam relatively for the circular aperture (pinhole) and the sample. When vacuum achieves 10^{-5} mbar, the EUV light is directed onto the CCD camera to identify and improve the spot.

After adjusting parameters which can influence quality of the EUV beam - mainly stability, shape of the beam and maximize the flux (compressor, gas pressure, focus position into the gas cell), the pinhole is placed in the focus of the EUV beam. The pinhole sample was made by focused ion beam (FIB) cutting on SiN membrane (50 nm) plus 200 nm Au coating. Diameters of the circular apertures vary from 2 μm to 20 μm (Figure 3.3).

Mathematical algorithms written by Michal Odstrcil allow for finding the best focus position of needed aperture. In order to find the focus, Newport motors are used to

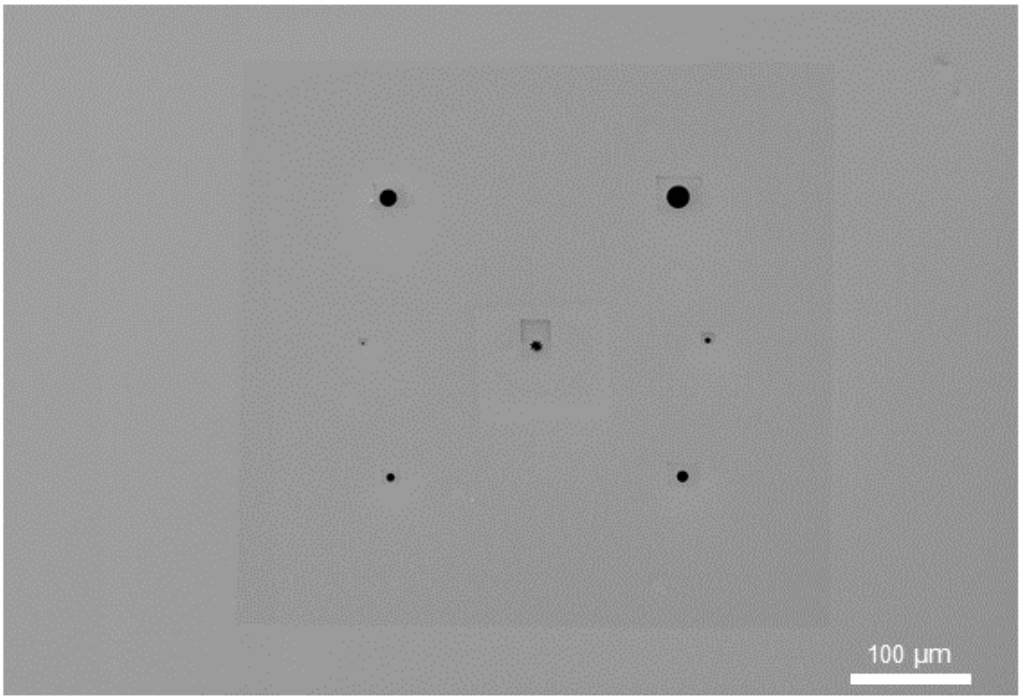

FIGURE 3.3: SEM of the pinhole sample; diameters of circular apertures: 2, 5, 7, 10, 12 (star shape), 15 and 20 μm. First, 200 nm of Au was deposited onto a 50 nm SiN membrane by magnetron sputtering. Then, focused ion beam FIB process has been used in order to etch pinholes. Image taken by Stuart Boden from the University of Southampton

move the pinhole through the focus and the EUV CCD is detecting the beam. After the beam spot is recorded by the CCD, a Gaussian fit is applied to the beam (at each point which is parallel to the beam). The focal spot size and M^2 can be then identified. 2D aperture scanning helps to measure position of the focus. Then, the CCD placed behind the aperture measures the integrated intensity and the Gaussian is fitted to the data. A beam spot can be extracted at each position through the focus.

Typically, for ptychography imaging, 7 μm and 10 μm pinholes have been used. After the focus position of the aperture is identified, coherence test of the source is performed, by using high dynamic range (HDR) method.

High dynamic range (HDR) term is often used in photography or digital imaging; it represents a higher dynamic range than the standard one. HDR helps to recreate larger dynamic range of luminosity in comparison to the standard imaging/photographic techniques. Luminosity is related to the brightness and it is defined as a total amount of energy which is emitter by an object (per unit time). HDR tries to represent similar range of luminosity which can be seen by the human visual system. HDR of an image is achieved by capturing several different exposures of the object and then combining

FIGURE 3.4: First image on the left shows image which is underexposed, the middle image is overexposed. The last image on the right is the final HDR image, merged from the two previous images. It is the most vibrant and the best quality image [77]

them. Ptychography measures dynamic range from the exposure values differences. An increased value of the exposure time represents double amount of light, decreased exposure time represents halving light. Different values of the exposure time can help to illuminate better dark regions of the object, while low exposure time diminishes light in a very bright region. A simple example of an HDR image in ptychography is presented in Figure 3.4 where the HDR image has been merged from 2 images - one overexposed, the other underexposed.

Measured x-ray diffraction coherence pattern of a 10 μm aperture without any sample is presented on Figure 3.5. Color bar is displayed in logarithmic scale. The diffraction data was taken at 29 nm and recorded with CCD camera. We can see fringes interference emanating from the pinhole shape with different phases of waves.

The equation representing HDR imaging is presented by 3.4.

$$img_h dr = sum_i(W_i * img_i)/sum_i(W_i . * t_i) * t_n \tag{3.4}$$

where $img_h dr$ and img_i are HDR image and image achieved by t_i exposure time. W defines the weighting matrix (1 value for measured regions, 0 for oversaturated or unmeasured regions); t_n is the longest exposure time.

Before performing the imaging scan, coherence test has to be executed in order to check and improve coherence of the x-ray light, pivotal for ptyhographic imaging. In pursuance to achieve that, a coherence diffraction pattern is recorded from a pinhole projection. Example of diffraction pattern collected by using HDR represents Figure

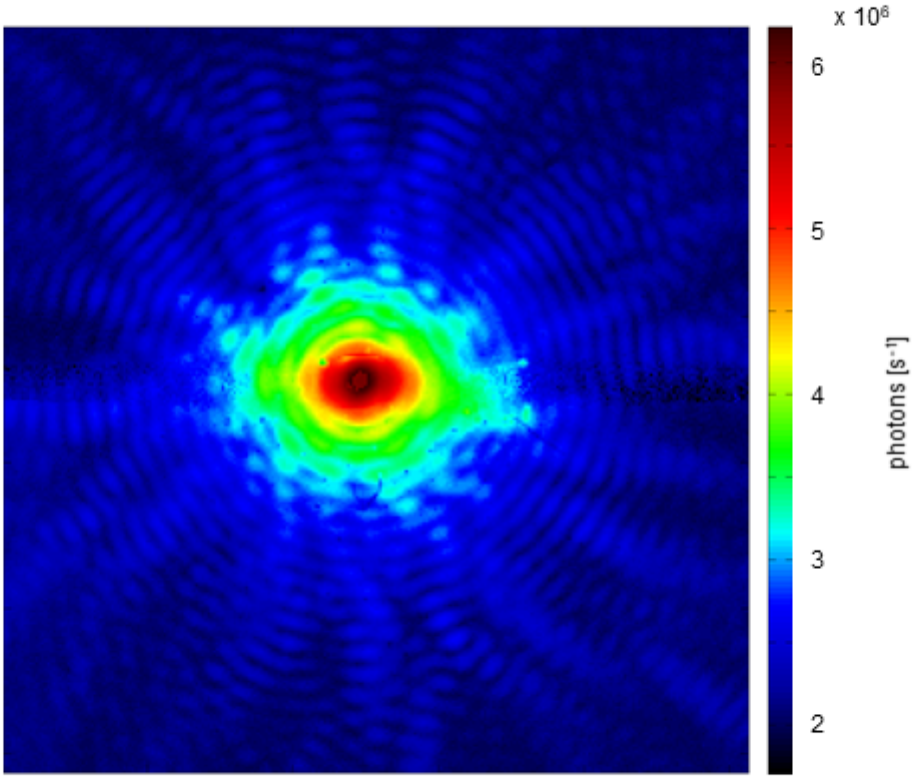

FIGURE 3.5: EUV Diffraction pattern of a 10 μm diameter aperture recorded with a CCD Andor Camera. Strong interference pattern of diffracted waves is an indicator of a high coherence. Coherence is the main requirement for successful ptychography technique

3.5. A coherent EUV light is passing through 10 a μm wide pinhole. We can observe interference of diffracted waves expanding from the center (where the light intensity is high). After coherence test is successful (which determinates a human eye), other steps can be taken to prepare sample for the scan.

The sample is placed behind the pinhole, in the central beam coming from the aperture (in a distance of about 100 μm) by using precise motors. The pinhole delivers scatter from its rough edges. Then, the EUV beam illuminates the sample through the aperture, at the same time transmission maps are taken. Transmission maps help visually choose a particular region of a sample to be imaged. After choosing the scanning area,

ptychography imaging is ready to perform. Figure 3.6 shows part of the configuration setup with motors holding the sample and the pinhole.

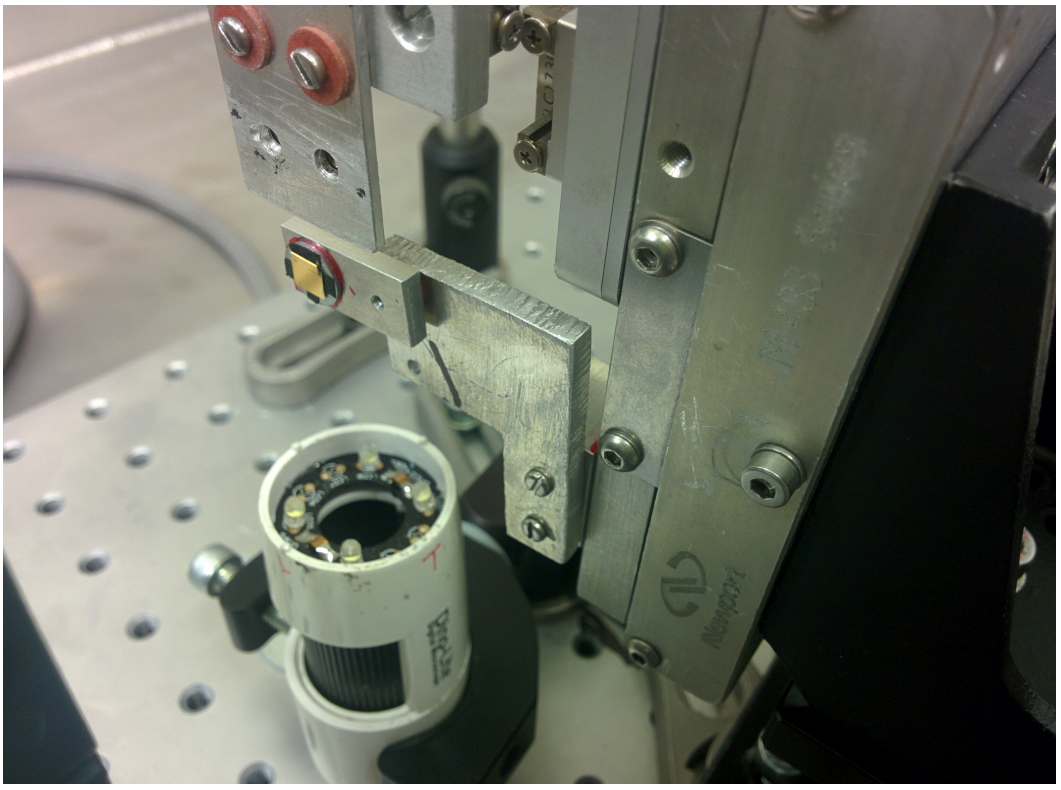

FIGURE 3.6: Part of the configuration system in the chamber. A small gold sample attached is a pinhole. Above it, there is a place for 2 imaging samples. During the ptychography scan, both aperture and imaging sample are placed parallel by using stages with nm precision. A Dino-Lite digital microscope is used to help with the alignment in a vacuum

In Figure 3.7 (a), transmission map (EUV illuminating the pinhole) represents all existed apertures within a sample. Image on the right is a sample transmission map (contains the whole sample), which denotes the EUV light was passing through a pinhole and then sample.

Biological samples are placed onto a membrane which is very fragile. While pumping down/venting the vacuum chamber, a membrane with a sample can be blown if the process is rapid. Figure 3.8 demonstrates neurons sample which has been lost. We can spot a square with a sharp edge where a membrane with neurons was located. High flux of the EUV is passing through the sample which can be compared with 3.7 (b) where the flux is much lower and the light is absorbed by specimens. In that case the sample was being smashed by the pinhole - sample interaction, where the distance between both was about 80 μm. In order to position sample just behind the pinhole all stages need to possess μm precision in all directions.

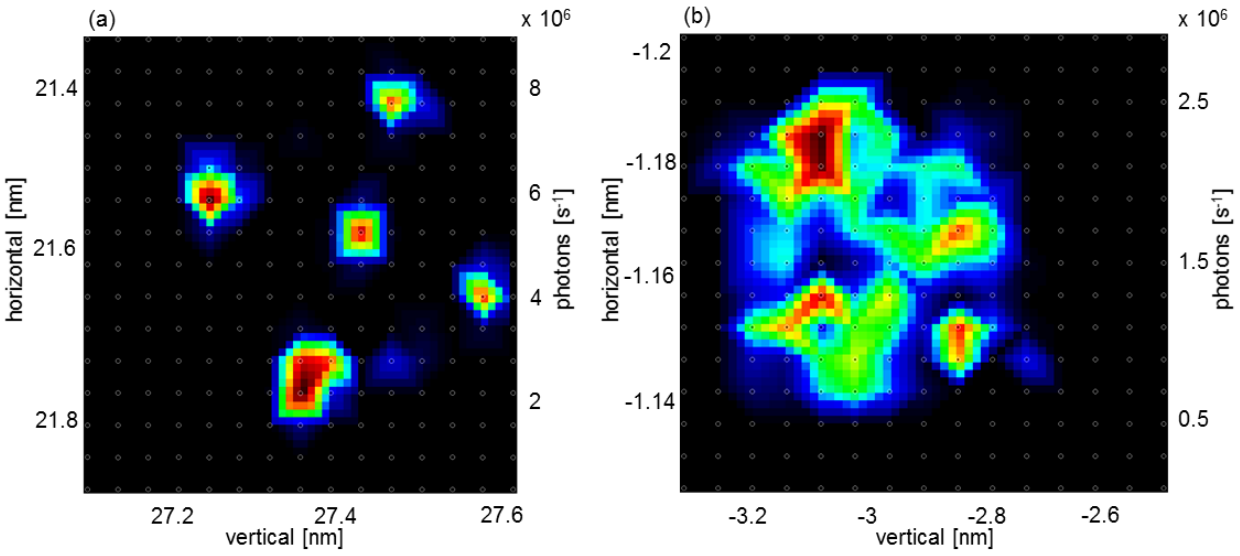

FIGURE 3.7: Figure (a) represents the scanning transmission map of the apertures (7 apertures ranging from 2 μm to 20 μm diameter). Figure (b) is an example of the scanning transmission map of neurons sample placed behind one of the pinhole in a distance of 120 μm

3.5 Image Reconstruction Analysis

In this section results of the transmission ptychography have been presented. All studied samples were neurons extracted from mouse hippocampal left 7 days in culture (DIV7) and 14 days in culture (DIV14). They have been imaged by using far-field transmission ptychography method and then reconstructed by Michal Odstrcil by using ePIE and OPRP methods. Analysis has been performed focusing on the thickness and chemical composition of the objects.

3.5.1 Neurons Structure Identification

In this subsection, few reconstructed images of neurons samples have been provided. As ptychographic images present a visible network of the details inaccessible to see on optical images, an attempt has been taken to identify specimens.

First reconstructed sample is presented on the Figure 3.9 and it shows results from the DIV7 neurons cells. Due to the high EUV flux we can see many details recorded while light was transmitted through the sample. The main part of the neuron is clearly seen - neuronal cell body, soma (4) which provides proteins for axons, dendrites and

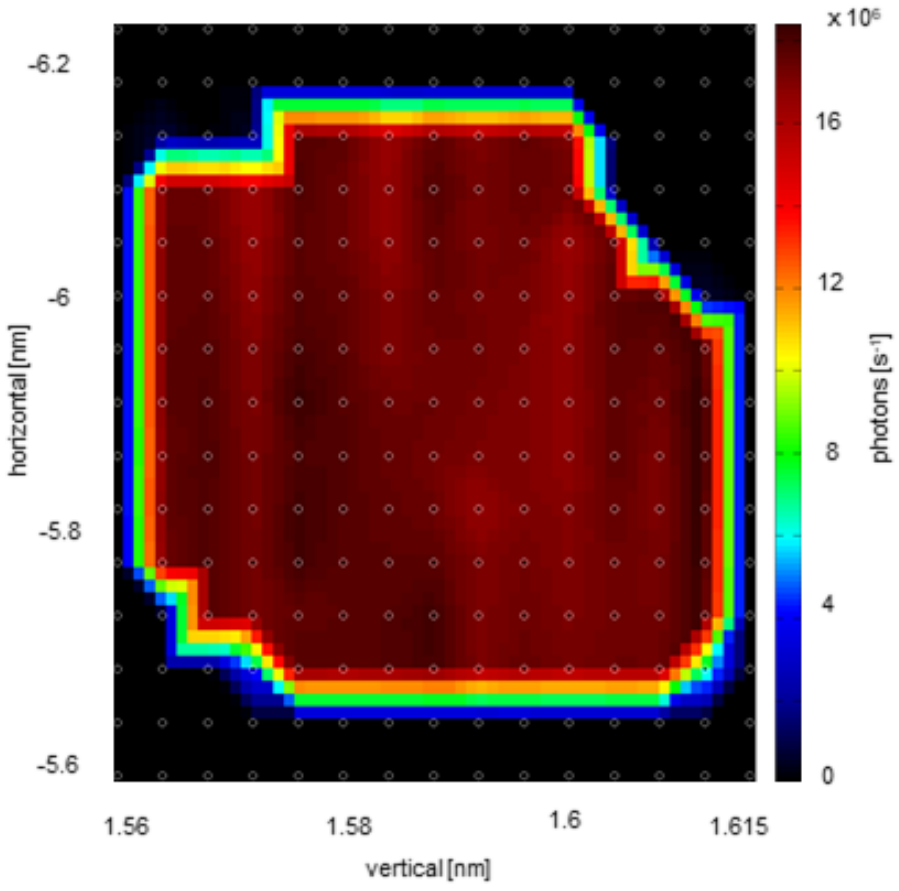

FIGURE 3.8: Example of a broken neurons sample. From shining the laser through the pinhole and then a full sample, we achieve a transmission map of the sample. Onto the image, we can spot sharp edges as an indicator of lost membrane. Also, as we can see the demonstrated flux is high, which means all part of the EUV is transmitted through the sample

synapses. We can spot many axons and axonal branches (Figure 3.9 (2)) which has been developed due to the fact that DIV14 sample represents older structures of neurons. Axonal branches have been formed as microtubules from the parent axon which has been divided and they were able to form other structures such as new axons. (5) is the growth cone coming out of the dendrite and indicating direction of the growth. (6) is filopodia with the bundle of actin filaments which is a migrating cell. (1) shows neuron varicosities whose task is to release a neurotransmitter to surroundings. (3) presents synapses - those are structures between neurons and they permit to pass electrical/chemical signal from one neuron to another.

After imaging process and identification of sample DIV7, an attempt has been taken to image DIV14 which represents dense structure of neurons. In order to see as many details as possible, high EUV flux is required as all neurons have been well developed and many axons and their bundles has been created. Figure 3.10 presents 2 images -

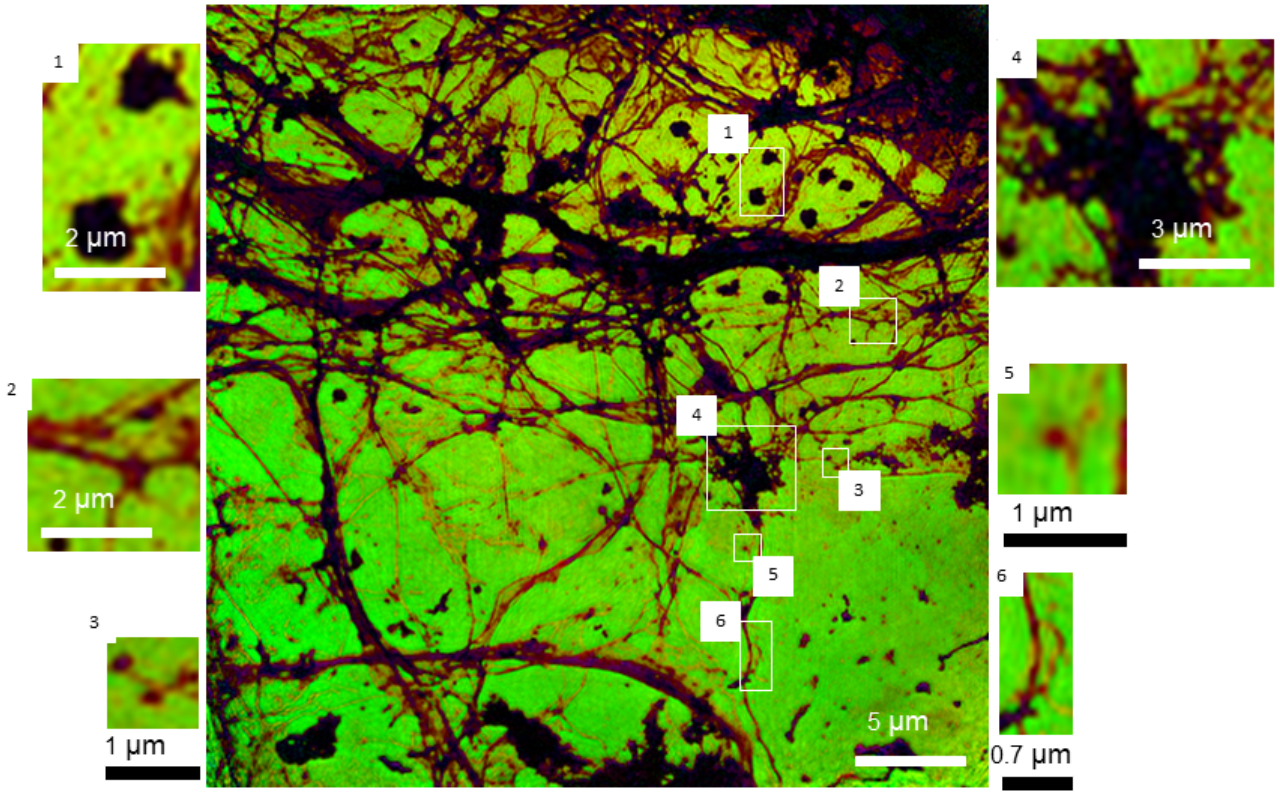

FIGURE 3.9: DIV7 neurons sample reconstructed from the ptychographic data taken during the scan. We can see many tiny details which were possible to obtain due to the high EUV flux transmitted through the sample. Morphology of the imaged feature is compatible with the shape of the neurons, their axons and neurites. (1) neuron varicosities; (2) axonal branches coming from axon; (3) synapses; (4) neuronal cell body (soma); (5) growth cone from the dendrite; (6) filopodia. Scale bar 5 μm

the one on the right was obtained from an optical microscope and presents full DIV14 cell sample on a SiN membrane (500 μm). The red square indicates region which was selected for ptychographic scan of about 50 μm size. On the red square we are unable to see many details of the structure. The left image is the reconstructed area of the scan and many details can be spotted. As ptychography techniques provide phase information, speciments thickness can be extracted from the collected data. The amount of visible details cannot be seen by using traditional optical microscope.

Figure 3.11 shows results of the DIV14 neuron cell sample scan. The sample was reconstructed by Michal Odstrcil (using ePIE and OPRP). Figure (a) presents the HSV reconstruction of the full CCD scatter patterns (FOV of 50 μm of the sample). Figure (b) and (c) are the average reconstructions of the probe (at the plane of the sample) and the aperture respectively. Figure (d) shows the amplitude of the full FOV sample. We can see high sensitivity in amplitude characteristics for the spectral wavelength. Lower energy sources (EUV) are able to achieve high resolution of a very thin structures of

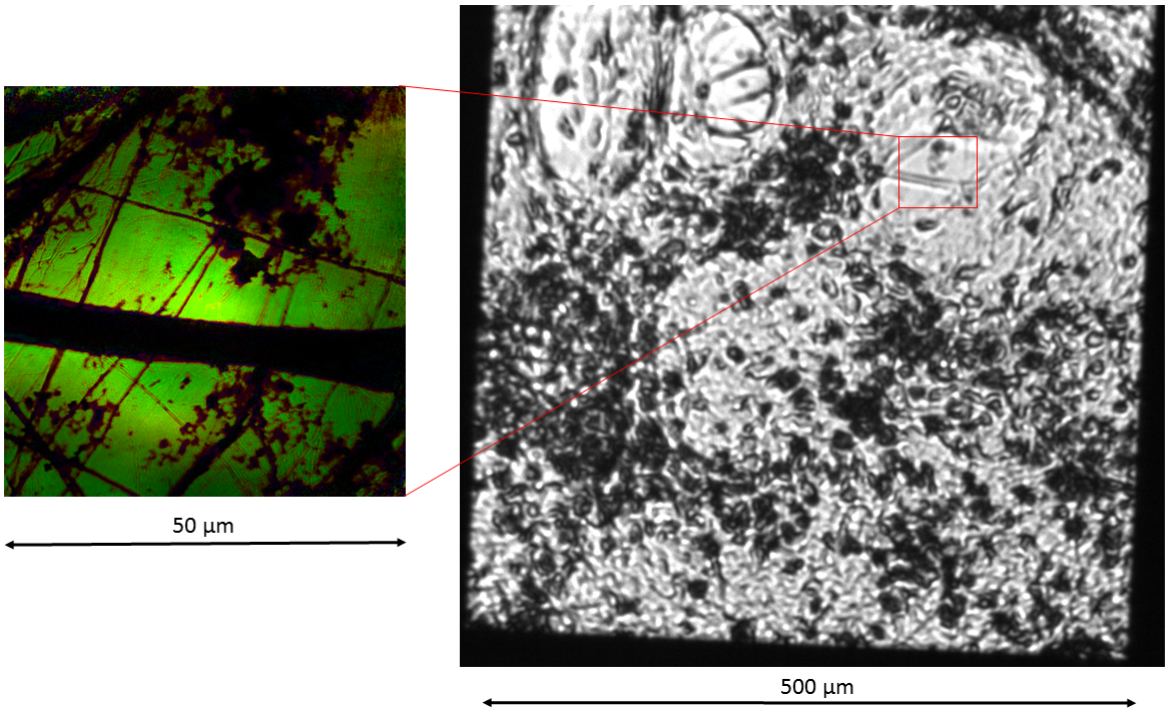

FIGURE 3.10: The image on the left presents the reconstructed image from the DIV 14 neuron cell sample; the image on the right presents the optical microscope picture of the full DIV 14 neuron sample. The red square on the right image is the part which was imaged by using ptychography technique. As we can notice, ptychography imaging allows to see more details and provides phase information from which data about thickness and structure of a sample can be extracted

an object. Figure (e) is the phase only of the reconstructed image. Large variety of different structures, including the tiniest can be seen, as transmitted flux was enough to extract information.

Figure 3.12 presents reconstructed DIV14 sample image with optical images of the same scan region. Figure (a) shows magnification of the isolated area where a very dense meshwork of axons was spotted. After 14 days in culture neurons structure significantly developed and we can observe many tiny objects of the tissue cultures, which are impossible to see on the Figure (d) and (e) - optical images (reflected and transmitted light). Part of the neurons cells can be easily distinguishable - a long fiber. Spines going from a neuron can be also spotted. In the same area of optical microscope images, tiny structures are invisible - the area looks blank.

Figure 3.13 presents variety of sizes among different structures identified on the reconstructed image (DIV14). Sizes of the identified structures vary from hundreds of μm to 70 μm. Those are axons and dendrites. The sample is a good representation of neurons where formation of axonal branches is greatly developed.

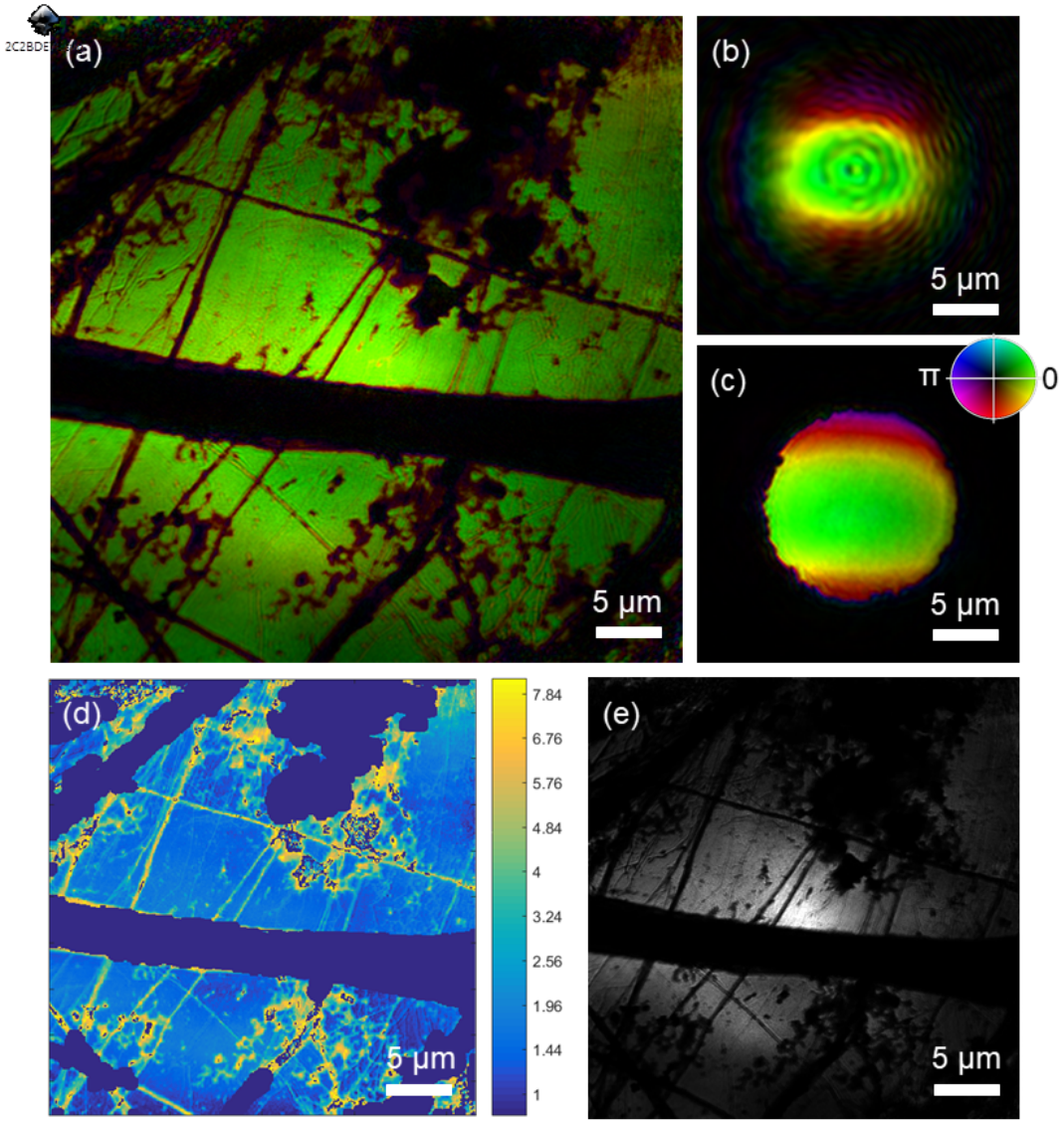

FIGURE 3.11: DIV14 neurons. (a) HSV reconstruction. (b) probe electric filed reconstruction on the sample. (c) electric field of the neurons sample after the filed has been back propagated (using ASM to the plane of the pinhole). (d) shows amplitude only of the reconstructed region and (e) shows phase only of the reconstructed image

Additionally, chemical composition of specimens identified within a sample can be extracted. As ptychography technique provides information about phase shift and amplitude which can be useful for basic calculations of the sample thickness. Both values give information about material properties - δ and β. As the ratio of imaginary and real part of the refractive index δ/β does not depend on the thickness [78], for the recognized components (therefore known values of refractive index) thickness can be extracted.

The imaging method is valid for thin specimens. Due to the EUV attenuation, higher values of thickness cannot be extracted.

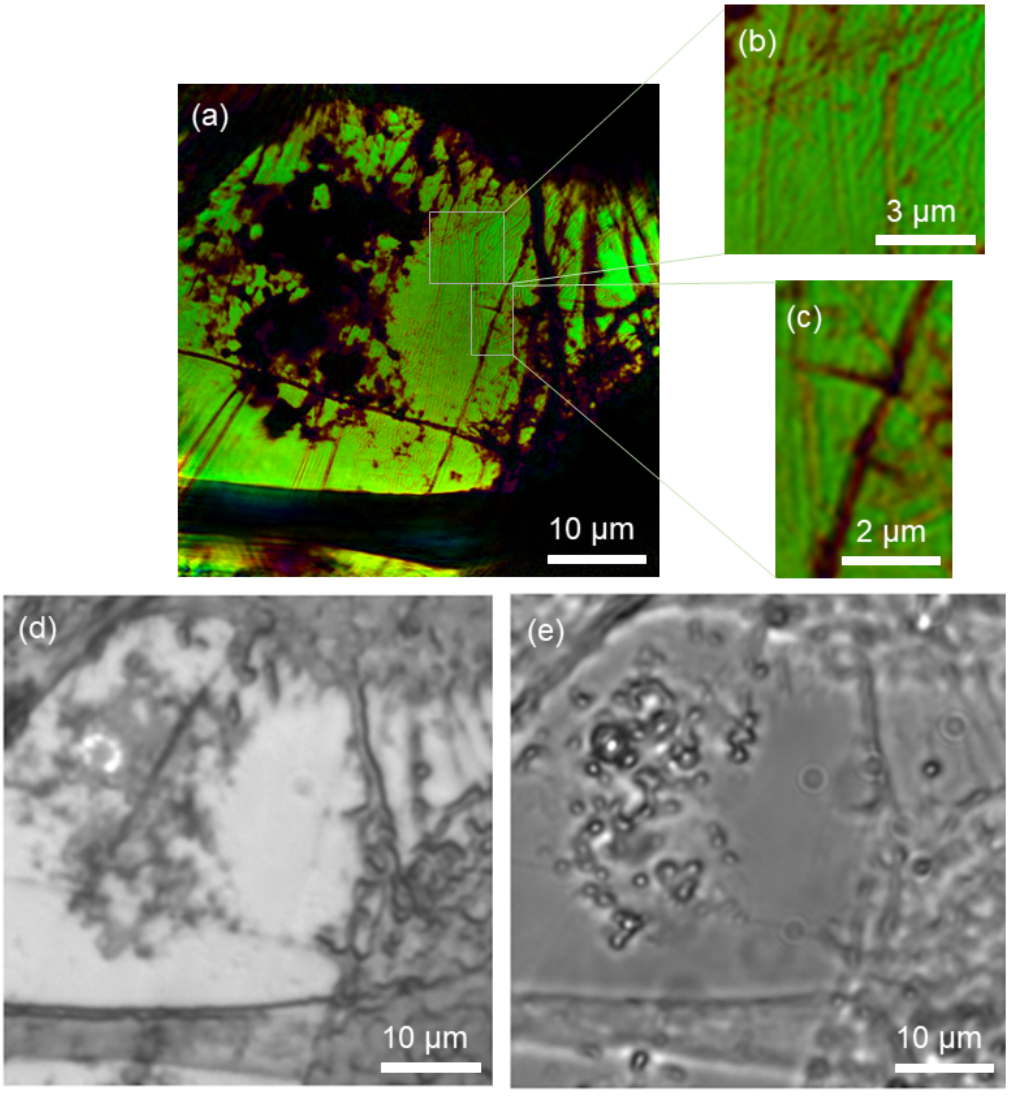

FIGURE 3.12: (a) is the final reconstructed image of hippocampal neurons sample with magnification of some regions (b) and (c). We can identify bunch of structures (mainly axons with dendrites). (c) and (d) are optical images taken of the same region (transmission and reflection mode) and we are unable to observe tiny structures visible on the reconstructed object. Also, thanks to the contrast in the image (a) specimens are clearer to identify. Magnification of (c) and (d) does not improve visibility of species

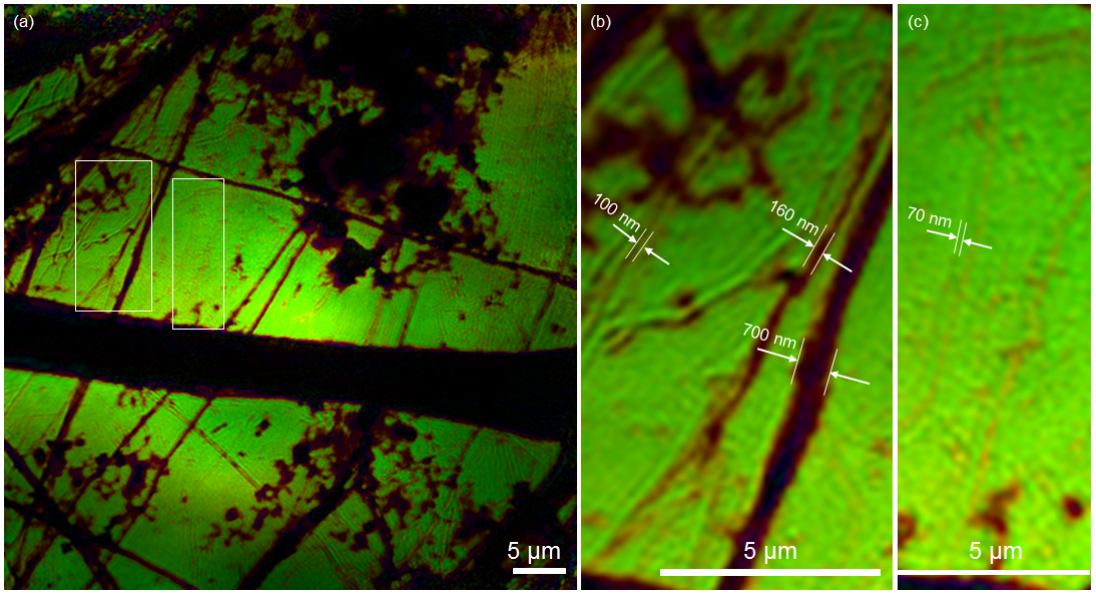

FIGURE 3.13: DIV14 neurons. (a) Reconstructed image with fine details possible to see through EUV radiation, (b) and (c) presents magnification of the scanning region with the structure thicknesses. Sample reconstructed by Michal Odstrcil. Parameters of the ptychography scan: exposure 10 s (datasets contained 454 images), cropping 2, readout 3, temp -40 degrees centigrade, step size 2 μm, pinhole diameter 7 μm, probe to sample distance 90 μm, binning 2. Ptychographic phase image of neurons was compared with traditional optical images. As we expected, the reconstructed image appeared with high resolution features resolved

3.6 Summary

In this section details of ptychography technique have been presented and the method has been used for imaging biological samples – neurons. In the demonstrated experiment, soft x-rays light generated by HHG process was used to illuminate the sample. From the data collected during the scan, mathematical algorithms were applied to reconstruct scanned images. Reconstruction process allows us to subtract the phase of the HHG and to achieve information about the imaging sample. Specimens have been found and identified providing more details about neurons. Additionally, ptychography process allows us to identify thickness and composition of the specimens presented in the sample.

It has been shown that performing ptychography imaging require high photon flux, high coherence and stability of the beam. All the above parameters can be impacted by the optical system design and environment (such as temperature, building vibrations which has a crucial effect on the beam stability). One of the method which has great influence on the x-rays flux is separation of the fundamental laser beam from the harmonics by the beam splitter optical device. Improvement of optical separators can enhance the flux and gives the possibility of imaging more substantial samples, such as mature neurons,

which require more light to pass through the sample. An attempt of imaging DIV21 was found very challenging due to the difficulties of identification the sample in the vacuum chamber and later, in passing light through the sample. There are still many opportunities in the Ultrafast X-ray Laboratory to improve efficiency of the laser and imaging processes.

Ptychography is a very powerful technique, helping to explore biological samples. It allows for imaging without lenses, therefore errors coming from imperfect optics or various forms of aberrations (an issue for very short wavelength) are absent. With comparison to the optical microscope, images retrieved from ptychographic imaging showed higher resolution. The main potential is to improve the resolution achieved by ptychography technique. This requires shorter wavelength, therefore improvement of the optical system.

Chapter 4

Adaptive Optics for EUV Wavefront Control

It has been presented in Chapter 3, that resolution in imaging determines visibility of fine features of an image. As resolution depends on the wavelength of light, shorter wavelengths such as x-rays can provide higher quality images. Nevertheless, high absorption attributed to many materials in the EUV range is one of the limitation to achieve high quality optics. While using such a short wavelength many challenges appear which are not considered while using longer wavelength of light.

Another factor which influences quality of the EUV optics are aberrations in the optical system and wavefront distortions. Aberrated light coming from optics to the camera increases problems with the image quality. By making an effort to correct wavefront distortions, a highly resolved object representing a source of detailed information can be achieved. Technology which helps improving performance of optical systems by correcting wavefront deviations is adaptive optics. Although adaptive optics is a well-established method, it has not been used in EUV wavelength of light. We tested piezoelectric deformable mirror's adaptation and responses to EUV wavelength of light. Preliminary results were experimentally demonstrated and reported for the first time.

In the following section the work was performed in the Ultrafast X-ray Laboratory at the University of Southampton, at the University of Padova (Italy) with Institute for Photonics and Nanotechnologies in Padova collaboration. Additionally, x-ray reflectance data was obtained at the BEAR beamline at ELETTRA synchrotron radiation in Trieste (Italy). The following people were involved in fabrication of the mirror and performing experiments presented in the thesis: Peter Baksh, Stefano Bonora, William S. Brocklesby, Alain Jody Corso, Magdalena Miszczak, Piergiorgio Nicolosi and Maria Gulielmina Pelizzo.

4.1 Piezoelectric Deformable Mirror Design

Operation in the EUV spectral range requires multilayer mirrors to reflect light by interlayer interference. In this section a piezoelectric deformable mirror (DM) has been developed and presented in the visible light and then in the EUV. Performance of the mirror has been measured at ELETTRA synchrotron in Trieste and at the University of Padova. Functioning of the device was demonstrated by using HHG at the University of Southampton.

Mo/Si multilayer mirrors on a Si wafer substrate have been fabricated by using magnetron sputtering by Prof. Zhanshan Wang at Tongji University in China. It was optimized for 30.4 nm (d=16.4 nm, Γ=0.82, N=25), 5 deg incident angle (Figure 4.1).

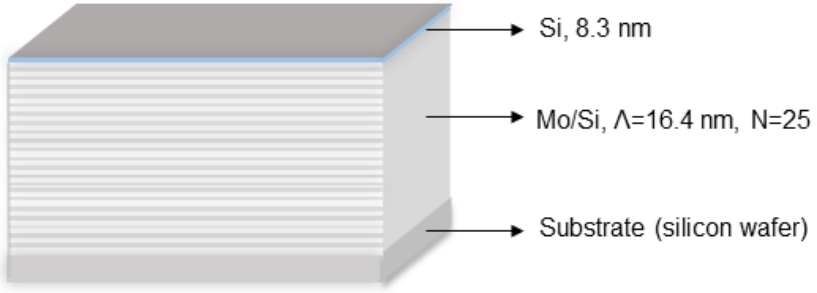

FIGURE 4.1: Multilayer mirror as a base to build a deformable mirror. Alternating layers of Mo/Si were deposited onto Si wafer substrate by magnetron sputtering and optimized for 30.4 nm wavelength and 5 deg incident angle (d=16.4 nm, Γ=0.82, N=25). Multilayer structure was fabricated by the group of Prof. Zhanshan Wang at Tongji University in China

To the back surface of the mirror, a small piezoelectric actuator has been glued. Another identical actuator has been attached to a Si wafer only in order to study other properties, where multilayer mirror does not influence the results but Si wafer is sufficient for the experiment.

Figure 4.2 (a) presents Mo/Si multilayer mirror mounted onto a mirror's holder. The centre part is the actual multilayer mirror (a rectangle), while the part behind the mirror is an aluminum piece/ring designed to hold the mirror; (b) is a diagram presenting front part of the mirror for better understanding. (c) is the picture demonstrating the back surface of the mirror taken out of the holder. It consists of a piezoelectric circular actuator to which wires are attached and then connect to the mirror' controller; (d) is another diagram demonstrating back surface of the mirror. (e) is a cross-section of the device for better understanding.

For the primary tests we decided to use only one actuator attached to the multilayer mirror in order to make all experiments simpler. More actuators attached to the mirror

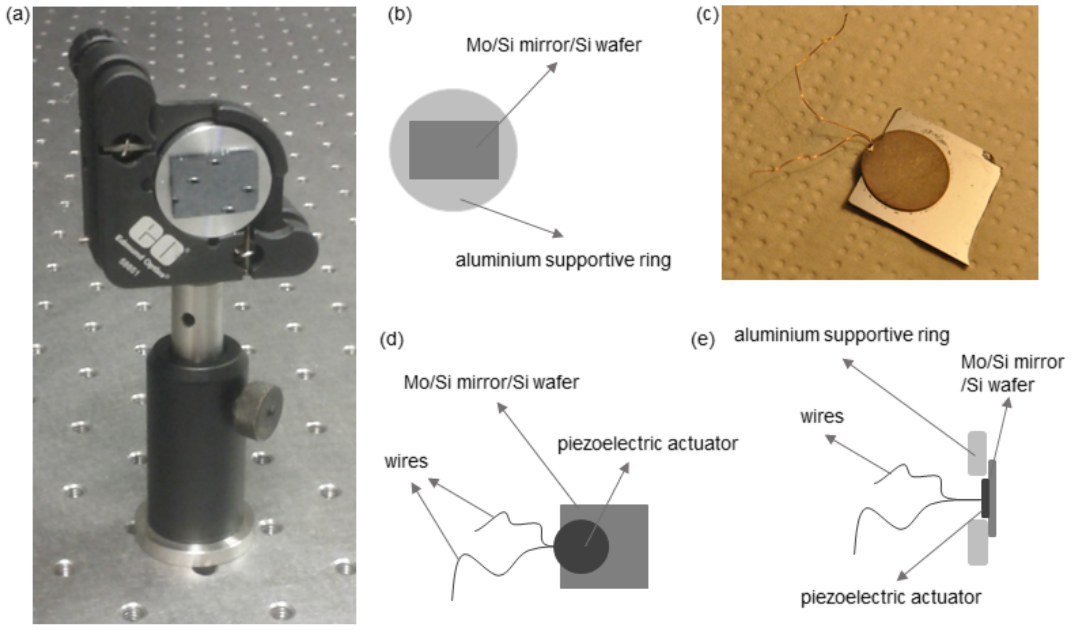

FIGURE 4.2: (a) presents Mo/Si multilayer mirror attached to an aluminum ring which plays a supportive role for the mirror; (b) is a diagram presenting front surface of a DM. Picture (c) presents back side of the mirror, where we can observe wires coming out of the piezoelectric actuator attached to the mirror; (d) is a diagram for better understanding (c) and (e) is a cross-section of the whole device mounted onto a holder

would allow for better control/correction of the wavefront but at the same time they can introduce more complications. At this stage one piezoelectric actuator was adequate to test some properties of a basic DM and proof that it can successfully work with the EUV light. In later phases, DM with more actuators will be tested to provide varieties of wavefront manipulations.

4.2 Deformable Mirror Performance

In this section performance of the mirror has been examined. Voltage applied to the actuator bent mirror multiple times, then the influence of that process on the mirror has been studied. Another aspect to consider was how attachment of the actuator to the back surface of a delicate multilayer mirror can affect the device.

4.2.1 Hysteresis Curve Measurement

One of the important features of piezoelectric materials is nonlinear hysteresis, the existence of which complicates the control of actuators. We studied hysteresis of our mirror

(a piece of silicon wafer) by applying voltage to the actuator and by using Zygo GPI-4 XP Interferometer in order to present the data. Simple diagram of an interferometer principle is presented in Figure 4.3. A beam splitter (glass coated with Ag) splits into two identical halves a coherent beam of light. More precisely - half of the light passes through a beam splitter and half is reflected. One part of the beam goes onto a mirror, then to a detector and it is considered being a reference beam. The other part travels an optical path and is being reflected by a second mirror, then goes to the same detector as the first beam. Phase difference between two beams will change light intensity on the detector. Both beams overlap, interfere and create pattern with dark and light areas. Dark areas are places where both beams interfere destructively, light - constructive interference occurs. The interference pattern gives information about optical path length.

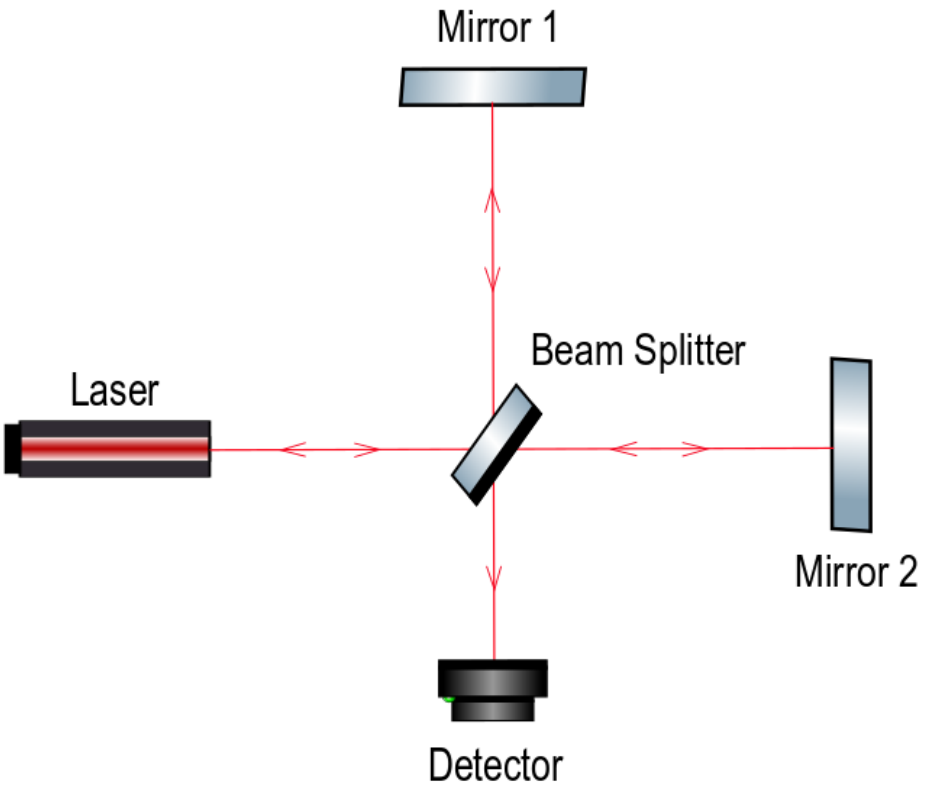

FIGURE 4.3: Principle of interferometer. Common configuration consists of a beam splitter and two mirrors. A coherent beam from a light source travels onto a beam splitter where it splits into two identical beams. Both beams have different optical paths and after their reflections from two mirrors, they travel onto a detector. The path difference creates an interference pattern onto a detector, which analyzed evaluates wave characteristics, properties of a material or other properties which are interested in the experiment; rewritten from [18]

Nanometric structure of a multilayer mirror is very fragile, therefore applying a voltage

to the actuator can cause structure changes along with reflectivity shift. In order to verify the potential impact on the mirror's reflectance some stress tests on DM has been performed.

Initially, DM was actuated up to 0.5 V and down to -0.5 V and results were monitored by using ZYGO interferometer, where each bending cycle, Peak-to-Valley (PtV) was registered. The effect of deformations on the mirror is shown below on the hysteresis curve presenting the stroke versus voltage driver. Interferogram showing surface displacement due to the voltage applied is shown in the Figure 4.4. It is one of the example showing fringes visibility as a results of interference, provided by interferometer. We can observe alternating dark and light regions called fringes as a result of constructive and destructive interference. A path difference of a half wavelength will result in destructive interference, while within a path difference of 0, constructive interference will be produced.

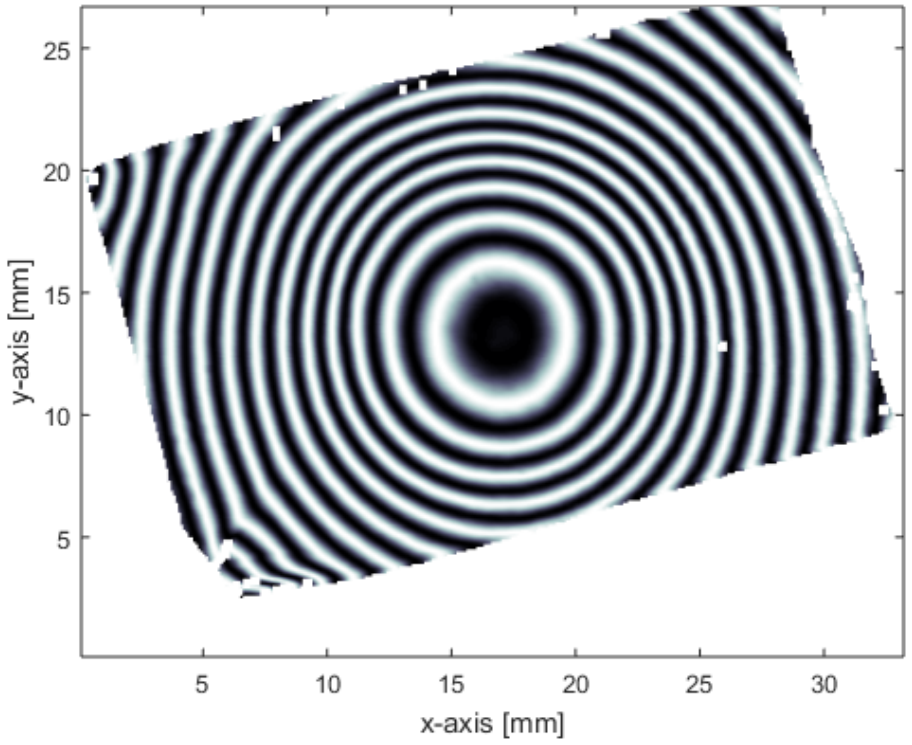

FIGURE 4.4: Interferogram with the surface deformations after applying 0.5 V to the actuator. Interference pattern is created by constructive (light color) and destructive (dark color) interference. It is a result of two different path lengths coming from two beams of light. White regions are indicating constructive interference while dark regions destructive interference

Additionally, interferometer shows surface displacement which is a good way to understand what is happening to the surface of a mirror after applying some stress. On Figure 4.5, surface wavefront map is presented where attention can be paid to the changes of

the surface while applying different values of the voltage. At the beginning surface is at relaxed position which means no voltage applied and as a consequence, the surface should be flat. There are two factors why this is not happening in our case. Gluing an actuator to the delicate mirror's surface produce some tension which can already influence the surface of a mirror. The second factor is connected with the stress applied. As voltage causes bending of a mirror, the surface wavefont is no flatter even in a relaxed position. This could be reduced by using more actuators onto a mirror's surface which by adaptive optics technology can compensate and fix the wavefront.

As voltage increases, wavefront surface changes and the displacement is higher, about 2.38 μm while applying 0.5 V and -2.10 μm with -0.5 V applied to the actuators.

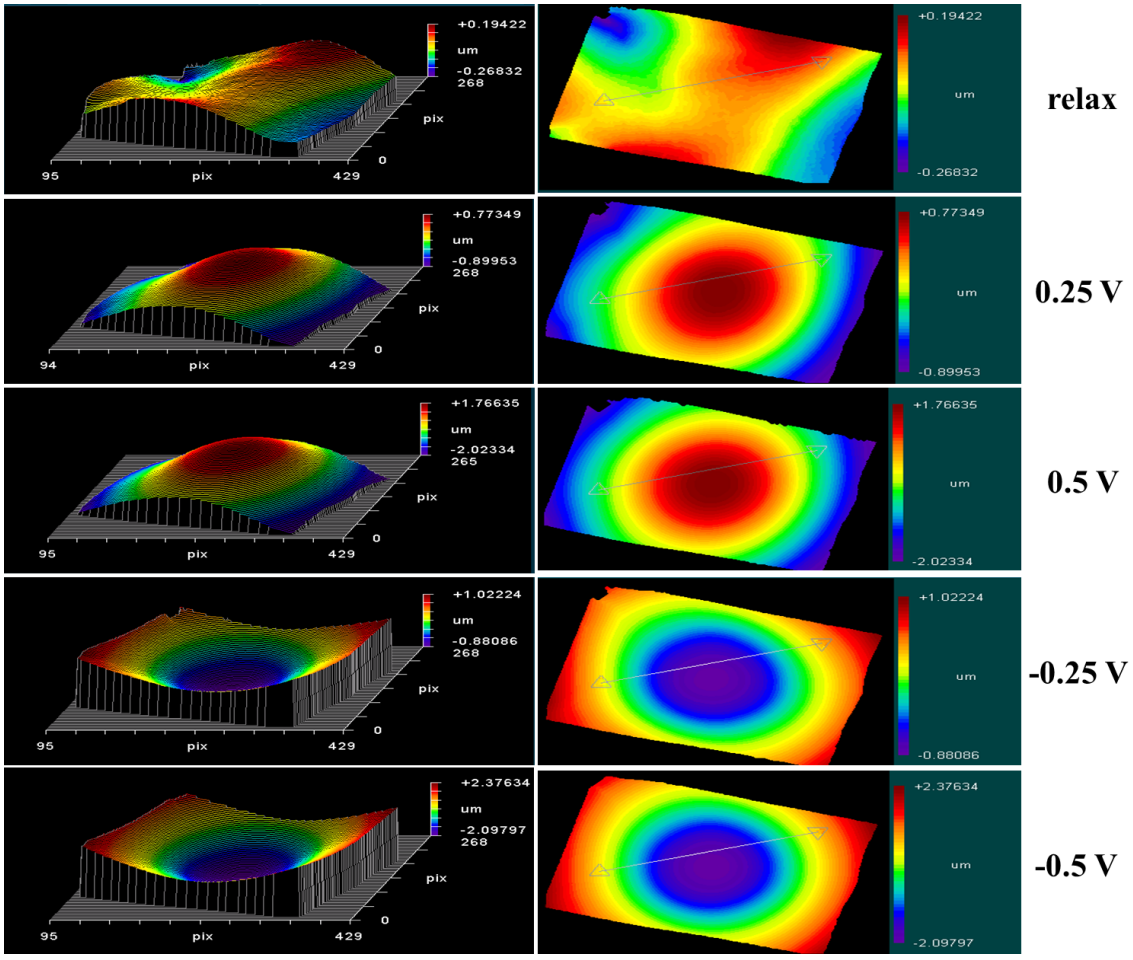

FIGURE 4.5: Surface wavefront maps after applying voltage to the one actuator (sample relax, 0.25 V, 0.5 V, -0.25 V and 0.5 V). We can recognize changes of the surface according to the voltage applied. The highest displacement of the shape of a surface (the lowest figure) shows values from +2.38 μm to -2.10 μm (vertical axis)

As we can see on Figure 4.6, the hysteresis test started with the actuator in a relaxed position (which means no voltage). Then voltage was applied from the value 0.5 V to -0.5 V with the step of 0.1. While increasing the value of the voltage, strong hysteresis

can be observed which is associated with the displacement curves of actuators, which determine displacement.

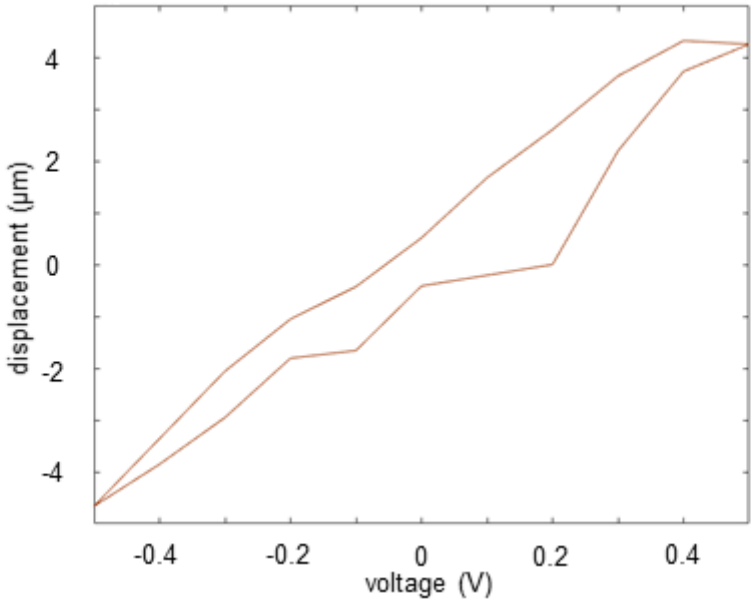

FIGURE 4.6: Hysteresis curve of Si piece with piezoelectric actuator attached. In order to verify stability and behavior of mirror's surface voltage was applied from value 0.5 V to -0.5 V with the step of 0.1. As we can observe on the graph, strong hysteresis appears with higher voltage values

According to the results, it can be deduced that achieved hysteresis is acceptable, although influence of the applied voltage on the surface of our mirror will decrease response of changing shape of a surface. For our purpose and first tests the above hysteresis curve gives us information about the speed in the response while applying voltage onto the actuator. At that stage, the hysteresis curve is tolerable but it can change after and it may need some improvements while applying more difficult tests. Another representation of a surface displacement after applying some stress to the actuator of a mirror is shown on Figure 4.7. Again, relaxed position does not show a flat surface as it has been already bended. We can clearly see the magnitude of mirror's deformations.

4.3 Deformable mirror surface data analysis

After testing how bending of the mirror can affect its surface, it is important to study performance of the mirror by creating a specific wavefront. Optical performance of the DM can be tested by studying its response through generating a specific wavefront. In order to do that a spherical wave was generated using pinhole filtered He:Ne laser beam and deformable mirror was used to represent the same shape. Data from wavefront sensor of the deformable mirror (Mo/Si on the Si wafer optimized for 30.4 nm, one

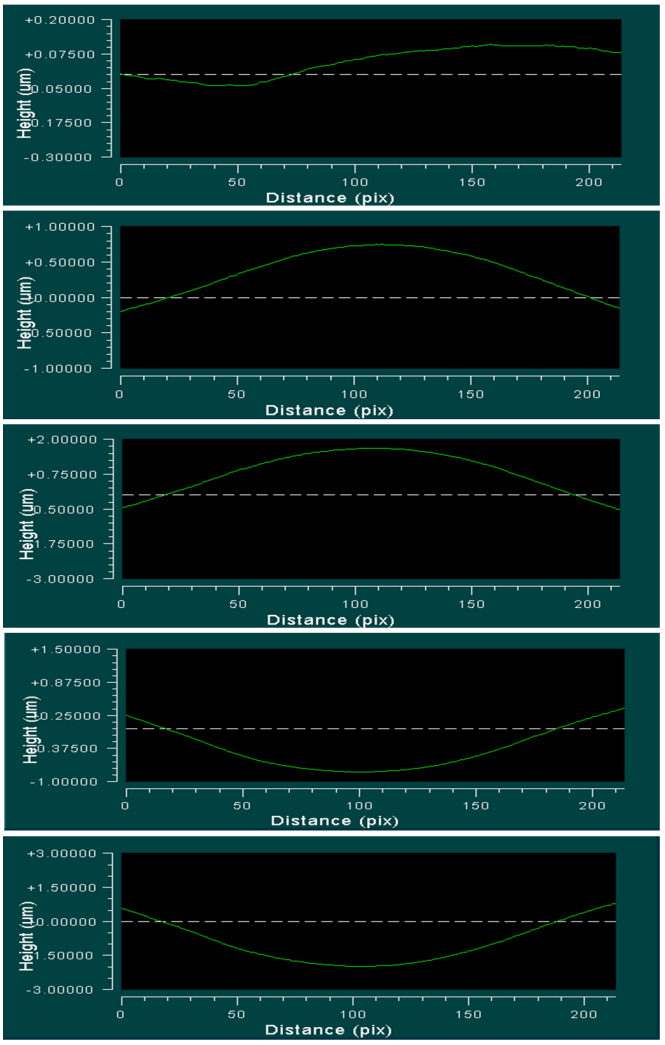

FIGURE 4.7: Surface/wavefront after applying voltage to one actuator (sample relax, 0.25 V, 0.5 V, -0.25 V and 0.5 V). Again, the top image represents surface without any stress applied to the surface of the mirror. Then respectively 0.25 V, 0.5 V, -0.25 V and 0.5 V were applied voltage caused changes of the wavefront

piezoelectric actuator attached, d=16.4 nm, Γ=0.82, N=25) were then analyzed. Figure 4.8 shows measured phase distortion and the requested AO mirror phase deformation.

Both figures seem to be visually very similar, which would mean the wavefront generated by the laser and by bending the DM (our new requested shape of a surface) is the same. In Figure 4.8 (c) and (d) we are able to observe the differences, which is 5% between the modeled and measured data. Only small scale of the wavefront was left uncorrected. According to the data presented, the mirror's performance seems promising as it should be capable to correct large scale wavefront aberrations.

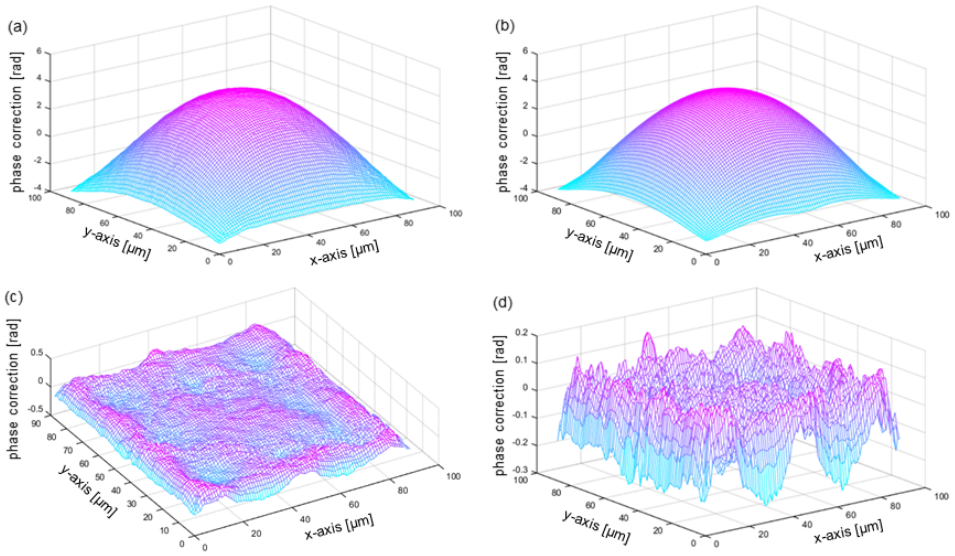

FIGURE 4.8: Deformable mirror's performance of creating given shape of a wavefront. (a) presents measured phase of the DM by the wavefront sensor; (b) is the phase correction of the DM; (c) and (d) present the difference between the requested shape of the wavefront and the wavefront phase achieved. The difference between the modelled and measured data is about 5%; μm scale

4.3.1 Reflectance Measurement of the Deformable Mirror

In this subsection, the most important property of a multilayer mirror has been tested - reflectance. DM created during the project was designed to work with one actuator. In the EUV spectral range, precision of a multilayer structure plays a crucial role and any modification will significantly reduce reflectance of the device. DM working as beam manipulator will bend multiple times to produce a desired shape of wavefront, hence there is a high possibility that the nanometric structure of the mirror will change. The reflectance can be also affected while attaching an actuator to the delicate and fragile surface of a mirror. Therefore, combination of bending with high voltage applied may influence mirror's performance and can affect interfaces in the composition of a structure. A sensitive and thin surface of a mirror may destroy and the optics lifetime can be lower than associated with a mirror without adaptive optics applied. Due to the high production costs of DM, it is desirable to use EUV optics for a long time, as long as reflectivity value can be accepted. We put an effort on studying influence of the stress applied to the mirror on the reflectance data. Few samples with and without AO were fabricated and then reflectance was measured.

As mentioned before, Mo/Si multilayer mirrors (3 samples) optimized for 30.4 nm wavelength with or without piezoelectric actuator attached to the surface were investigated.

To the sample number 7 and 10 piezoelectric actuators were attached (one per one multilayer) and then mechanical stress was applied. We are aware of the fact that actuators attached to the surface can affect multilayer formation but at the same time one actuator produces the same shape of the surface. Magnification of the deformation can change which is associated with different stress values. Therefore, we are hoping to prove high stability of our deformable mirrors.

Sample number 7 (AO) was treated with 0/+150 V bias for ten times and 0/-150 V bias for ten times. In April 2013, reflectance for all 3 samples was measured at ELETTRA synchrotron in Trieste concerning that the oxidation can also influence surfaces. In April 2015, sample number 10 (AO) was treated with 100 Hz frequency stress during 80 min. Then, reflectivity measurements for the same samples were repeated in the same month with the goal of comparison of all measurements executed in 2013 and 2015 (Table 4.1 for better understanding).

Both chemical elements of the multilayer structure, Si and Mo are characterized by high mechanical strength. By applying long lasting stress or strong mechanical stress, decrease of the reflectivity could be identified as permanent deformation of a sample. While small stress is applied, small atoms displacement can be observed (according to the ductility of chemicals) and after removing stress, atoms will go back to the same original position of the equilibrium. Therefore, in theory there is a possibility of long lifetime performance for Mo/Si deformable mirror.

TABLE 4.1: Measurements performed at ELETTRA synchrotron in Trieste in 2013 and 2015. Sample no. 7 and 10 were multilayer mirrors with adaptive optics applied while sample no. 12 was without actuator attached to the mirror

No. sample	Measurement in 2013	Measurement in 2015
7 (AO)	-150/150 V stress	2nd measurement
10 (AO)	1st measurement	100 Hz 80 min stress
12	1st measurement	2nd measurement

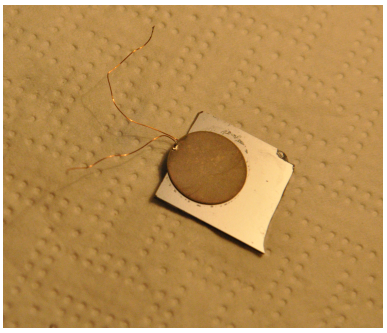

FIGURE 4.9: *Mo/Si* multilayer mirror with actuator attached. The back view

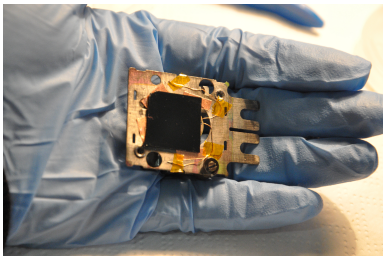

FIGURE 4.10: Sample ready for the experiment, attached to the holder of the beam line. Actuator is present on the back of the surface

All measurements at the BEAR beam line at ELETTRA Synchrotron (Trieste, Italy) in April 2015 were performed with details provided in Appendix B.

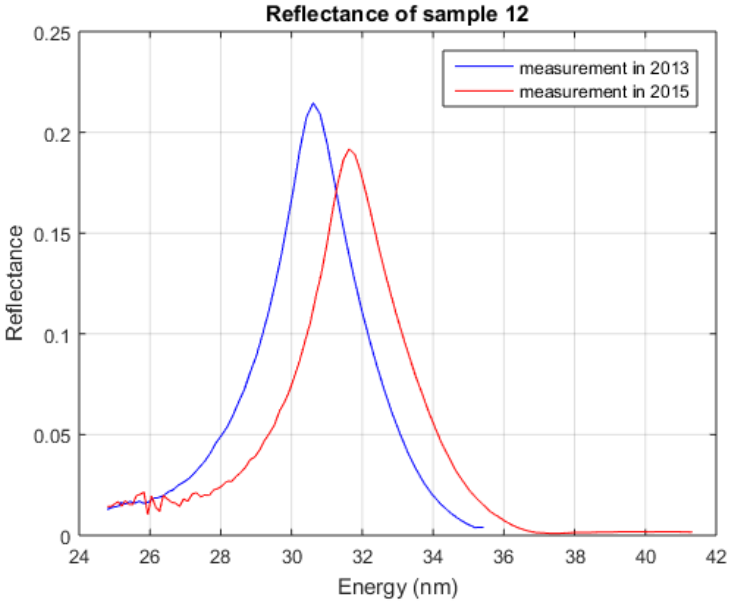

FIGURE 4.11: Sample 12 was a Mo/Si multilayer mirror without AO applied. In 2013 reflectance measurement was taken and it showed about 18.5% reflectance. After 2 years, in 2015, measurement was repeated with the same conditions and reflectance of a sample showed about 21%. A sample was not treated with an AO; therefore, surface was not mechanically affected. A decrease in reflectance by 3.5% seems to be connected with surface aging - interaction between Mo and Si could cause formation of another layer from the reaction of both chemicals. Also, oxidation of the surface could influence changes in reflectance. It has not been proven as the structure was not studied in details

Figure 4.11 presents two measurements of a sample number 12 with no adaptive optics applied. Measurement performed in 2013 showed 21% reflectance, while in 2015 18.5%, therefore shift by 3.5% was observed. As the multilayer mirror did not have AO applied, as a reason in reflectance changes we consider surface oxidation and/or changes in the

structure of the mirror. Some chemical reactions could have taken place between Mo and Si layers which could introduce other layers, therefore the original structure with reflectance expectations will not apply anymore. Nevertheless, structure has not been studied in details, therefore those are assumptions.

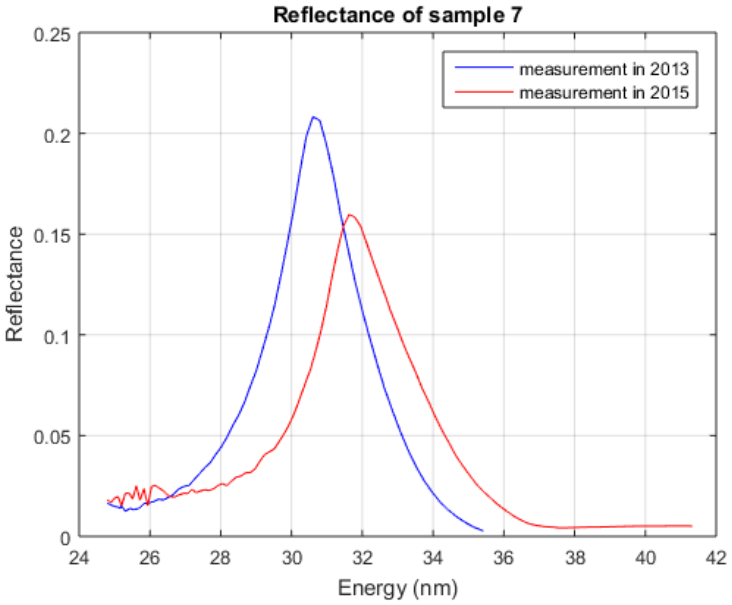

FIGURE 4.12: Sample 7 was a Mo/Si multilayer mirror with AO applied. In 2013 reflectance measurement was taken after applying -150/150 V stress to the actuator and therefore bending the surface of a mirror. Reflectance after taking the measurement showed about 16%. After 2 years, in 2015, measurement was repeated with the same conditions and reflectance of a sample showed about 21%. A sample was treated with an AO; therefore, surface was mechanically affected. A decrease in reflectance by 5% seems to be connected with three factors: surface aging, oxidation and possibly the most crucial - AO applied

Figure 4.12 presents another multilayer mirror sample with AO applied. Deformable mirror was bent several times by applying stress of -150/150 V to the actuator placed onto the back surface of a mirror. Bending can cause changes in the structure. After performing measurement in 2013, the sample showed 21% of the reflectance. In 2015 the measurement was repeated (same conditions) and reflectance of the sample showed 16%. Therefore, after 2 years the reflectivity dropped by 5%. It can be associated with oxidation or sample aging (as in case of previous sample no. 7). The main reason we expect to be surface bending. If we compare with sample no. 7, the reflectivity drop is bigger by 1.5% and we expect those 1.5% of the reflectance to be linked with AO.

Figure 4.13 shows reflectance measurement performed in 2013 for DM. Then in 2015 DM was treated with 100 Hz stress during 80 min and the reflectance dropped from 21.5% to 19%. The difference in reflectance of 2.5% is less significant than the one associated with sample 7 as it seems that AO and bending the surface did not change reflectance. Possibly smaller drop in performance can be associated with a specific composition of

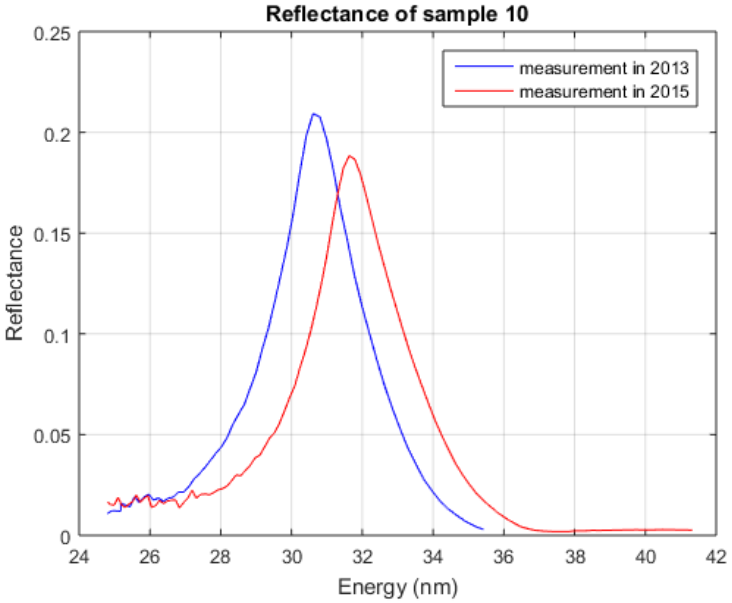

FIGURE 4.13: Sample 10 was a Mo/Si multilayer mirror with AO applied. In 2013 reflectance measurement was taken and showed 19%. Then in 2015 sample was treated with 100 Hz frequency stress applied to the actuator during 80 min. Measurement was repeated and showed about 21.5% reflectance. Three factors could affect the sample: oxidation, aging (structure changes due to the reactions between alternating layers) and stress applied to the mirror

a sample, varying in comparison with others. Also, attachment of an actuator could produce much less influence onto the structure.

According to the above results, we can deduce that actuator attachment and bending the surface does not have a significant influence on the structure distortion and stability of a sample. The reason of higher drop in the reflectivity of the sample with lower stress (sample number 10) than the sample with higher stress (sample number 7) are possibly properties of a specific composition, also the influence of a glued actuator. Sample with lower stress showed more significant difference in the reflectivity value than sample with higher stress applied. It is also probable, that we are not able to observe the differences in the composition changes (therefore in the reflectivity) just directly after the stress was applied. The measure performed in 2015 was taken directly after the stress applied. Possibly another measurement in a longer distance (1-2 years) would provide lower reflectivity (for further investigations).

While analyzing the data and comparing results from 2013 and 2015, the first observed change in data was a wavelength shift evident in all performed measurements. It can be clearly visible in Figure 4.11, where the central pic from 2013 measurement appears roughly at 30.65 nm, while in the measurement from 2015 at about 31.8 nm. Therefore, the difference between both peaks of about 1.1 nm is observed.

There are two possibilities of the shift in wavelength. First assumption was wrong calibration of monochromator. If we look into the data deeper (Figures), we can observe not only energy shift but also width of the peak has changed. It is visible on the graphs where the energy shift has been corrected (Figure 4.13 and Figure 4.12). As we can see data from 2015 presents narrower peak compare to the peak from 2013. It appears on all the of the Figures and it is proportional.

While considering Bragg's Law (Equation 2.3), when wavelength is longer, the thickness of a bilayer has to increase. In case of our data, results from 2015 would indicate larger bilayer thickness. The bilayer structure could change, hence after 2 years another layers could be distinguished as a reaction between Mo and Si. Nevertheless, the structure has not been checked after 2015 therefore there are no evidence for modification of the multilayers.

4.4 Deformable Multilayer Mirror in the EUV Spectral Region

In this section, deformable multilayer mirror was used in the EUV spectral wavelength. For the first time, experiments performed lead to demonstrate adaptive optics technology in short wavelengths.

The first study was to observe spot of the deformable mirror. We expect surface theoretically flat, to be slightly curved as from previous sections we know that voltage applied and attachment of the actuator will affect performance of the mirror.

Focus position experiment in the following section has been performed in the Ultrafast X-ray Laboratory in Southampton. EUV source based on HHG technique has been used - all details are provided in 3.3.1.

On Figure 4.14 surface of the DM used in all experiments in that section is presented. The EUV beam was directed onto the DM and then recorded by the CCD camera. The quality of the surface is low as we can notice speckles onto the whole area. Although deformable mirror needs improvement due to its surface, it did not have significant impact for the experiments presented in this thesis.

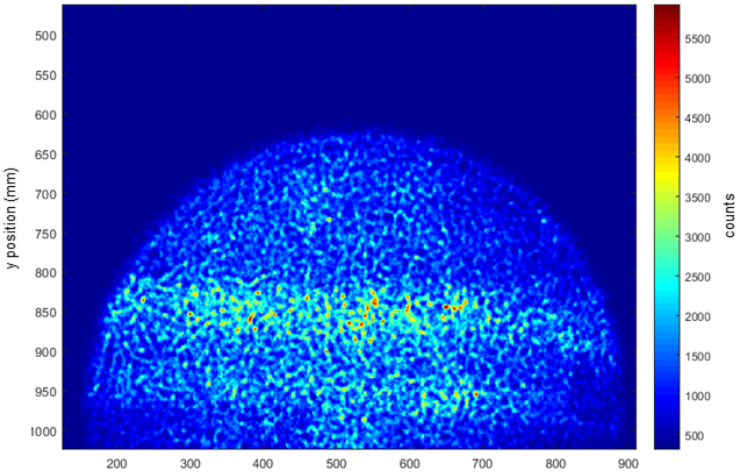

FIGURE 4.14: Deformable spot recorded by the CCD camera. We can notice low quality spot with speckles onto it. As other deformable mirror was checked and another multilayer mirror without AO - all provided the same quality images, which should be improved for future experiments

4.4.1 Focus Position Changes with Deformable Mirror

Capability of changing focus position by deforming DM in the vacuum chamber has been tested. Curvature of the mirror was adjusted by applying specific voltage values to the mirror. Then, CCD camera recorded position of the focus.

EUV coming into the experimental chamber after being separated with IR laser by Al filters was directed onto the Mo/Si deformable multilayer mirror. Then, the beam was reflected towards a spherical multilayer mirror and focused onto a CCD camera. Figure 4.15 presents the sketch of the setup.

Deformable mirror's ability to change the focus position of the optical system has been then tested. The curvature of the DM was bending by voltage applied to the actuator. CCD camera set at a fixed position for every measurement registered spectrum. Figure 4.16 demonstrates two images which are corresponding to specific voltages applied to the mirror.

By applying -73 V spot of the EUV increases while bending the mirror with +81 V makes the spot smaller. It is a proof that DM can work in a vacuum environment. The capability of bending the mirror was +/-3 μm.

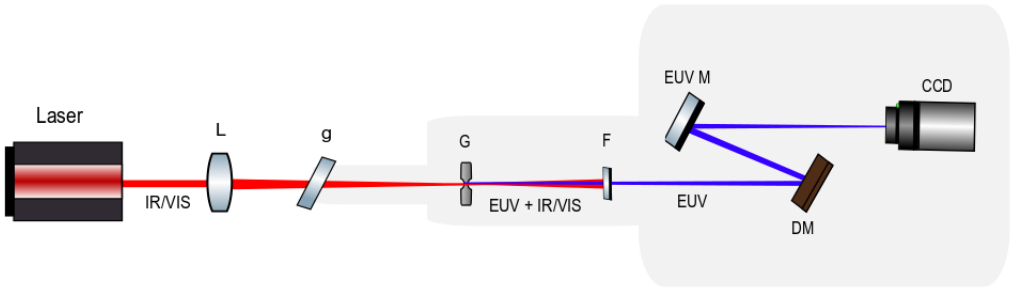

FIGURE 4.15: Configuration of a setup testing DM performance in a vacuum system. EUV is being generated through HHG process and the light enters the experimental chamber after being separated from the IR light by Al filter (F in the image). After that, EUV beam goes onto a deformable mirror (DM) where it is being reflected to the EUV multilayer mirror and then goes directly onto the EUV CCD camera. In the image, L is lens, g is glass, M - mirror, G - gas cell, F - filter, DM - multilayer mirror adapted to adaptive optics (deformable mirror, DM), EUV M - multilayer spherical mirror, CCD - EUV camera

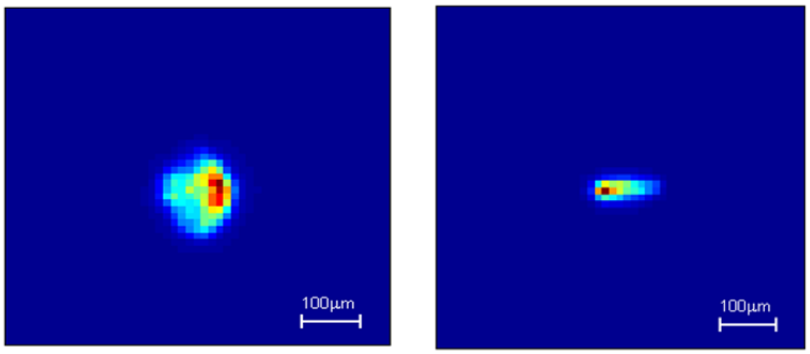

FIGURE 4.16: Focus position changes with different voltage values applied to the actuator of the DM. -73 V causes the spot to increase while +81 V makes spot much smaller. Spot obtained from an EUV beam being reflected by DM and then by the spherical multilayer mirror towards the CCD camera. The capability of bending for the mirror was +/-3 μm

4.4.2 EUV Wavefront Integration with Deformable Mirror

The next experiment performed was to monitor EUV wavefront by using Hartmann wavefront measurement. Aside of a typical Hartmann sensor with an array of lens, an array of apertures was used. An aperture of a size 20 μm was placed onto a stage with a high precision allowing for nano movement of the pinhole. Then, an aperture was moving across the beam (in steps by 450 μm) and has been scanned. Detector was placed close to the mask (61 mm) in order to prevent diffraction from interfering arrays. Diffraction patterns have been collected by the CCD camera. Hartmann sensor has been created by a superposition of all single collected images. Figure 4.17 presents Hartmangram.

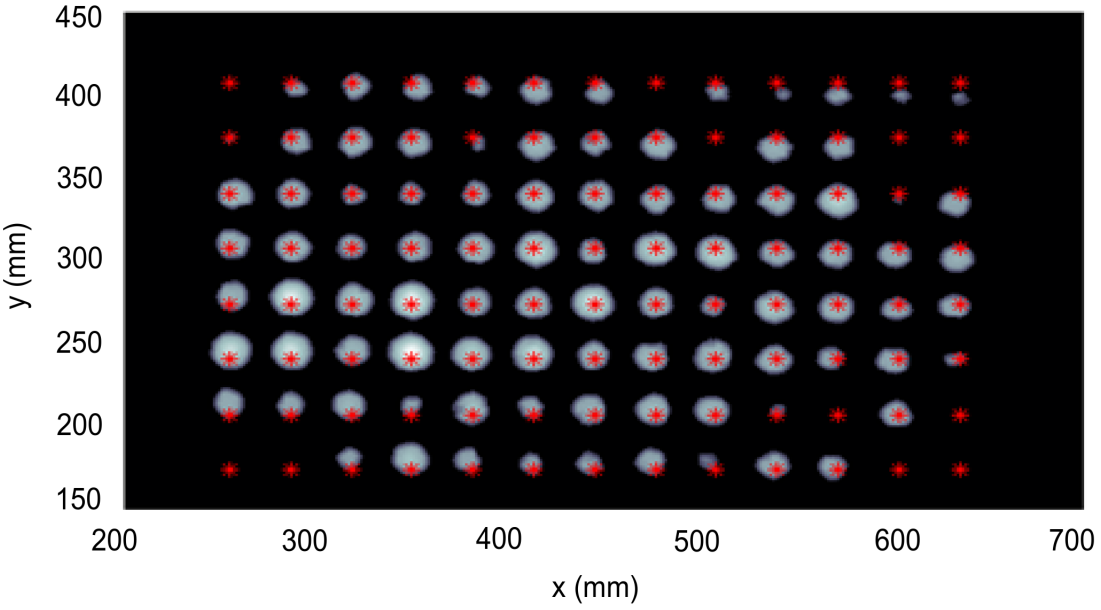

FIGURE 4.17: Hartmann wavefront sensor measurement. The experiment was conducted by using a pinhole of a size 20 μm has been scanned across the beam (in steps of 450 μm). The hartmangram was created by superposition of all images. Red stars represent reference grid points while grey areas are Hartmann spots

Every position corresponds to one single image. The pinhole was scanned through the aperture and the image was computed by superposition of all images. Then, the diffraction pattern has been collected for all the images. Each aperture created the centroid position and then information about wavefront were extracted. Red stars represent reference grid points while grey areas are Hartmann spots. The wavefront was measured for different voltage applied to the DM.

Additionally, Figure 4.18 represents wavefront reconstructed from the data where 0 V (a) and 100 V (b) were applied to the mirror. Therefore, the first image refers to the DM with a flat surface, the second image curvature manipulated. Evidently, changes of the wavefront while applying 100 V stress to the device can be noticed.

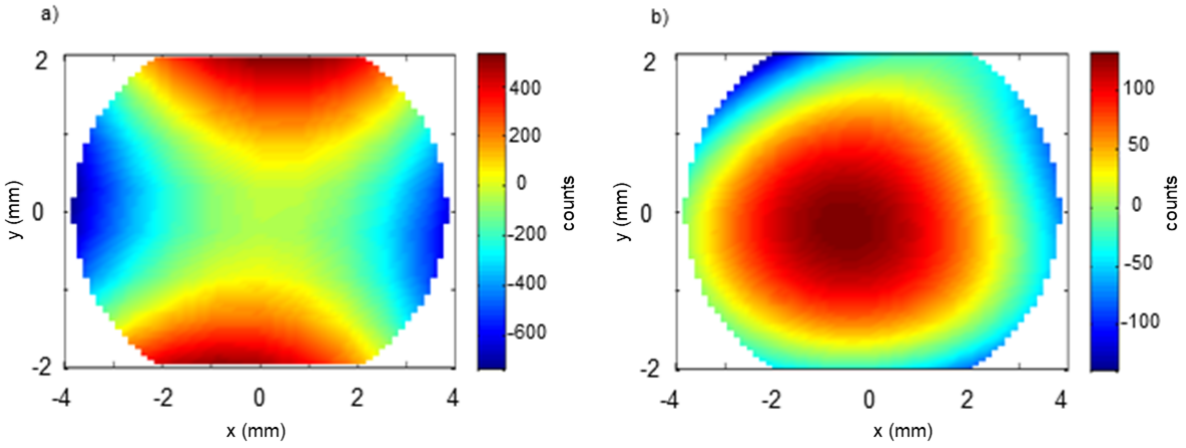

FIGURE 4.18: EUV wavefront reconstructed from the Hartmann measurement data where 0 V (a) and 100 V (b) was applied to the mirror. The first image refers to the DM with a flat surface, the second image represents DM's curvature manipulated. Color bar in nm

4.5 Summary

In this chapter, piezoelectric DM has been tested for the first time in the EUV spectral range. The device was built by fabricating Mo/Si multilayer mirror which was optimized for 30.4 nm wavelength. Piezoelectric actuator was glued to the back surface of the mirror. The most important properties of the device have been studied such as hysteresis, surface deformations and reflectance of the samples. Surprisingly, piezoelectric actuator does not seem to affects reflectivity of the mirror. Finally, DM was tested in the EUV spectral range which was proven by changing the soft x-rays wavefront while applying stress to the actuator. Although quality of the DM was not the highest, experimental data seems promising and DMs can be used in other experiments where they could improve the wavefront.

Modulation of the EUV wavefront is a powerful tool, therefore the great motivation for building deformable devices such as DM. Our preliminary results from the performed experiments proved DM can work in the vacuum systems without any issues. In future, the plan is to perform more sophisticated experiments, such as ptychography imaging with wavefront correction. This process could improve the beam profile which can be distorted in the vacuum chamber during imaging process due to local temperature changes. It would allow for higher efficiency ptychography imaging methods, therefore quality and resolution improvement.

Another goal is to use DM with more than one actuator attached to the back side of the multilayer mirror. Such a mirror can reconstruct many different shapes (represented by

Zernike polynomials) and allow for precise wavefront correction. This requires designing, fabricating and testing stage. It is obvious that reflectivity of the mirror will decrease due to flexibility of the mirrors bending. In order to achieve more detailed information about parameters of the DM with multiple actuators, similar mirrors without actuators attached to the surface has to be fabricated and compared with the DM.

Another step could be considering using more advanced adaptive optics techniques, which are adaptive lenses.

Chapter 5

MoS_2 Beam Splitter as a Separator for HHG Process

Beam splitter is one of the optical components which is extremely crucial in HHG process as it allows for filtering IR/VIS light from a weak EUV signal. Without the above separation, many experiments would not be possible to perform, as the high power laser could destroy the camera/sample during the imaging process. Selection of materials which could effectively transmit and/or reflect different wavelengths is complex as besides physical properties, elements have to fulfil chemical requirements likewise. The most important is high thermal stability while dealing with high intensity IR light. Ideally, materials should either reflect all the EUV and completely transmit the IR laser or transmit all the EUV with reflection of the IR. Placing the beam splitter at the Brewster's angle allow to notably increase its efficiency. A brief description about filtering has been given in the previous sections. Detailed characterization of materials and experimental analysis is presented in the next sections. All reflectivity measurements were performed in the Ultrafast X-ray Laboratory in Southampton.

Filter which is being used in the Ultrafast X-ray Laboratory in Southampton is an Al piece (200 nm) which reflects IR light and transmits EUV.

5.1 Simulations for a Novel MoS_2 Beam Splitter

Dichalcogenide materials have been recently of a great interest as they are used as transistors in electronics [79],[80]. With the fact that nanometric precision of their production has been developed at the University of Southampton [81], some simulations have been performed in order to study their properties as potential candidates to use as

a beam splitter. Calculations were implemented for some few dichalcogenides materials from which the MoS_2 showed promising results and it has been selected as a material for further investigation.

Originally, the idea was to fabricate MoS_2 onto any transmitive substrate and subsequently measure IR light reflectivity. It came out that smooth MoS_2 surfaces cannot be effortlessly built onto any substrate by using simple fabrication method. Depending on the thickness of a sample and substrate (Si wafer, glass or sapphire) different processes need to be used.

5.1.1 Laser Reflectivity

From the previous sections we know that if the fundamental laser beam is horizontally polarised with the sample set at the Brewster's angle, the reflection coefficient goes to zero. Calculations by using Fresnel equations were performed for a MoS_2 sample in order to determine Brewster's angle.

Figure 5.1 presents reflectivity for the laser with different polarisation state. Reflectivity for the sample with laser being vertically polarised is high, about 40% of IR light in theory will be reflected. Placing MoS_2 at the angle of 77 deg, which is Brewster's angle, would allow for low reflectivity of the laser light at a specific polarisation state (p -polarised laser).

Primarily, theoretical EUV reflectivity were measured for different thicknesses of a MoS_2 sample. This allowed for selection of the most promising thickness. Afterwards, as it has been observed that a substrate onto which MoS_2 is fabricated influences reflectivity - calculations were made to select a substrate with the greatest reflectivity. Then wavelength and angle changes were studied to determine how they can affect reflectivity. In the end reflectivity measurement for two samples successfully fabricated has been performed.

5.1.2 EUV Reflectivity

Reflectivity of a specific sample depends on many factors such as sample thickness, substrate, wavelength and angle spread. Therefore, all those factors were studied in pursuance of the best MoS_2 sample characterization.

Sample thickness

Thickness of a material being used as a beam splitter influences reflectivity of the EUV light. It is important to optimise thickness of a sample so the reflectivity of short

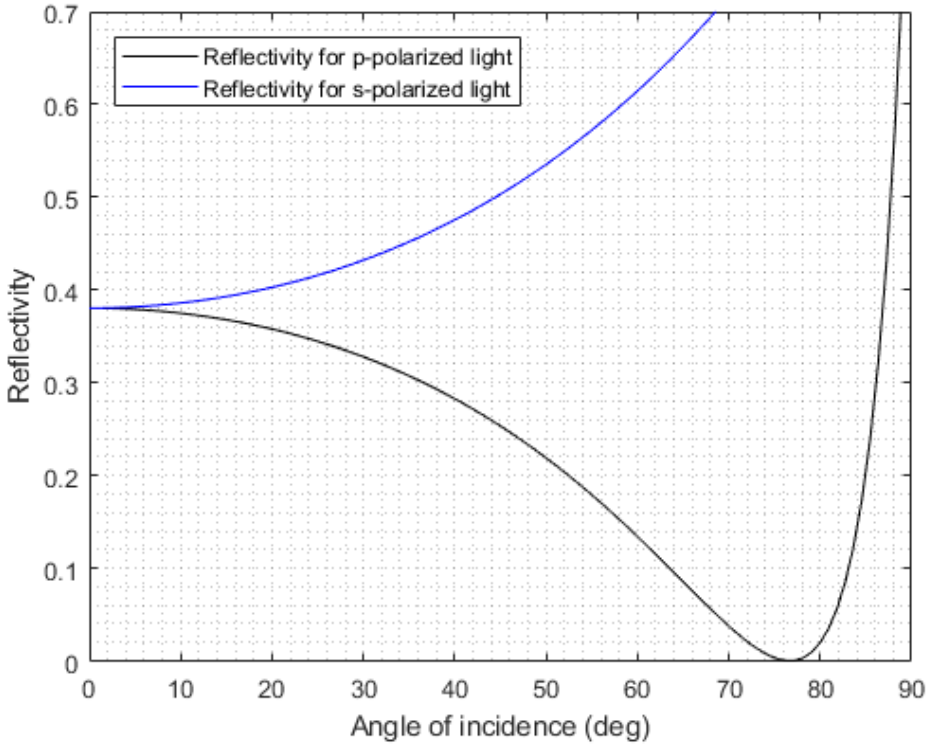

FIGURE 5.1: Reflectivity of MoS_2 for the laser *p*- and *s*-polarised. Different polarisation states of the laser provide contrasting reflectivity. Placing sample at a specific angle, which in case of MoS_2 is theoretically 77 deg, will massively reduce reflectivity close to the zero value. Apart from attenuation of the large amount of the IR laser, another very important requirement in the process of a beam splitter selection is to reflect ideally the whole portion of the EUV light while placing the BS at the same angle (in this case 12 deg for the EUV). MoS_2 at a wavelength of 790 nm has refractive index and absorption coefficient of 4.22 and 0.4 cm^{-2} respectively [19]

wavelengths is the greatest. Figure 5.2 shows theoretical reflectivity of few different MoS_2 sample thicknesses: 10, 20, 30 and 40 nm on a Si wafer substrate. Calculations were performed by using [82]. These thicknesses were chosen in agreement with fabrication methods, as some of them have not been evaluated while preparing thicker samples. The highest theoretical reflectivity of about 81% for the EUV light (13 nm wavelength) should be possible to achieve with 20, 30 or 40 nm thickness of MoS_2 onto a Si wafer substrate. 10 nm MoS_2 should provide slightly lower reflectivity of about 73%.

According to the performed simulations and calculations, we can expect that the beam splitter will reduce high energy from the laser (to zero) and maximum about 81% of the EUV should be reflected. Unfortunately, theoretical calculations often do not match with the authentic, physical measurement - data of the optical properties (refractive index and extinction coefficient) for EUV and visible/IR light radiation were obtained by spectroscopic ellipsometry from [19]. Samples in the above work were prepared by vapor phase sulfurization. Data was taken and then values of refractive index were

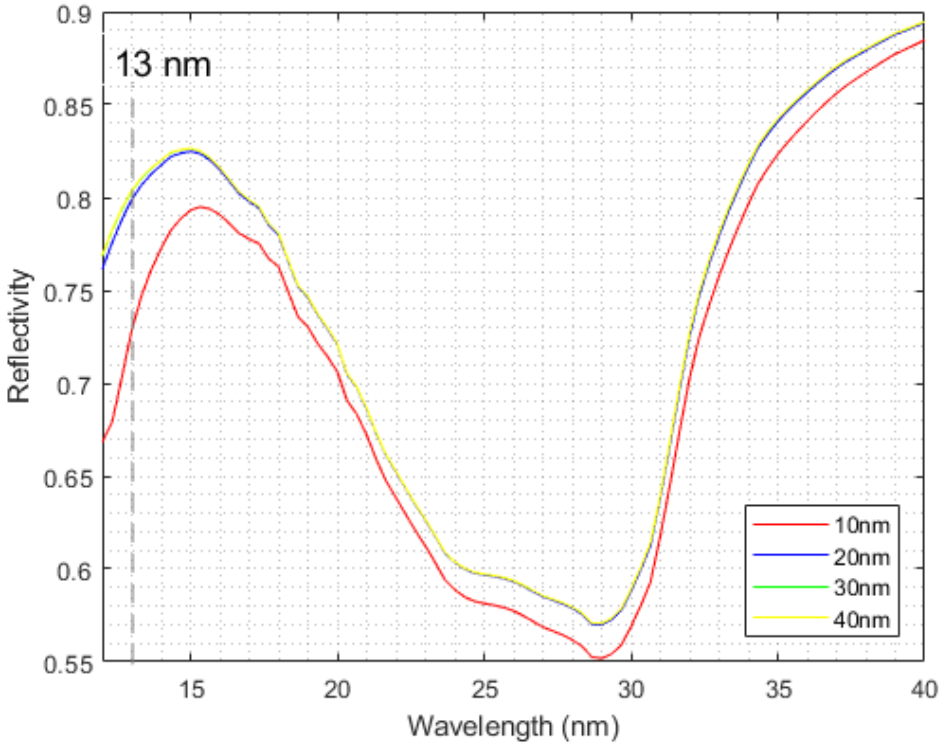

FIGURE 5.2: Reflectivity of MoS_2 for 10, 20, 30 and 40 nm of material on a substrate. Thickness of the MoS_2 which theoretically should provide the highest efficiency - the highest reflectivity for the EUV light should be about 81% for a sample 20, 30 or 40 nm. The reflectivity has been calculated for different thicknesses of the MoS_2 sample deposited onto a Si wafer substrate

interpolated for the MoS_2 and the required wavelength (4.22 for the wavelength of 790 nm). As our method of fabrication samples is different than in the mentioned work, the optical properties can vary. Another issue is the surface roughness of a sample, which ideally should be atomically smooth for the short wavelength light we use. That was an assumption while calculating EUV reflectivity versus sample thickness which due to technological limitations is not possible. Therefore, we can expect that part of the high energy laser will be still reflected and part of the EUV absorbed.

Sample surface

Whereas preparing MoS_2 samples, it came out that some of the fabrication methods are not straightforward to build on specific substrates. Also, while performing one of the reflectivity measurement for the MoS_2 sample, it appeared that the substrate is affecting reflectivity as the sample we tried to use is very thin (30-40 nm). Therefore, simulations have been performed in order to select the most appropriate and alternative substrate for the material. The substrate should be easy to use in fabrication MoS_2 process and provide high reflectivity too. Figure 5.3 shows reflectivity as a function of a material thickness for three different substrates: sapphire, Si wafer and glass. Using

information from [83], reflectivity coefficient and then reflectivity for the whole sample was calculated.

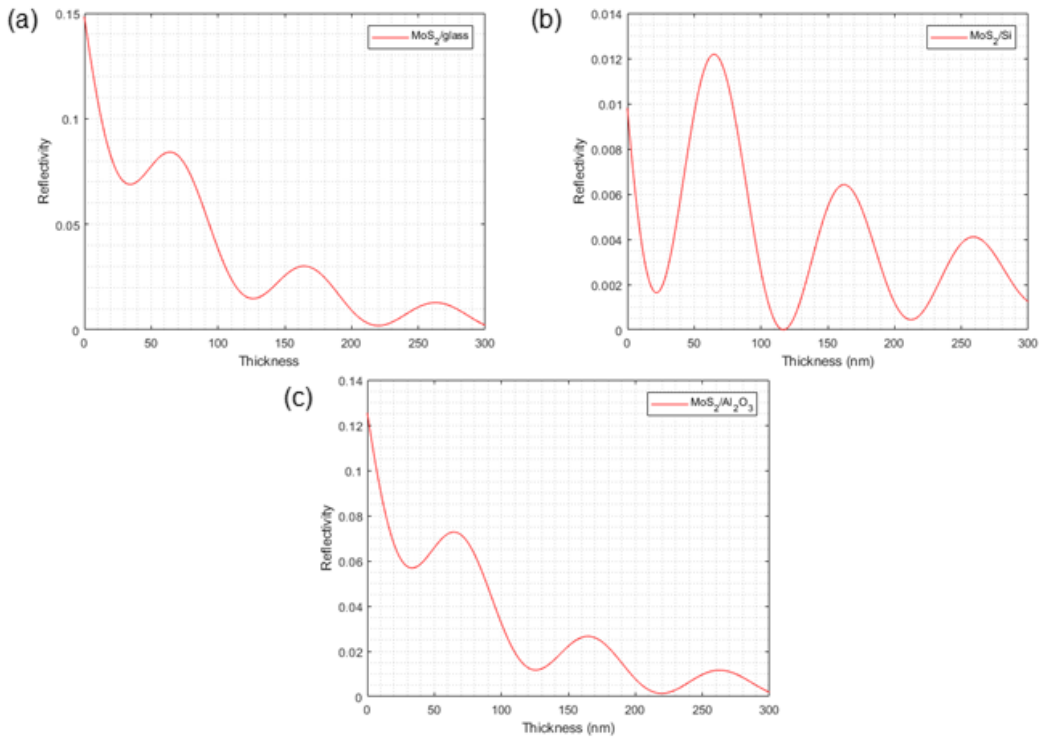

FIGURE 5.3: Theoretical reflectivity of a MoS_2 sample onto a three different substrates for the IR light (790 nm). The lowest, desired reflectivity for the high power laser combined with the most thinner MoS_2 (BS) sample appears for the sample deposited onto a Si wafer. Assuming that the refractive index for the sample was interpolated from some given data, values of the thickness can vary possibly between 20-30 nm. While increasing the thickness of the sample, other substrates could be used such as sapphire and glass. All calculations have been performed for the laser horizontally polarised and the MoS_2 sample placed at the Brewster's angle, which is about 77 deg

The lowest, desired reflectivity for IR light, close to the zero value can be achieved possibly with 20-30 nm of MoS_2 deposited onto a Si wafer. Another opportunity is thicker sample of MoS_2 onto sapphire or glass substrate. Deposition of thicker sample is a longer process, sometimes more sophisticated (depending on the production technique) and often increasing the roughness error.

5.1.3 Variation with Angle and Wavelength

Another important issue to consider is how much of the fundamental laser beam, MoS_2 BS is able to attenuate. The attenuation efficiency has been studied by calculating how much a beam splitter is able to attenuate considering wavelength and angular spread. The divergence of the beam was assumed to be 2.5 mrads and wavelength range between

700-900 nm. Figure 5.4 presents the distribution of the attenuation for MoS_2 according to the angle and wavelength changes (p-polarised light).

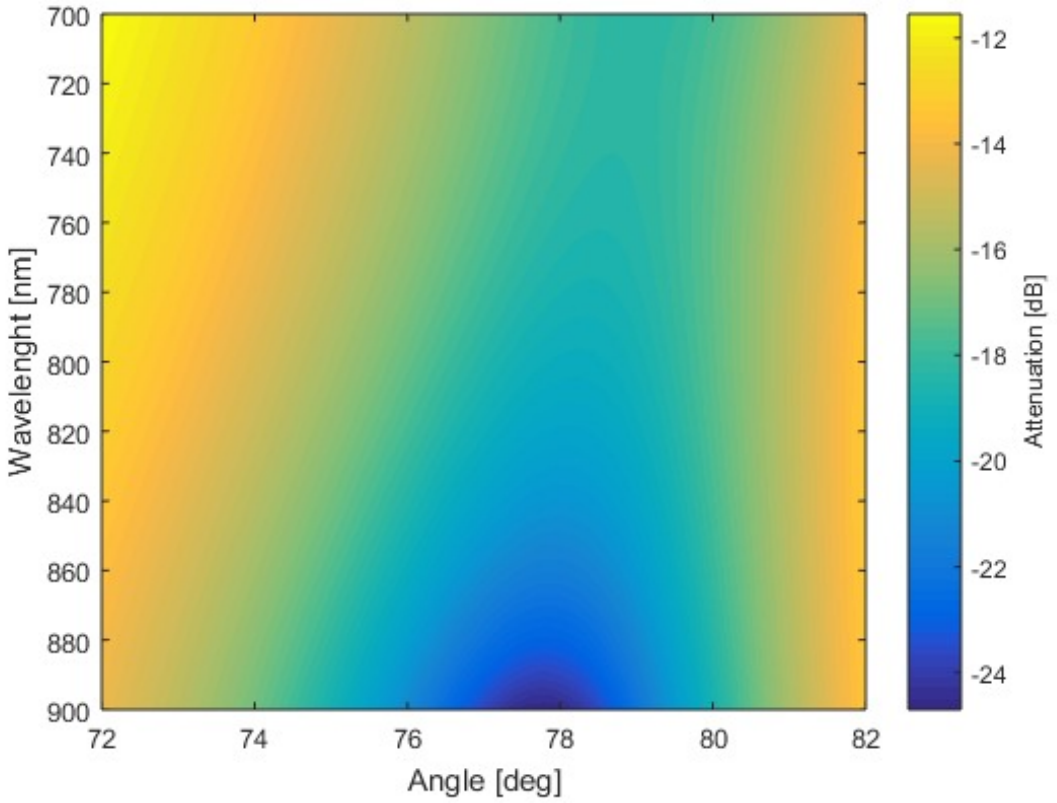

FIGURE 5.4: Attenuation power of the MoS_2 sample/Si wafer showing the spread of the attenuation power while the wavelength and the angle are changing. For the Brewster's angle (about 78 deg) the sample is able to attenuate the largest amount of the long wavelength and the value decreases while the wavelength is shorter. The attenuation power theoretically decreases while changing the angle of the sample is placed at. As we can spot, it is very important to place the sample precisely at the Brewster's angle

As it is presented in Figure 5.4 the MoS_2 beam splitter is able to attenuate about 24 dB of the power within an angle 78-79 deg. When the wavelength of light decreases, the attenuation efficiency for similar angle goes down by few dB. At the same time, in order to keep the highest efficiency of the beam splitter, the angle must be precisely specified as any changes will reduce the efficiency of attenuation. The wavelength of our interest is 790 nm wavelength, which gives about 20 dB of IR laser attenuation. Divergence/bandwidth of the laser and changes in the angle of incidence ware other factors which will also influence the final reflectivity.

5.2 Sample Preparation

Few MoS_2 beam splitters have been fabricated, two of them showed interesting and worth to discuss specifications. Those are 30 nm of MoS_2 fabricated onto a glass substrate and 30 nm of MoS_2 fabricated onto a Si wafer.

30 nm of MoS_2 were deposited onto a Si wafer by using magnetron sputtering process by Ioannis Zeimpekis (University of Southampton). The reflectivity of a sample has been measured then in the laboratory by using 790 nm of IR light.

FIGURE 5.5: Two samples of MoS_2 deposited onto Si wafer substrate by chemical vapor deposition process. As we can notice on the picture, the surface is rough and reflection is very low. Therefore, the fabricated sample could not be used as a BS in the HHG process. It is an example of a bad sample which will not reflect IR light considering visually rough surface of a sample. It is important to add that MoS_2 fabrication onto some different substrates can be challenging. Sizes of simples were chosen according to the experiment design for a synchrotron source. Both samples were prepared by Katrina Morgan (University of Southamtpon)

Figure 5.5 is an example of a bad sample.

Another sample consisted of 30 nm of MoS_2 on a quartz glass as a transparent substrate (Figure 5.6) was prepared by Huang Chung-Che (research group of Prof. Dan Hewak, University of Southampton) by using chemical vapor deposition process (CVD).

Figure 5.7 presents spectrum of a sample with the Raman modes E^1_{2g} and A_{1g}. Photon mode E^1_{2g} appeared on the spectrum from two S atoms vibrations with respect to the

Mo while mode A_{1g} represents vibrations of *S* atoms. It is a confirmation of MoS_2 sample. Figure 5.6 demonstrates thickness of the sample measured by SEM.

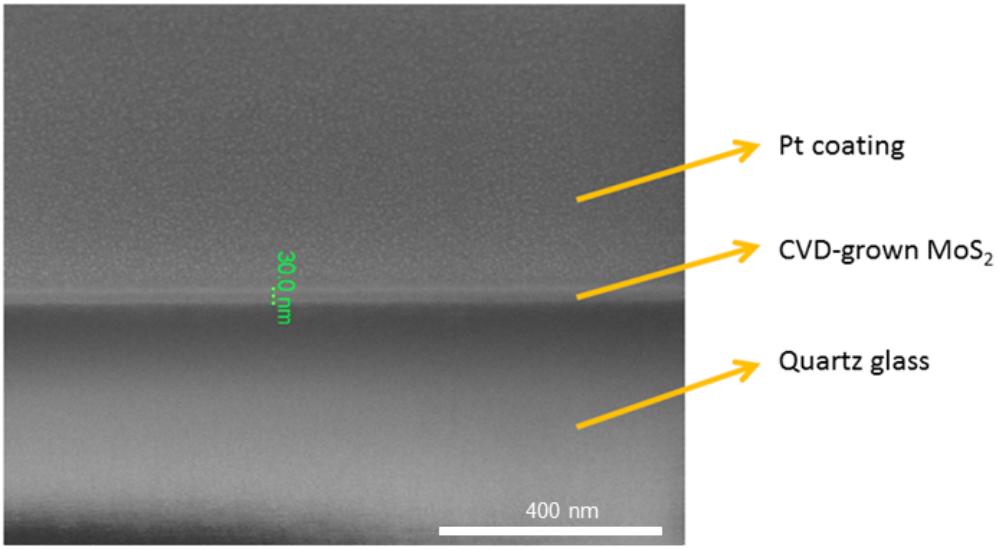

FIGURE 5.6: Cross-section SEM image by Bruce Ou (University of Southampton). Pt coating was deposited in order to measure the thickness of the MoS_2 layer and the final sample is free from Pl. It is a proof that fabrication method is successful and onto the substrate there is specific thickness of a sample

In order to estimate roughness of the MoS_2 surface an optical profilometer was used (Figure 5.8). The RMS and average roughness were found to be 3.12 nm and 1.26 nm respectively. According to the fact that the overall thickness of a layer is 30 nm, the variations in the roughness of about 1-3 nm should be acceptable in order to use the sample as a BS.

5.3 Reflectivity Measurement for MoS_2 Samples

Experimental setup which allowed for reflectivity measurement is presented in Figure 5.9.

The main IR laser beam is vertically polarised, therefore a Fresnel rhomb was used to change polarisation from the laser being *s*-polarised to *p*-polarised. A lens of 100 cm focal length has been used and the focus position region has been placed in a vacuum to prevent generation of plasma. An iris has been used to reduce the size of the IR beam to 2.5 mm diameter. In front of the iris, a rotatory stage has been placed holding the MoS_2 BS controlled by a computer to change the angle of a sample position. The beam reflected from the BS was directed onto the power meter, measuring the power of an IR light reflected from the MoS_2.

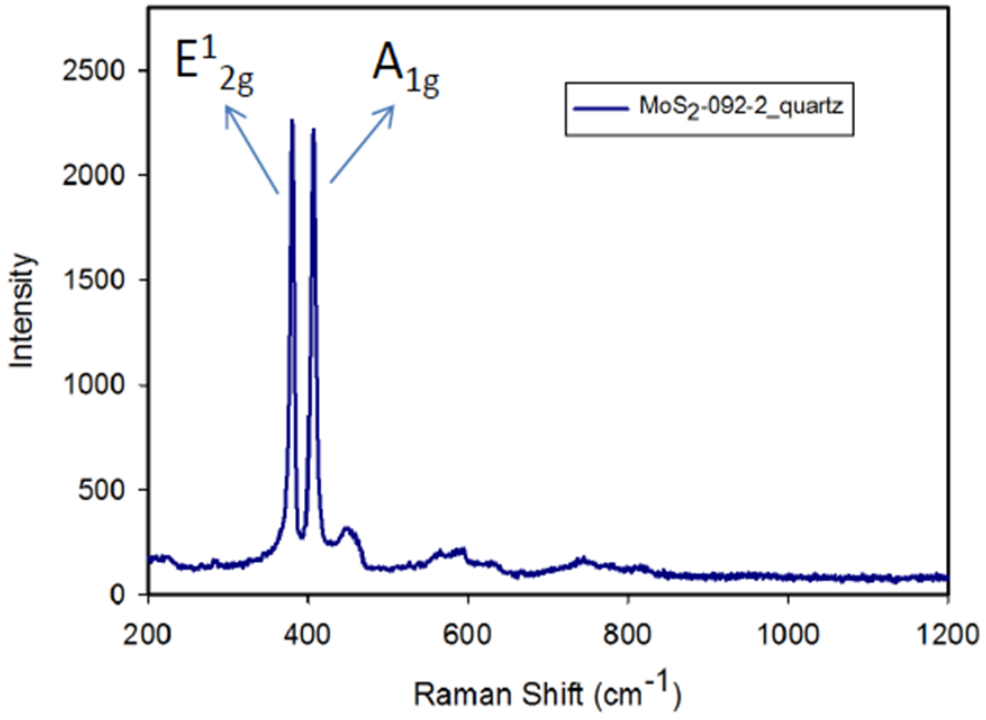

FIGURE 5.7: Raman spectrum of CVD-grown MoS_2 on quartz glass substrate by Bruce Ou (University of Southampton). By observing low-frequency modes such as rotational and vibrational the technique allows for atoms identification. The above spectrum presents Raman modes E^1_{2g} and A_{1g}

5.3.1 Data Analysis for MoS_2 Reflectivity Measurements

In Figure 5.12 measurement of the IR light reflectivity from MoS_2/glass and MoS_2/Si samples has been presented.

The minimum reflectivity for MoS_2/glass is about 20% which is high and means the sample cannot be used as a BS as the reflection of the IR light is not high enough. As simulations shows quite low reflectivity for the MoS_2 sample, possible reasons were analyzed. The thickness of the MoS_2 is about 30 nm (or less) onto a glass substrate which is a very thin layer of a substrate. Therefore, the IR light reflection may occur at 2 interfaces - MoS_2 and the glass substrate. Simulations have been performed both for the Si and glass substrate assuming the same conditions. Figure 5.11 shows results.

Brewster angle for a glass substrate is about 56 deg, 77-75 deg for Si and 77-78 for MoS_2. Therefore, some reflection could come from the glass as the layer of the MoS_2 is thin. As for Brewster's angle is about 77 deg, for the glass that angle we are getting some reflection of about 15-20 deg so quite similar as we achieved with MoS_2 layer. Therefore, Si wafer should be considered as a substrate for MoS_2.

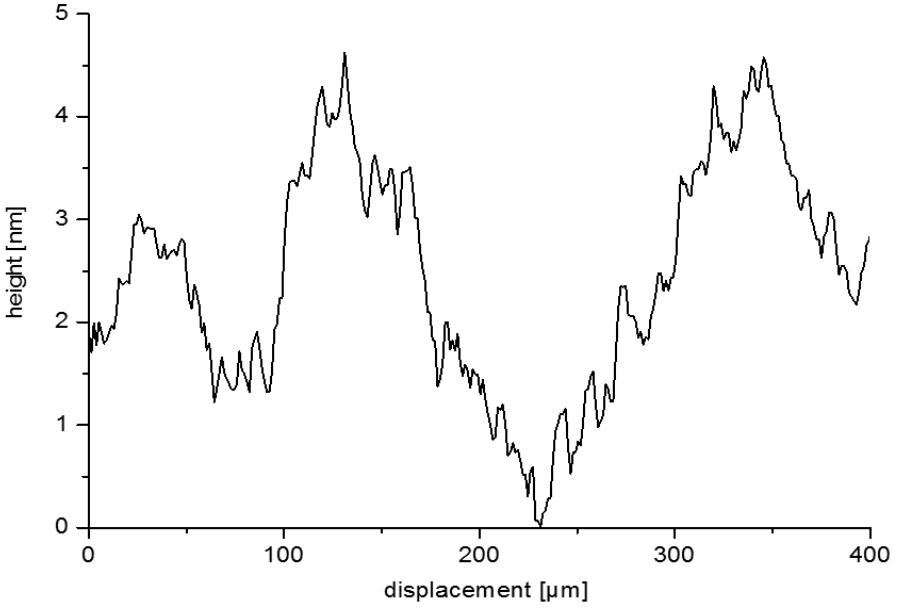

FIGURE 5.8: Roughness of the surface - MoS_2 beam splitter (optical profilometer). The RMS and average roughness were found to be 3.12 nm and 1.26 nm respectively which is acceptable for our purpose

MoS_2/Si shows low IR light reflectivity 5%. Figure presents the full reflectivity measurement for the MoS_2/Si sample. This is an initial measurement for Si and MoS_2/glass sample assuming that Brewster angle will be what was predicted, 78 deg. Brewster's angle has been moved from about 78 deg to 72 deg. The reason is that it is quite not the material we expected.

As we can also notice, reflectivity for Si sample is much lower than for MoS_2 and it is closer to the zero value. The reason why we could just not simply use Si as a beam splitter is that reflectivity for EUV is not high enough. Therefore, we need to compromise both EUV reflectivity with IR attenuation.

5.4 Summary of the MoS_2 BS

In this section design of a new MoS_2 beam splitter has been presented and high efficiency of the filter has been proven. Theoretical data showed low reflectivity for IR light while high reflectivity for the EUV (about 80%). Experimental data showed substantial attenuation of IR laser. Reflectivity of a beam splitter plays an important role during

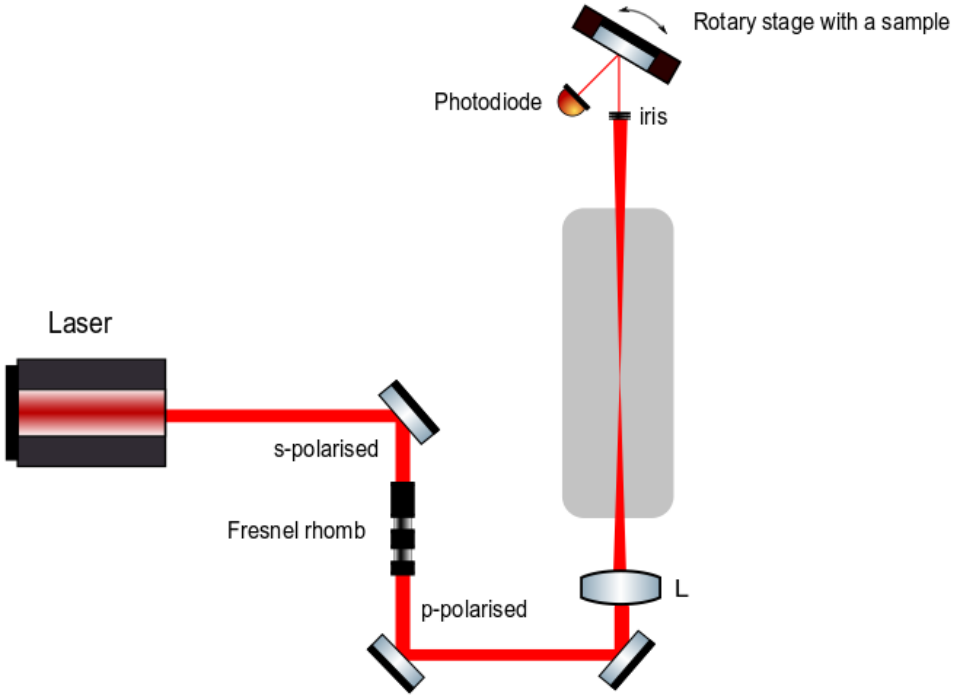

FIGURE 5.9: Configuration of the setup measuring reflectivity of the IR light from the Mo_2 sample. Originally, the laser is vertically polarised. After the beam is being reflected from a dielectric mirror, it goes through the Fresnel rhomb which changes polarisation from laser vertically polarised to horizontally polarised. Then the beam is being reflected from a second dielectric mirror, Ag mirror and goes to a lens with 100 cm focal length. The lens is being used to reconstruct the original configuration of the HHG setup. The focal length path was placed in a vacuum to avoid harmonic generation. An iris has been placed to decrease the size of the beam up to max 3 mm. At a distance 200 cm from the lens, rotatory stage was placed with a MoS_2 sample and reflection from it was measured by using photodiode

the HHG process as BS rejects the high power laser which drives with high harmonics. Brewster's angle is crucial for separation of two different wavelengths but can be challenging placing it into the optical system. Currently, in the Ultrafast X-rays Laboratory at the University of Southampton we use Al filters which highly attenuate the IR but they are also very fragile, hence other BSs are needed.

Separation efficiency during filtering the fundamental laser beam from the EUV signal can be improved by designing and then testing various materials. In the process of designing, there are many parameters which are crucial for a BS working in a vacuum environment. The main one is that the device has to withstand the energy associated with the driving high power laser. That requirement eliminates many materials Reflectivity properties for the EUV light and attenuation properties for the IR light will eliminate more. During the project, we met some difficulties during the fabrication process, therefore few attempts have been taken in order to fabricate MoS_2 beam splitter

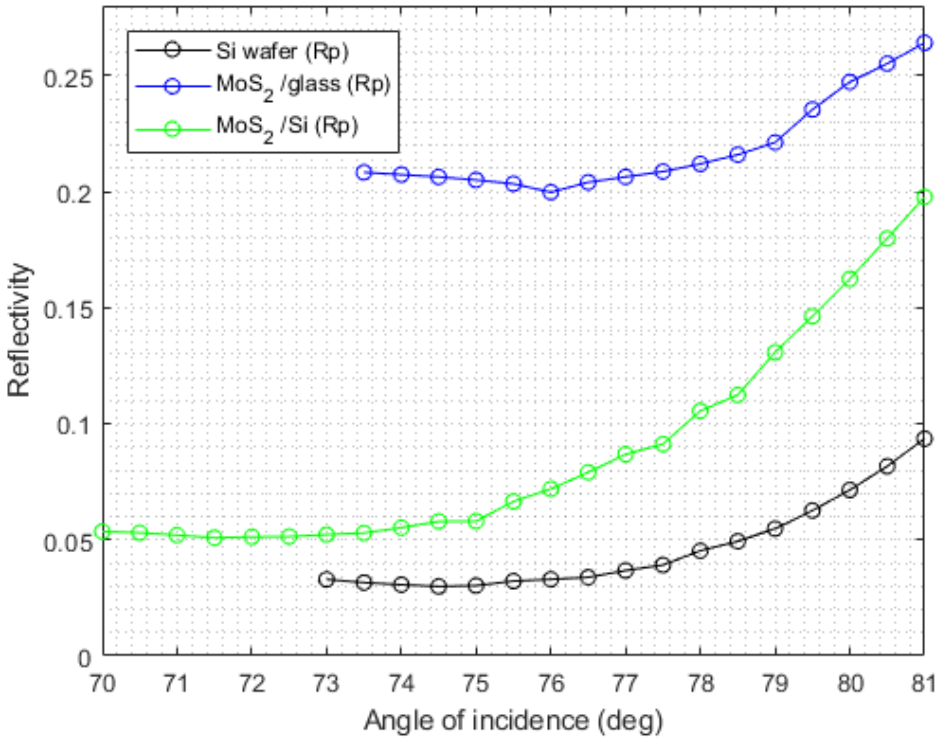

FIGURE 5.10: Reflectivity measurement for the *p*-polarised IR laser beam from the MoS_2/glass and MoS_2/Si samples. The angle of the sample respectively to the IR light beam was changing by 5 deg and an average power has been recorded for the MoS_2/Si. For MoS_2/glass sample the max power was recorded. BS onto a glass substrate does not provide low enough reflectivity to be used as BS in HHG process as the minimum reflectivity for IR is about 30%. MoS_2/Si sample provided low reflectivity of about 5%. We can notice that Brewster's angle for the MoS_2/Si is different that theoretical simulations due to reflectivity of the sample and it is about 73 deg

with desirable properties. Therefore, designing and fabricating can be often challenging, mainly due to the thickness of the fabricated device needed.

The next step is to test how much EUV light can be reflected by the MoS_2/Si sample and if it can withstand the long imaging process (lasting few hours). Improving separation efficiency is very important as it can improve the EUV flux, hence the imaging process.

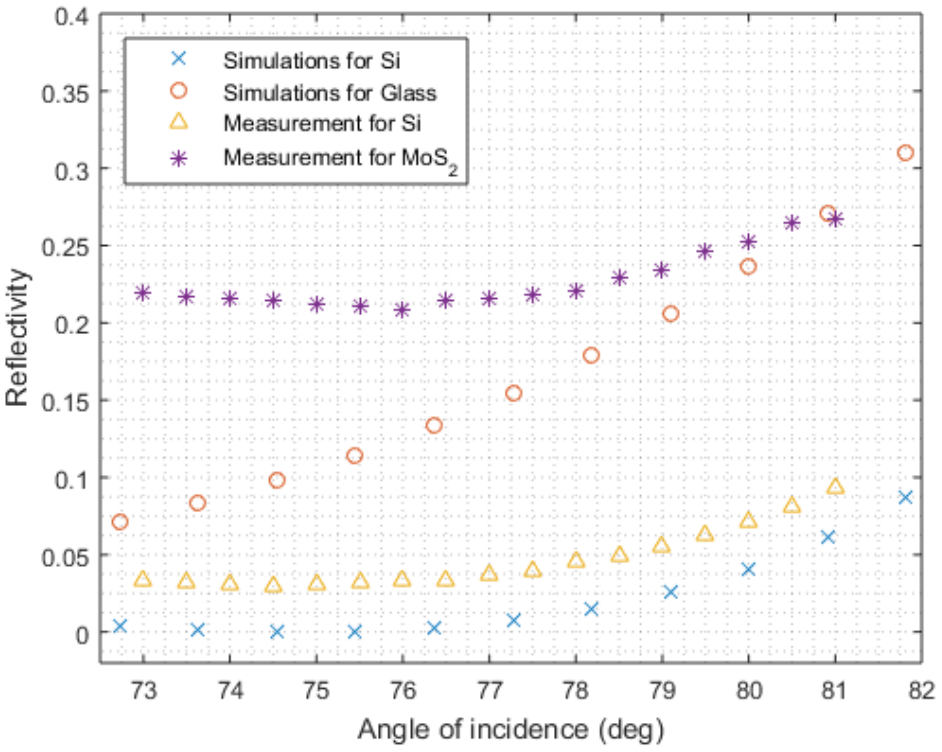

FIGURE 5.11: Simulations and measurements for Si, glass and MoS_2. As MoS_2/glass measurement showed much higher reflectivity for IR light than expected (calculated), some simulations have been performed to understand what the reason of that behavior. As it is presented, theoretical (calculated) reflectivity for glass is close to the performed measurement, we can expect that reflectivity of IR is coming from glass reflection as MoS_2 sample has only thickness of 40 nm. As theoretical IR reflectivity for Si is much lower, the decision to use MoS_2/Si fabrication has been taken

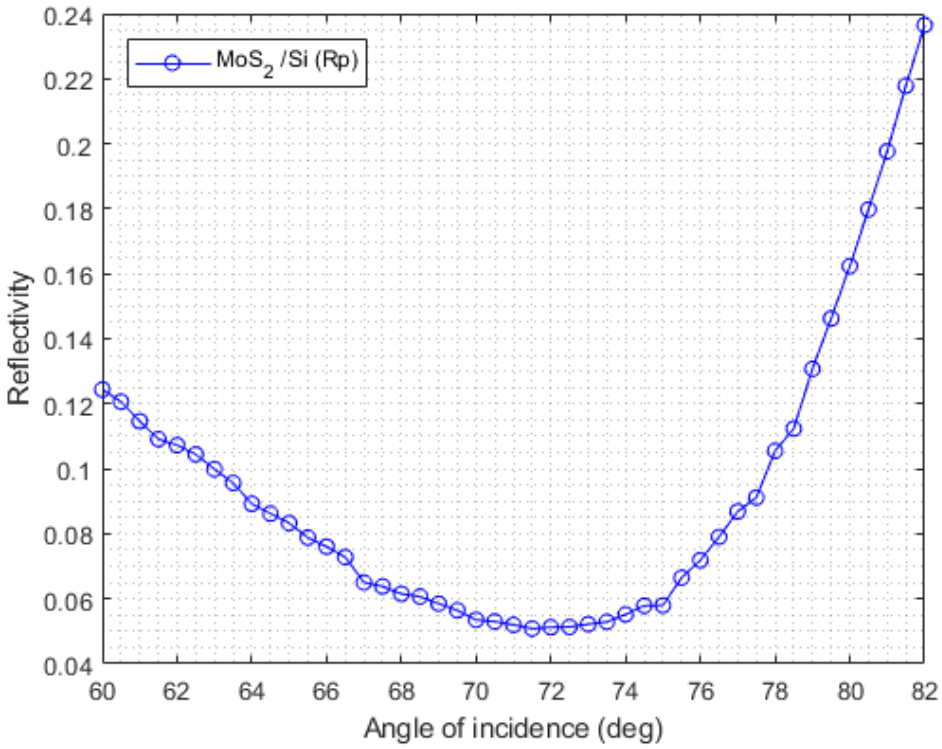

FIGURE 5.12: Reflectivity measurement for the *p*-polarised IR laser beam from the MoS_2. The maximum power of the IR light used in the experiment was 48.2 mW. Maximum and minimum value from the power meter was taken during the experiment and the average value was used to produce the results

Chapter 6

Conclusions and Future Work

6.1 Ptychographic Imaging of Biological Samples

Lensless imaging technique allows for resolving objects without lenses and hence with no aberrations to the image. Main requirements for successful ptychography scan is high coherence and high EUV flux. Higher flux allows for greater amount of light which can penetrate through the sample. Stable source improves quality of the data and increase efficiency of image reconstruction. During the project, experimental data were taken while imaging biological samples (neurons). All data was collected by EUV light passing through the aperture and being illuminated to the object, then phase retrieval algorithm has been used to recover information from the phase and create an image.

Few neurons samples have been imaged and then extensively studied. On the reconstructed images we can observe more details in comparison to the optical images. Specimens identified contain synapses, dendrites and axons, invisible by optical microscope. Ptychography proved high sensitivity of tiny objects as penetration depth is deeper in comparison to other techniques. Additionally, chemical composition of the structures can be studied providing estimation of the thin biological structures.

Ptychography imaging is a successful and powerful technique in determining structure of the imaging objects from its diffraction pattern. It has been proven that compared to other visualizing methods such as optical microscopy it improves biological images. Future plans include improvement of the source efficiency which allows for imaging older neurons. Mature samples are characterized by a very dense structure. Within high flux, EUV penetration can enhance and progress to resolving more specimens. The obtained information is essential notably for medical scientists as provides details about mechanisms within the neuron structure.

6.2 Adaptive Optics for EUV Wavefront Control

Modulation of the EUV wavefront was the main motivation for designing, fabricating and testing deformable mirrors (DM). Our research was mainly focused on surface quality or the produced DMs that affects both: the reflectance and the reflected wavefront distortion. But also hysteresis of the used piezo actuators was studied in order to understand reliability of the produced DM.

Stress experiments in voltage range ±0.5 V showed nonlinear hysteresis curve of the actuators with characteristics acceptable for further investigation. As expected, stronger hysteresis appeared towards the higher voltage values.

Deformations of the mirror's surface were examined with visible light by changing stress applied and using ZYGO interferometer to monitor shape of the mirror. As voltage increased, wavefront surface changes showed higher displacement. Maximum displacement observed was 2.38 μm with 0.5 V and -2.1 μm with -0.5 V. The device showed different curvatures of the mirror by applying specific stress values what we could observe by using interferometric data.

In the next experiments, multilayer reflectivity has been tested to specify stress influence. The most crucial observations showed that after 2 years (all samples with/without AO and with/without stress applied) a decrease in the reflectivity has taken place which could be associated with the degradation of a structure. After applying actuator and treating it with mechanical stress, a drop in the reflectance values is similar to the sample without an actuator applied. Therefore, DMs showed good performance in maintaining reflectance values at 30.4 nm of EUV wavelength. We found that multilayer structures can attain long lifetime (at least 2 years) and they are able to provide stable construction after rapid (100 Hz) mechanical stress.

Deformable mirror has been tested for applications in the EUV system, by HHG process. By applying different voltage values, we could observe changes in the EUV spot. Preliminary tests showed good control of the wavefront in the EUV spectral range, although the mirror's quality needs improvement. The device can massively improve resolution of imaging systems operating in the EUV wavelength. Therefore, the research area of adapting adaptive optics for multilayer mirrors and controlling the wavefront distortions appears promising.

Next step is to improve quality of the DM and to perform simple ptychographic scan. Then, the plan is to use more than one actuator attached to the DM. Higher amount of piezoelectric actuators allows for better modulation and control of the wavefront.

6.3 MoS_2 Beam Splitter as a Separator for HHG Process

Beam splitters are efficient optical devices in separating cooperating, different wavelengths of light. They can be used in the HHG process, where the fundamental laser comes along with the EUV signal and has to be highly attenuated to protect optics and samples. During the project, effort has been concentrated on theoretical simulations in order to design a new separator for our HHG system in the Ultrafast X-rays Laboratory at the University of Southampton. Currently we use Al filter which highly attenuates the IR light but we are interested in other materials too. New BS could enhance the EUV flux which is desirable mainly for imaging experiments (currently 10 nJ/pulse).

After performing IR light reflectivity simulations for several different samples, MoS_2 showed high theoretical reflectivity in the EUV region of about 80%, efficient attenuation of a fundamental laser beams and acceptable surface roughness.

Three BSs have been built as every next one supposed to decrease IR light reflectivity. The first sample, MoS_2 onto a glass substrate fabricated by CVD after performing measurement, it showed much higher IR reflectivity than expected. After deeper analysis it became obvious that reflectivity is coming from the substrate used in fabrication process. Our first assumption about any transmittive substrate was not strictly correct as the substrate can also affect IR reflectivity, probably while using thin samples. Therefore, we achieved 20% of light reflected from the MoS_2/glass sample which in comparison to the glass reflection seems to be similar. Then, we decided to study surface selection for the BS which would decrease IR reflectivity. We looked at different substrates such as Al_2O_3 (sapphire), Si and glass. The higher thickness of a sample increases roughness of a surface, which is very important for our purpose. At the same time, we found out, that some of the fabrication methods are challenging to perform while building the structure of MoS_2 layers and keeping the same properties of the following structures. Some production processes will not allow us to achieve smooth surface of a sample, and other methods are difficult for thick sample fabrication. Therefore, while choosing the superior substrate and to avoid some more complications it is valuable to consider thinner sample than the thicker one. Following that, silicon substrate in theory provided the lowest, close to the zero value IR reflectivity with 20-30 nm sample.

Additionally, the stability of the MoS_2/Si sample has been tested while shining the IR light of a 1W power for 15 min. Apart from being warm, visually there was no noticeable damage onto the surface. Demonstrated measurement indicating IR light reflection of a MoS_2/Si sample showed low reflectivity, therefore the sample can be possibly used during the HHG process. Experiments are planned to implement reflectivity measurement in the EUV.

The next step is to experimentally test how much EUV light can be reflected by the MoS_2/Si sample. Besides, previously taken data which measured attenuation of the IR light was corresponding to the 1W power. During the ptychographic scan the min. power used to produce EUV light is about 1.5W (15 min time of exposure). Further, the new BS has to be tested in the environment for the soft x-rays imaging where scanning an object is lasting few hours.

Appendix A

Biological Sample Information

Poly-D-Lysine (PDL) Poly-D-Lysine is a synthetic molecule, a thin coating, which is usually used to enhance attachment of cells to glass or plastic surfaces.

Phosphate-buffered saline (PBS) Phosphate-buffered saline is used in biological research. It is a buffer solution which generally contains disodium hydrogen phosphate, potassium chloride, sodium chloride, potassium chloride and potassium dihydrogen phosphate. It helps to keep constant pH.

Trypsin enzyme Trypsin enzyme is used in various biotechnological processes. In vitro, it helps to cleave proteins bonding as some cells have tendency to adhere to the bottom of a dish while in vitro cultivation. Then, cells can be transferred to fresh dishes.

Fetal bovine serum (FBS) Fetal bovine serum is a fraction of the blood. It is widely used in vitro cell cultures (eukaryotic cells).

Neuronal Growth Media (NGM) Neuronal Growth Media are neuronal growth supplement.

Neurobasal Glutamax Neurobasal Glutamax is a serum-free supplement.

B-27 B-27 is a serum-free supplement.

Paraformaldehyde solution (PFS) Paraformaldehyde solution is used in cell biology for fixation.

Appendix B

BEAR Beamline at Elettra Synchrotron

All measurements at the BEAR beam line at Elettra Synchrotron (Trieste, Italy) in April 2015 were performed with properties as below:

- Monochromator: GNIM in full beam configuration
- Scan in the 25-35 nm range (35-50 eV)
- Scan step $\Delta E = 0.2eV$
- Exit slit vertical aperture at 150 µm
- *s*- configuration

Appendix C

Publications

Journal Publications

H.S. Kim, P. Baksh, M.Odstrcil, M. Miszczak, J.G. Frey, L. Juschkin and W.S. Brocklesby, Lloyds mirror interference lithography with EUV radiation from a high-harmonic source. *Applied Physics Express (2016), 9(7), p.076701*

A.J. Corso, S. Bonora, P. Zuppella, P. Baksh, M. Miszczak, W.S. Brocklesby, Z. Wang, P. Nicolosi, M.G. Pelizzo, Developing an EUV multilayer adaptive mirror: the first results. *Proc. SPIE 9963, Advances in X-Ray/EUV Optics and Components XI (2016)*

Conference Contributions

M. Miszczak, W.S. Brocklesby, Optics for short pulse X-Ray sources, *ELI Beamlines Summer School 2014, August 24-19 2014, Prague, Czech Republic (poster presentation)*

M. Miszczak, W.S. Brocklesby, Optics for short pulse X-Ray sources, *COST Action MP1203, Training School for advanced X-ray spatial and temporal metrology, General Assembly, September 29 - October 04 2014 , Dubrovnik, Croatia (poster presentation)*

M. Miszczak, J. Frey, W.S. Brocklesby, Optics for short pulse X-Ray sources, *EXTATIC Workshop 2014, October 20-24 2014, Warsaw, Poland (oral presentation)*

M. Miszczak. S. Bonora, A.J. Corso, D. Bacco, A. Donazzan, P. Zuppella, Z. Wang. P. Nicolosi, W.S. Brocklesby, M.G. Pellizo, Multilayer adaptive optics development for the

EUV wavefront control, *10th International Workshop on Adaptive Optics for Industry and Medicine, June 15-19 2015, Padova, Italy (poster presentation)*

M. Miszczak. S. Bonora, A.J. Corso, P. Baksh, Z. Wang. P. Nicolosi, M.G. Pelizzo, W.S. Brocklesby, M.G. Pellizo, Deformable mirror as a wavefront control device in the EUV radiation, *EXTATIC meeting 2016, January 11-15 2016, Warsaw, Poland (oral presentation)*

M. Miszczak, S. Bonora, P. Baksh, A.J. Corso, Z. Wang, P. Nicolosi, M.G. Pelizzo, W.S. Brocklesby, Deformable mirror as a wavefront control device in the EUV radiation , *COST Action: MP1203, Meeting WG1: X-ray spatial metrology of optics; Damage on X-ray optics on Advanced X-ray mirror metrology, April 28-29 2016, Tallinn, Estonia (oral presentation)*

M. Miszczak. S. Bonora, A.J. Corso, D. Bacco, A. Donazzan, P. Zuppella, Z. Wang. P. Nicolosi, W.S. Brocklesby, M.G. Pellizo, Multilayer adaptive optics development for the EUV wavefront control, *COST Action [MP1203] event: MC meeting co-located with X-ray optic metrology, September 19-21 2016, Athens, Greece (poster presentation)*

Bibliography

[1] David Attwood. *Soft x-rays and extreme ultraviolet radiation: principles and applications*. Cambridge University Press, 1999.

[2] M-C Chen, P Arpin, T Popmintchev, M Gerrity, B Zhang, M Seaberg, D Popmintchev, MM Murnane, and HC Kapteyn. Bright, coherent, ultrafast soft x-ray harmonics spanning the water window from a tabletop light source. *Physical Review Letters*, 105(17):173901, 2010.

[3] Philippe Wernet, Jérôme Gaudin, Kai Godehusen, Olaf Schwarzkopf, and Wolfgang Eberhardt. Femtosecond time-resolved photoelectron spectroscopy with a vacuum-ultraviolet photon source based on laser high-order harmonic generation. *Review of Scientific Instruments*, 82(6):063114, 2011.

[4] URL `http://www.aura-astronomy.org/news,on14.04.2016`.

[5] MDASHF i@M Invariance. Optical aberrations, 2017. URL `https://mdashf.org/2017/01/25/aberrations-a-lecture-in-optics`. Accessed: 2017-09-30.

[6] Solo Hermelin. Human eye optics. URL `https://www.slideshare.net/solohermelin/human-eye-optics`. Accessed: 2017-10-24.

[7] Edmund Optics. How aberrations affect machine vision lenses, . URL `https://www.edmundoptics.com/resources/application-notes/imaging/how-aberrations-affect-machine-vision-lenses`. Accessed: 2017-10-24.

[8] Edmund Optics. Comparison of optical aberrations, . URL `https://www.edmundoptics.eu/resources/application-notes/optics/comparison-of-optical-aberrations`. Accessed: 2017-10-24.

[9] Sebastián Mirasol-Menacho, Ana Planells-Pérez, Arturo Barba-Sevillano, Jaume Segura-Garcia, Máximo Cobos-Serrano, and Alicia Giménez-Pérez. Development of a hmd for virtual acoustics. application in a world heritage (unesco) building from the valencian civil gothic. In *International Conference on Augmented Reality, Virtual Reality and Computer Graphics*, pages 241–250. Springer, 2016.

[10] Purveyor Of Light. How-to, lightroom, photography. URL `http://www.purveyoroflight.com/blog/correcting-lens-distortion-in-adobe-lightroom`. Accessed: 2017-10-24.

[11] Teoria das aberrações óticas. URL `http://astro.if.ufrgs.br/telesc/aberracao.htm`. Accessed: 2017-08-23.

[12] Bettina Mikulec, John V Vallerga, Jason B McPhate, Anton S Tremsin, Oswald HW Siegmund, and Allan G Clark. A high resolution, high frame rate detector based on a microchannel plate readout with the medipix2 counting cmos pixel chip. *IEEE transactions on nuclear science*, 52(4):1021–1026, 2005.

[13] Larry N Thibos and Xin Hong. Clinical applications of the shack-hartmann aberrometer. *Optometry & Vision Science*, 76(12):817–825, 1999.

[14] Shack–hartmann wavefront sensor. URL `http://www.wikiwand.com/en`. Accessed: 2017-10-24.

[15] K Giewekemeyer, M Beckers, T Gorniak, M Grunze, T Salditt, and A Rosenhahn. Ptychographic coherent x-ray diffractive imaging in the water window. *Optics express*, 19(2):1037–1050, 2011.

[16] Andrew M Maiden and John M Rodenburg. An improved ptychographical phase retrieval algorithm for diffractive imaging. *Ultramicroscopy*, 109(10):1256–1262, 2009.

[17] Martin Wilson. Microscope resolution: Concepts, factors and calculation. airy discs, abbe's diffraction limit and the rayleigh criterion. URL `http://www.leica-microsystems.com/science-lab/microscope-resolution-concepts-factors-and-calculation`. Accessed: 2017-10-12.

[18] Samuel M. Goldwasser. Laser instruments and applications. URL `http://www.repairfaq.org/sam/laserlia.htm`. Accessed: 2017-11-11.

[19] Chanyoung Yim, Maria O'Brien, Niall McEvoy, Sinéad Winters, Inam Mirza, James G Lunney, and Georg S Duesberg. Investigation of the optical properties of mos2 thin films using spectroscopic ellipsometry. *Applied Physics Letters*, 104(10): 103114, 2014.

[20] Robert Hooke. *Micrographia*. Science Heritage Limited, 1972.

[21] Ernst HK Stelzer. Light microscopy: Beyond the diffraction limit? *Nature*, 417 (6891):806–807, 2002.

[22] Charles W Gwyn, R Stulen, D Sweeney, and D Attwood. Extreme ultraviolet lithography. *Journal of Vacuum Science & Technology B: Microelectronics and Nanometer Structures Processing, Measurement, and Phenomena*, 16(6):3142–3149, 1998.

[23] Vivek Bakshi. *EUV lithography*, volume 178. Spie Press, 2009.

[24] James R Lemen, David J Akin, Paul F Boerner, Catherine Chou, Jerry F Drake, Dexter W Duncan, Christopher G Edwards, Frank M Friedlaender, Gary F Heyman, Neal E Hurlburt, et al. The atmospheric imaging assembly (aia) on the solar dynamics observatory (sdo). In *The Solar Dynamics Observatory*, pages 17–40. Springer, 2011.

[25] Christian Wagner and Noreen Harned. Euv lithography: Lithography gets extreme. *Nature Photonics*, 4(1):24–26, 2010.

[26] Igor'Mikhailovich Ternov. Synchrotron radiation. *Physics-Uspekhi*, 38(4):409, 1995.

[27] Vladimir A Bordovitsyn. *Synchrotron radiation theory and its development: in memory of IM Ternov*, volume 5. World Scientific Publishing Co Inc, 1999.

[28] Vivek Bakshi. Euv source technology: Challenges and status, 2005.

[29] Jeroen Jonkers. High power extreme ultra-violet (euv) light sources for future lithography. *Plasma Sources Science and Technology*, 15(2):S8, 2006.

[30] John MJ Madey. Stimulated emission of bremsstrahlung in a periodic magnetic field. *Journal of Applied Physics*, 42(5):1906–1913, 1971.

[31] Claudio Pellegrini. The history of x-ray free-electron lasers. *The European Physical Journal H*, 37(5):659–708, 2012.

[32] Zhirong Huang and Kwang-Je Kim. Review of x-ray free-electron laser theory. *Physical Review Special Topics-Accelerators and Beams*, 10(3):034801, 2007.

[33] Zhong-lin Wang. *Elastic and inelastic scattering in electron diffraction and imaging*. Springer Science & Business Media, 2013.

[34] Andrew Lee Aquila. Development of extreme ultraviolet and soft x-ray multilayer optics for scientific studies with femtosecond/attosecond sources. *Lawrence Berkeley National Laboratory*, 2009.

[35] Michael Hofstetter. *Multilayer mirrors for attosecond pulse shaping between 30 and 200 eV*. PhD thesis, Ludwig-Maximilians-Universität, 2011.

[36] Ileana Nedelcu. *Interface structure and interdiffusion in Mo/Si multilayers*. University of Twente, 2007.

[37] Nicolas Benoit, Sergiy Yulin, Torsten Feigl, and Norbert Kaiser. Radiation stability of EUV Mo/Si multilayer mirrors. *Physica B: Condensed Matter*, 357(1):222–226, 2005.

[38] Yutaka Nagata, Yasuo Nabekawa, and Katsumi Midorikawa. Development of high-throughput, high-damage-threshold beam separator for13 nm high-order harmonics. *Optics Letters*, 31(9):1316–1318, 2006.

[39] Eiji J Takahashi, Hirokazu Hasegawa, Yasuo Nabekawa, and Katsumi Midorikawa. High-throughput, high-damage-threshold broadband beam splitter for high-order harmonics in the extreme-ultraviolet region. *Optics Letters*, 29(5):507–509, 2004.

[40] Y Sanjo, M Murata, Y Tanaka, H Kumagai, and M Chigane. TiO2/sapphire beam splitter for high-order harmonics. *Journal of Laser Micro/Nanoengineering*, 7(3): 375–379, 2012.

[41] Ioachim Pupeza, Ernst E Fill, and Ferenc Krausz. Low-loss VIS/IR-XUV beam splitter for high-power applications. *Optics Express*, 19(13):12108–12118, 2011.

[42] Ferenc Krausz and Misha Ivanov. Attosecond physics. *Reviews of Modern Physics*, 81(1):163, 2009.

[43] Ahmed H Zewail. Femtochemistry: Concepts and applications. *Femtosecond Chemistry*, pages 14–128, 1995.

[44] Friedrich Dausinger and Friedemann Lichtner. *Femtosecond technology for technical and medical applications*, volume 96. Springer Science & Business Media, 2004.

[45] Walter T Welford. *Aberrations of the symmetrical optical system*. Academic Press, 1974.

[46] Gerard Rousset. Wave-front sensors. *Adaptive optics in astronomy*, 1:91, 1999.

[47] Joseph M Geary. *Introduction to wavefront sensors*, volume 18. Spie Press, 1995.

[48] Zernike von F. Beugungstheorie des schneidenver-fahrens und seiner verbesserten form, der phasenkontrastmethode. *Physica*, 1(7-12):689–704, 1934.

[49] Ben C Platt and Roland Shack. History and principles of shack-hartmann wavefront sensing. *Journal of Refractive Surgery*, 17(5):S573–S577, 2001.

[50] Esther Moreno-Barriuso and Rafael Navarro. Laser ray tracing versus hartmann–shack sensor for measuring optical aberrations in the human eye. *JOSA A*, 17(6): 974–985, 2000.

[51] Daniel Malacara-Hernández and Zacarías Malacara-Hernández. *Handbook of optical design*. CRC Press, 2013.

[52] Daniele Brida, Stefano Bonora, Cristian Manzoni, Marco Marangoni, Paolo Villoresi, Sandro De Silvestri, and Giulio Cerullo. Generation of 8.5-fs pulses at 1.3 μm for ultrabroadband pump-probe spectroscopy. *Optics Express*, 17(15):12510–12515, 2009.

[53] Ltd APC International. *Piezoelectric ceramics: principles and applications*. APC International, 2002.

[54] George B Parrent Jr. Basic theory of partial coherence. In *Proceedings of the April 26-28, 1966, Spring joint computer conference*, pages 17–24. ACM, 1966.

[55] Jianwei Miao, David Sayre, and HN Chapman. Phase retrieval from the magnitude of the fourier transforms of nonperiodic objects. *JOSA A*, 15(6):1662–1669, 1998.

[56] David Sayre. Some implications of a theorem due to shannon. *Acta Crystallographica*, 5(6):843–843, 1952.

[57] Harry Nyquist. Certain topics in telegraph transmission theory. *Transactions of the American Institute of Electrical Engineers*, 47(2):617–644, 1928.

[58] RHT Bates and WR Fright. Composite two-dimensional phase-restoration procedure. *JOSA*, 73(3):358–365, 1983.

[59] Jianwei Miao and D Sayre. On possible extensions of x-ray crystallography through diffraction-pattern oversampling. *Acta Crystallographica Section A: Foundations of Crystallography*, 56(6):596–605, 2000.

[60] Walter Hoppe. Beugung im inhomogenen primärstrahlwellenfeld. i. prinzip einer phasenmessung von elektronenbeungungsinterferenzen. *Acta Crystallographica Section A: Crystal Physics, Diffraction, Theoretical and General Crystallography*, 25 (4):495–501, 1969.

[61] HML Faulkner and JM Rodenburg. Movable aperture lensless transmission microscopy: a novel phase retrieval algorithm. *Physical review letters*, 93(2):023903, 2004.

[62] Pierre Thibault, Martin Dierolf, Andreas Menzel, Oliver Bunk, Christian David, and Franz Pfeiffer. High-resolution scanning x-ray diffraction microscopy. *Science*, 321(5887):379–382, 2008.

[63] Veit Elser, I Rankenburg, and P Thibault. Searching with iterated maps. *Proceedings of the National Academy of Sciences*, 104(2):418–423, 2007.

[64] Albert Rose. The visual process. In *Vision*, pages 1–27. Springer, 1973.

[65] George Biddell Airy. On the diffraction of an object-glass with circular aperture. *Transactions of the Cambridge Philosophical Society*, 5:283, 1835.

[66] C Nave. Radiation damage in protein crystallography. *Radiation Physics and Chemistry*, 45(3):483–490, 1995.

[67] Jan Kmetko, Naji S Husseini, Matthew Naides, Yevgeniy Kalinin, and Robert E Thorne. Quantifying x-ray radiation damage in protein crystals at cryogenic temperatures. *Acta Crystallographica Section D: Biological Crystallography*, 62(9):1030–1038, 2006.

[68] Tobias Beetz. *Soft X-ray diffraction imaging with and without lenses and radiation damage studies*. PhD thesis, Stony Brook University, 2004.

[69] Malcolm R Howells, Tobias Beetz, Henry N Chapman, C Cui, JM Holton, CJ Jacobsen, J Kirz, Enju Lima, Stefano Marchesini, Huijie Miao, et al. An assessment of the resolution limitation due to radiation-damage in x-ray diffraction microscopy. *Journal of electron spectroscopy and related phenomena*, 170(1):4–12, 2009.

[70] Bruce F McEwen, Kenneth H Downing, and Robert M Glaeser. The relevance of dose-fractionation in tomography of radiation-sensitive specimens. *Ultramicroscopy*, 60(3):357–373, 1995.

[71] Lars Bertram and Rudolph E Tanzi. The genetic epidemiology of neurodegenerative disease. *Journal of Clinical Investigation*, 115(6):1449, 2005.

[72] Mahendra S Rao and Marcus Jacobson. *Developmental neurobiology*. Springer Science & Business Media, 2006.

[73] Harvey Lodish, Arnold Berk, S Lawrence Zipursky, Paul Matsudaira, David Baltimore, and James Darnell. Molecular cell biology 4th edition. *National Center for Biotechnology InformationÕs Bookshelf*, 2000.

[74] Paul Gillam. Nerve cells and synapses: A* understanding for igcse biology. URL `https://pmgbiology.com/2015/02/18/nerve-cells-and-synapses-a-understanding-for-igcse-biology`. Accessed: 2017-10-17.

[75] Gyorgy Buzsaki. *Rhythms of the Brain*. Oxford University Press, 2006.

[76] James R Janesick. *Scientific charge-coupled devices*, volume 83. SPIE press, 2001.

[77] Jon Sutton. What is hdr (high dynamic range) and why is it important for gaming? URL `http://www.game-debate.com/news/20603/what-is-hdr-high-dynamic-range-and-why-is-it-important-for-gaming`. Accessed: 2017-10-12.

[78] Peter Baksh. *Ptychographic imaging of real biological samples using a high harmonic and synchrotron source University of Southampton.* PhD dissertation, University of Southampton, 2012.

[79] Fengnian Xia, Han Wang, and Yichen Jia. Rediscovering black phosphorus as an anisotropic layered material for optoelectronics and electronics. *Nature communications*, 5:4458, 2014.

[80] Qing Hua Wang, Kourosh Kalantar-Zadeh, Andras Kis, Jonathan N Coleman, and Michael S Strano. Electronics and optoelectronics of two-dimensional transition metal dichalcogenides. *Nature nanotechnology*, 7(11):699–712, 2012.

[81] Chung-Che Huang, Feras Al-Saab, Yudong Wang, Jun-Yu Ou, John C Walker, Shuncai Wang, Behrad Gholipour, Robert E Simpson, and Daniel W Hewak. Scalable high-mobility mos 2 thin films fabricated by an atmospheric pressure chemical vapor deposition process at ambient temperature. *Nanoscale*, 6(21):12792–12797, 2014.

[82] Farhad Salmassi and Eric Gullikson. measured july 2005 at advance light source. URL `http://www-cxro.lbl.gov`. Accessed: 2014-05-14.

[83] Harland Tompkins and Eugene A Irene. *Handbook of ellipsometry.* William Andrew, 2005.